UNIVERSITY OF OKLAHOMA

GRADUATE COLLEGE

# THEORETICAL ANALYSIS OF AND BIAS CORRECTION FOR PLANAR AND CYLINDRICAL POLARIMETRIC PHASED ARRAY WEATHER RADAR

A DISSERTATION

SUBMITTED TO THE GRADUATE FACULTY

in partial fulfillment of the requirements for the

Degree of

DOCTOR OF PHILOSOPHY

By

LEI LEI
Norman, Oklahoma
2014

THEORETICAL ANALYSIS OF AND BIAS CORRECTION FOR PLANAR AND CYLINDRICAL POLARIMETRIC PHASED ARRAY WEATHER RADAR

A DISSERTATION APPROVED FOR THE
SCHOOL OF ELECTRICAL AND COMPUTER ENGINEERING

BY

_____
Dr. Guifu Zhang, Chair

_____
Dr. Richard Doviak, Co-Chair

_____
Dr. Robert Palmer

_____
Dr. Yan (Rockee) Zhang

_____
Dr. Yang Hong

## Acknowledgements

First, I would like to thank my advisors Drs. Richard J. Doviak and Guifu Zhang, who have been insightful and inspirational guides during my Ph.D. study. They are the smartest people I have ever known. Dr. Zhang always has innovative ideas and frequently leads to key insights. He has an exceptionally strong ability to select and to approach compelling research projects. Dr. Doviak is always patient with difficulties and encouraging of new ideas. His extraordinary high scientific standards and work ethic set an example for me. I also appreciate the valuable discussions with Drs. Qing Cao, Boon Leng Cheong, Shaya Karimkashi, Jerry Crain and Michele Galletti. In addition, I would like to thank Drs. Robert Palmer, Yan (Rockee) Zhang, and Yang Hong for being my committee members.

Second, I would like acknowledge the following people for their friendship during my graduate study: Dr. Xinyi Shen, Dr. Youcun Qi, Dr. Shang Wang, Dr. ZhengZheng Li, Dr. Fanxing Kong, Redmond Kelley, John Meier, Ying Bai, Qing Zhao, Dr. Brad Isom, Benjamin Root, Dr. Sheng Chen, Dr. Xianwu Xue, Krysta Bruehl, Jo Ann Mehl, David Bodine, Tim Bonin, Petar Bukovcic, Jim Kurdzo, Feng Nai, Serkan Ozturk, Eric Jacobsen, Yu Pan, Hernan Suarez and Dr.Yu Zhang.

Finally, I want to give my most gracious gratitude to my family, my husband, Yinguang Li, and my 2-year old son, Xunze (William). Their support and encouragement make all this work possible.

## Table of Contents

## List of Figures

## Abstract

Planar or Cylindrical Phased Arrays are two candidate antennas for the future polarimetric weather radar. These two candidate antennas have distinctly different attributes when used to make quantitative measurements of the polarimetric properties of precipitation. Of critical concern is meeting required polarimetric performance for all directions of the electronically-steered beam. The copolar and cross-polar radiation patterns and polarimetric parameter estimation performances of these two phased array antennas are studied and compared with that obtained using a dual polarized parabolic reflector antenna.

Planar Polarimetric Phased Array Radar (i.e., PPPAR) creates biases in observed polarimetric parameters when the beam is pointed off broadside. The biases of polarimetric parameters with a PPPAR are presented, and it is unacceptably large. Thus, a bias correction matrix needs to be applied for each beam direction. A bias correction matrix is developed for array elements consisting of either dipole, waveguide apertures or patches. Correction matrices are given for both the Alternate Transmission and Simultaneous Reception mode and the Simultaneous Transmission and Simultaneous Reception mode. The PPPAR, however, has significant deficiencies for polarimetric measurements, as well as other limitations, such as increases in beamwidth, decreases of sensitivity, and high geometrically projected cross polar fields when the beam scans off its broadside. The Cylindrical Polarimetric Phased Array Radar (i.e., CPPAR) is proposed to avoid these deficiencies. The CPPAR principle and potential performance are demonstrated through theoretical analysis and simulation. It is shown that the

CPPAR has much lower geometrically induced cross-polar fields and less bias of polarimetric parameters than those of PPPAR. Array lattices, element separations, and error effects of CPPAR are examined.

# Chapter 1 Introduction

The USA's network of singularly polarized (i.e., linear horizontal) weather radar (i.e. the WSR-88D) has been updated to simultaneously transmit and receive vertically (i.e., the electric field lies in the vertical plane) and horizontally polarized waves of equal intensity along the beam axis (i.e., boresight). Dual polarization can provide additional information to the single polarization radar (Bringi and Chandrasekar 2001; Doviak and Zrnić 2006, section 8.5.2). The additional measurement of differential reflectivity $Z_{DR}$ can provide previously unavailable information on precipitation particle size and shape. The additional measurement of specific differential propagation phase $K_{DP}$ can be used to correct for cumulative attenuation due to rain along the path. The additional measurement of the copolar correlation coefficient $\rho_{hv}$ depends mainly on the variability in the ratio of vertical-to-horizontal size of individual hydrometeors, but it can also be affected by non-Rayleigh scattering. The $\rho_{hv}$ is a good indicator of regions where there is a mixture of precipitation types, such as rain and snow. Quantitative precipitation estimation (QPE) is improved by dual polarization radar parameters. By using the R-(Z, $Z_{DR}$, $K_{DP}$) relation, the accuracy of rainfall rate estimation was improved by 40% over the traditional R-Z relation (Brandes et al. 2002; Ryzhkov et al. 2005). Moreover, the dual polarization information is used to classify hydrometeors (e.g., rain, hail, snow, etc.; (Liu and Chandrasekar 2000; Vivekanandan et al. 1999; Zrnić et al. 2001), and non-weather objects (e.g. ground clutter, insects, birds, etc.; (Park et al. 2009; Steiner and Smith 2002) by fuzzy logic techniques. Moreover, polarimetric radar can be used to retrieve the microphysical properties of cloud and precipitation (e.g., drop size distribution, particle size, particle shape, etc.; (Zhang et al. 2001)). Radar polarimetry

with dual H & V polarizations, with proven benefits of more accurate rainfall rate measurements and classification of weather radar echoes, has recently been implemented on the national network of WSR-88D Doppler radars (Darcy 2012).

Meanwhile, phased array radar technology has been successfully utilized in weather surveillance with the milestone of the nation's first phased array weather radar-----the National Weather Radar Testbed (NWRT). Its potential in weather surveillance has been recognized by the meteorological and radar communities. The volume update time for surveillance by a four-faced PAR is less than one minute whereas the volume update time for the WSR-88D is 5 minutes (Zrnić et al. 2007). For severe weather applications, studies have shown that PAR can extend the severe weather warning lead time from 10 to 18-22 minutes, which should reduce loss-of-life and injuries (http://www.nssl.noaa.gov/research/radar/par.php). Furthermore, PAR has the capability to quickly re-scan areas with the most severe weather; therefore, it could further increase the warning lead time. The Multi-mission Phased Array Radar (MPAR) concept was introduced by Weber et al. (2007). A Multi-mission Phased Array Radar (MPAR) is being considered as a future replacement to simultaneously serve the functions of weather and aircraft surveillance at a significant lifetime cost savings while providing significant improvement in weather surveillance performance. For example, a four-faced planar PAR antenna with electronic beam steering allows simultaneous transmissions to and receptions of echoes from four sectors, and time multiplexing of radar assets allows multi-mission surveillance of aircraft and weather (Zrnić et al. 2013). Time multiplexing missions preserves the required update time needed to track

aircraft while scanning, and potentially provides faster update rates of hazardous weather. Moreover, more rapid volumetric scans can improve forecasts of a storm's evolution based on numerical weather prediction (NWP) models, and thus warnings can be based on forecasts, rather than on detection of the hazard itself (Dawson II et al. 2012; Yussouf et al. 2013). Furthermore, an MPAR could reduce the total number of radar sites because one radar network could be used for surveillance of both weather and aircraft (Weadon et al. 2009; Weber et al. 2007; Zrnić et al. 2007), and thus there is a potential to reduce the usage of spectrum space (Zrnić et al. 2012). Because of these advantages, a PAR is expected eventually to replace the mechanically steered beams of radars using parabolic reflector antennas.

If an MPAR is to be used for weather observations, the weather community expects to have not only the adaptive and rapid scan capability of a PAR, but all of the present capabilities of the polarimetric WSR-88D (Smith et al. 2008; Zrnić et al. 2007). It is the polarimetric capability that the 2nd MPAR Symposium (http://www.ofcm.noaa.gov/mpar-symposium, 17-19 November, 2009, Norman, OK) identified as the most challenging technical issue for the future Polarimetric Phased Array Radar (PPAR). It would be ideal for the PPAR to have, as does the WSR-88D for any beam direction, the vertically polarized wave field $E_\theta$ only (i.e., copolar $E_\theta$ and no cross-polar $E_\phi$) transmitted if the V port of the antenna is excited, and horizontally polarized wave field $E_\phi$ only (i.e., copolar $E_\phi$ and no cross-polar $E_\theta$) transmitted if the H antenna port is excited. This ideal condition is practically achieved along boresight with the parabolic reflector of the WSR-88D. This ideal condition of the polarization

orthogonality is theoretically also achieved for Planar PPAR (PPPAR) only if the array element is a pair of ideal collinear magnetic and electric dipoles (Crain and Staiman 2007; Zrnić et al. 2012).

But if the PPPAR has common H and V array elements, as do most PPPARs, this ideal property is not attained and the wanted copolar and unwanted cross-polar fields are transmitted along boresight (Zhang et al. 2009). That is, if the beam is electronically steered away from the cardinal planes, cross-polar beams coaxial with the copolar beam are formed, as shown in Chapter 2 and Chapter 3. Cross-polar beams coaxial with the copolar beams can create large biases, as noted by Zrnić et al. (2010). This unwanted or geometrically induced cross-polar field cannot be ignored if it significantly biases estimates of polarimetric parameters (e.g., $Z_{DR}$ bias needs to be less than 0.1 dB; (FAA 2013)).

For PPPAR, corrections for each beam direction are needed to suppress biases, especially those large biases created when the beam is steered away from the principal planes of the array, to provide accurate quantitative measurement of the polarimetric properties of precipitation. Urkowitz (2006) first noted corrections can be made in the receiver and suggested that the corrections determined from calibrations be applied to the receiving signals during weather data collection. Zhang et al. (2009) theoretically derived the biases of polarimetric parameters assuming crossed dipoles as an array element and showed the biases are larger than those specified for acceptable polarimetric parameter estimates. In Zhang et al.'s article, correction is provided either

to a scattering matrix or to radar variables by jointly solving the polarimetric parameters $Z_{DR}$ and $\rho_{hv}$. These corrections apply to beams of infinitesimal width for which only the cross-polar fields along the boresight are considered in bias calculation. Lei et al. (2013) developed bias corrections for a PPPAR consisting of an array of idealized aperture and patch elements, and again cross-polar fields only along the boresight are considered. Staiman (2009) applied the Zhang et al.'s PPAR bias correction to differential reflectivity. The engineering demonstration of bias correction has been done by Fulton and Chappell (2010), in which the polarization correction is applied to eight 10-cm wavelength dual-polarized elements of a phased array to form an active Digital Array Radar (Darcy 2012) prototype system. Sikina and Trott (2010) examined the issue in terms of a unit radiating cell. Zrnić et al. (2011) showed the need to decouple the effects of Doppler velocity from polarimetric parameters in the bias correction when the ATSR mode of data collection is used. Doviak et al. (2011) used the NWRT to experimentally verify the theoretically deduced cross-polar fields generated by beams electronically steered away from the cardinal planes.

A Cylindrical PPAR (CPPAR) is proposed to considerably reduce the cross-polar radiation that is the source of bias in the measurement of polarimetric parameters (Zhang et al. 2011). CPPAR has the characteristics of polarization purity and scan invariant beam. The horizontal and vertical polarized wave fields will be orthogonal in all beam directions. The CPPAR would essentially eliminate the beam-to-beam calibration that is required for a PPPAR. In azimuth, the mainlobe is always at broadside, and scan is achieved by shifting the column of active elements. The

characteristics and polarimetric parameters of CPPAR will be discussed in detail in Chapter 4.

As mentioned above, theoretical bias corrections of polarimetric parameters to be measured with an array of crossed dipole elements has been studied (Zhang et al. 2009). However, more practical radiation elements need to be considered. For example, the first 10 cm-band weather PAR, the NWRT, uses waveguide apertures as the radiating elements, but it only transmits vertically polarized waves. Rapid-DOW (Doppler on Wheels) and TRMM (Tropical Rainfall Measuring Mission)/GPM (Global Precipitation Measurement)'s PR (Precipitation Radar)/DPR (Dual-frequency Precipitation Radar) also use aperture antenna elements (Wurman and Randall 2001). Although the patch element is widely used in communications, it is still new for weather PAR. In this dissertation, bias correction for aperture and patch antenna elements of a PPAR is studied, and the similarity and differences of the biases between these radiation elements and dipoles is discussed. The theoretical patch using the cavity model (Lei et al. 2013) and more realistic patches for which radiation patterns are calculated by a full wave analyzer (e.g. HFSS) are considered and compared.

Zrnić et al. (2010) and Galletti and Zrnić (2011) examined cross-polar fields of a reflector antenna and assumed that copolar and cross-polar fields can be modeled by Gaussian shaped beams in which the cross-polar field over the entire angular space are used to obtain the $Z_{DR}$, $\phi_{DP}$, and copolar correlation coefficient, $\rho_{hv}$, biases. Herein we also calculate biases of polarimetric parameter estimates (i.e., differential reflectivity

$Z_{DR}$, the magnitude of copolar correlation coefficient, $\rho_{hv}$ and differential phase $\phi_{dp}$) obtained with PPPAR and CPPAR over the entire angular space. and compare these biases to those incurred if an ideal center-fed parabolic reflector is used, one having the size, shape of the WSR-88D, but not the narrow ridges of sidelobes due to the three feed support structures; such sidelobes are absent in the radiation from PPARs and parabolic reflectors having offset feeds (Bringi et al. 2011). Henceforth we refer to this ideal WSR-88D simply as the WSR-88D, having a diameter $D$ of 8.54m and an $f/D = 0.375$ ($f$ is the focal length). Results are calculated for operation at a wavelength of 11.09 cm used by KOUN, NSSL's R&D WSR-88D, so theoretical radiation patterns can be compared with measurements. All three antennas are assumed to have identical aperture distributions. An objective of this dissertation is to determine angular scan limits on CPPAR and PPPAR to make polarimetric measurements with acceptable bias without beam to beam calibration while preserving the performance standards of the WSR-88D.

The differences of the WSR-88D, PPPAR and CPPAR copolar and cross-polar radiation patterns are discussed in Chapter 2 and general formulas of polarimetric parameters are derived. In Chapter 3, polarimetric parameters bias and corrections of PPPAR are discussed. The biases given in Chapter 3 are also compared with the results given by Zhang et al. (2009), as well as with those biases presented by Zrnić et al. (2010) and Galletti and Zrnić (2011) for an ideal center-fed parabolic reflector antenna. In Chapter 4, CPPAR characteristics and bias corrections are discussed. Biases are recalculated if partial corrections are applied, as suggested by Zrnić et al. (2010), to account for differential changes of H and V copolar gains of the array element's

radiation patterns as the beam is scanned. In Chapter 5, we study the multi-faced cylindrical array and find the design trade-offs. And we present multi-phased cylindrical array's polarimetric radar parameter biases. Conclusions and discussions are provided in Chapter 6.

# Chapter 2 Comparisons of the WSR-88D, PPPAR, and CPPAR radiation patterns

## 2.1 Description of the antennas

The WSR-88D radar has a parabolic reflector antenna with a diameter of 8.54m (Figure 2-2a) and a copolar beamwidth of about 1°. If the planar array is to provide angular resolution at least as good as that of the WSR-88D for all pointing directions, each beam of the four-beam planar array (Figure 2-2b; only one beam is shown) requires an array having an elliptical shape with a 8.54/cos(45°) meter horizontal length $2R_y$ and a 8.54 meter vertical length $2R_z$ (i.e. azimuthal beamwidth needs to be 1° at the largest azimuth electronic scan angle of 45°, and sidelobes at further angles beyond 10° need to be below -50 dB). There is a small loss of angular resolution as elevation angle increases, but the increased beamwidth compensates for the gaps that presently exist in elevation coverage of the WSR-88D volume scans. Each face of the PPAR electronically steers the beam $\pm 45^o$ in azimuth and at least $0^o$ to $20^o$ in elevation over which quantitative estimates of weather should nearly match or exceed that of the WSR-88D.

A four-sector CPPAR has a 8.54/cos(45°) meter diameter and a 8.54m vertical dimension (Figure 2-2c). Each $90^o$ sector of the CPPAR generates one of four beams (one is shown) which are always azimuthally separated by $90^o$ as the beams are synchronously steered in azimuth by commutating the aperture distributions column by column. The vertical beamwidth of the PPPAR and CPPAR increases slightly—6%—with elevation angles between 0 and $20^o$; it is assumed this increase in beam width with

elevation angle is acceptable for all MPAR functions, and estimates of H and V reflectivities.

Given the distribution of the electric field across the aperture of the WSR-88D's parabolic reflector, and given the far field of the array element and the weight applied to each of the elements to approximately match the radiation pattern of the WSR-88D, the theoretical far field radiation patterns can be computed for each of the radars and compared with available experimental results.

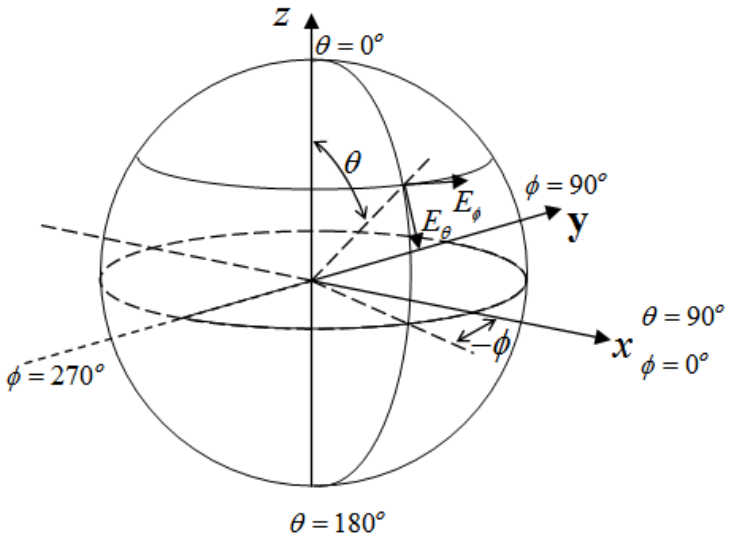


**Figure 2-1** A spherical coordinate system with a vertical polar axis is used to plot radiation patterns; variables used in this dissertation are also defined.

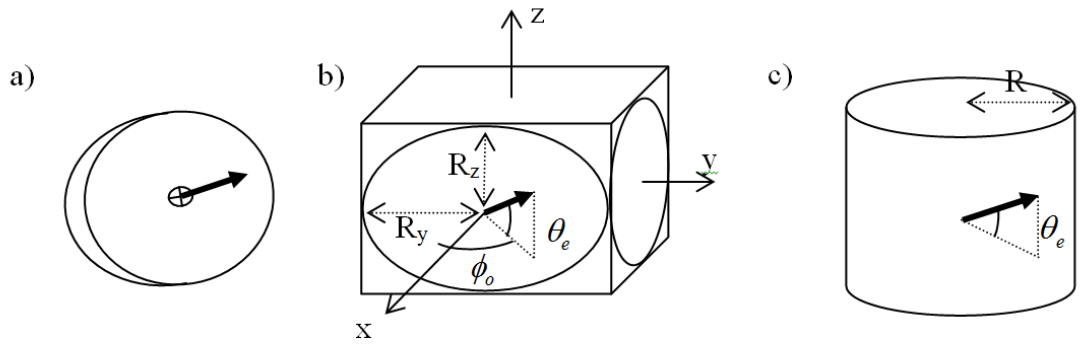


**Figure 2-2** (a) the WSR-88D center fed parabolic reflector, (b) a four-faced planar array, and (c) a four-sector cylindrical array. Single-sided bold arrows indicate beam direction.

## 2.2 Aperture distribution and element weightings

The WSR-88D feed horn's E field is nearly axial symmetric, and the normalized amplitude electric field across the aperture is well approximated by

$$W(\rho) \simeq \frac{\left[1-(\rho/\rho_o)^2\right]^a + b}{1+b} \tag{2-1}$$

where $\rho_o$ = 4.77 m, $a$ =3, and $b$ = 0.16 (Doviak et al. 1998). This aperture distribution was computed for KOUN, a prototype dual-polarimetric WSR-88D, which used a dual port circular feed horn having predominately a $TE_{11}$ electric field distribution across its aperture—this aperture field suppresses much of the cross-polar field generated by the reflector (Appendix A and Fradin 1961,section 8).

### *2.2.1 PPPAR*

To mimic the aperture distribution of the WSR-88D (Doviak et al. 1998), the amplitude weights $w_{mn}$ applied to the $mn^{th}$ element of the PPPAR are

$$w_{mn} = \frac{\left[1-\left(\frac{y_n^{\,2}}{R_y^{\,2}}+\frac{z_m^{\,2}}{R_z^{\,2}}\right)\right]^a + b}{1+b} \tag{2-2}$$

where $y_n$ is the horizontal distance of the n$^{th}$ column from the center of the elliptical array and $z_m$ is the vertical distance of the m$^{th}$ row from the center of the elliptical array. Thus PPPAR projected aperture distribution matches that of the WSR-88D only for the beam at $\theta_o$ = 90$^o$, $\phi_o$ = 45$^o$. Thus the PPPAR has higher azimuth resolution everywhere else in the domain of interest, but a slightly lower elevation resolution for beam elevations less than about 20$^o$.

Electronically scanning arrays are presented with the problem where there are changes in the H and V gains as the beam scans (Zhang et al. 2009). These gain changes contribute to biases in reflectivity factor Z, as well as differential reflectivity, $Z_{DR}$, because gain changes are not necessarily equal and depend on beam direction. These contributions to bias in polarimetric parameter estimates can be partially eliminated by adjusting the excitation of the H and/or V ports to equalize the received copolar H and V voltages for each beam direction—these adjustments are presented in Chapter 3 and 4.

*2.2.2 CPPAR:*

The weights $w_{mn}$ applied to the elements of the CPPAR are (Zhang et al. 2011):

$$w_{mn} = \frac{\left\{1-4\left[\frac{R^2\sin^2(\phi_o-\phi_n)+z_m^2}{D^2}\right]\right\}^a + b}{1+b} \tag{2-3}$$

where $R$ = 6 m is the radius of the cylinder, $z_m$ is the vertical distance of m$^{th}$ row from the center of the cylinder, $D$ = 8.54 m is axial length of the cylindrical array, and the CPPAR beam is pointed in the $(\theta_o, \phi_o)$ direction. $\phi_n$ is the azimuth angle of the n$^{th}$ column relative to the azimuth $\phi_0$ of the beam (Figure 2-2c). As with the PPPAR, to match the aperture distribution of the WSR-88D, $a$ = 3 and $b$ = 0.16. The match is approximate because we have not compensated weighting for the change of the density of elements projected onto the vertical plane perpendicular to the broadside direction, nor have we compensated for the change in element gain as the n$^{th}$ column of elements is at increasing angular distance from the broadside direction—herein called element rotation compensation. Nevertheless, as we shall see, the radiation patterns of the CPPAR are reasonably matched to those of the WSR-88D.

### 2.3 The array elements

As mensioned in the introduction, dipole antennas have been studied by Zhang et al. (2009). And aperture antennas have been used in the NWRT, Rapid-DOW and TRMM/GPM's PR/DPR. And patch antennas have been considered as the most competitive choise recently. Thus the dual-polarization radiation elements studied in this dissertation are aperture and patch antennas. For the aperture antenna, only the ideal model is considered. For the patch antenna, both the ideal patch using the cavity model and the full-wave simulated patch are considered. The spherical coordinate system is chosen with its polar axis vertical at the dual-polarized radiating element located at the origin, and the PPPAR array face is in the y, z plane (Figure 2-1). For simplicity, the

mutual couplings between the two antenna elements are all neglected. The mutual coupling will cause positive or negative bias to the radar parameters.

*2.3.1 Ideal Aperture*

The aperture antenna is an open ended waveguide. By using the field equivalence principle, the actual sources can be replaced by the equivalent electric and magnetic current sources. For the aperture on an infinite flat electric, only the magnetic current density has non-zero values on the aperture surface (Fig. 12.5 in Balanis 1997). The calculations of the far field radiation for the aperture antenna on an infinite electric conducting ground plane are shown in Appendix A.

For a horizontally polarized rectangular aperture, the longer side lies along the z axis (Figure 2-3a). A $TE_{10}$ mode is assumed to propagate inside the waveguide feeding the aperture. To simplify the problem we assume the aperture is surrounded by an infinite ground plane. The cofactor $\frac{jke^{-jkr}}{4r}abE_o$ is used to normalize the electric field radiating from a horizontally polarized aperture (Appendix A):

$$E_{\phi}^{(h)} = \sin\theta \cdot f^{(h)}(\theta,\phi) \tag{2-4}$$

$$E_{\theta}^{(h)} = 0 \tag{2-5}$$

where,

$$f^{(h)}(\theta,\phi)=\frac{\left(\frac{\pi}{2}\right)^2\cos(\frac{k_0 a}{2}\cos\theta)}{\left(\frac{\pi}{2}\right)^2-\left(\frac{k_0 a}{2}\cos\theta\right)^2}\times\frac{\sin(\frac{k_0 b}{2}\sin\theta\sin\phi)}{\frac{k_0 b}{2}\sin\theta\sin\phi} \tag{2-6}$$

The superscript $^{(h)}$ denotes the radiated field is from the horizontally polarized aperture, and $k_0 = 2\pi/\lambda_0$ is the free space wave number.

For the vertically polarized aperture, the longer side lies along the y axis (Figure 2-3b). Similarly, a $TE_{10}$ mode and infinite ground plane are assumed. In this case the cofactor $\frac{jke^{-jkr}}{4r}abE_o$ is used to normalize the radiated field which is (Appendix A):

$$E_\phi^{(v)}=\cos\theta\sin\phi\cdot f^{(v)}(\theta,\phi) \tag{2-7}$$

$$E_\theta^{(v)}=-\cos\phi\cdot f^{(v)}(\theta,\phi) \tag{2-8}$$

where,

$$f^{(v)}(\theta,\phi)=\frac{\left(\frac{\pi}{2}\right)^2\cos(\frac{k_0 a}{2}\sin\theta\sin\phi)}{\left(\frac{\pi}{2}\right)^2-\left(\frac{k_0 a}{2}\sin\theta\sin\phi\right)^2}\cdot\frac{\sin(\frac{k_0 b}{2}\cos\theta)}{\frac{k_0 b}{2}\cos\theta} \tag{2-9}$$

Usually, if only the $TE_{10}$ mode exists in the aperture, the length $a$ is between 0.5 $\lambda_o$ and 1.0 $\lambda_o$, and $b$ is less than $a$. In this paper, a typical size of aperture is assumed (i.e., $a$ = 0.55$\lambda_o$, $b$ = 0.25$\lambda_o$). The layout of array of rectangular apertures could be an interlaced brick pattern of orthogonal rectangles. But to simplify the calculation, both the horizontally and vertically polarized apertures are assumed to be located at the origin.

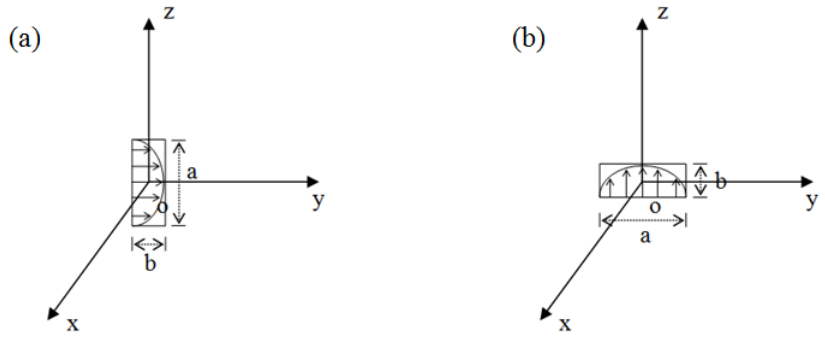


**Figure 2-3** Horizontally and vertically polarized apertures

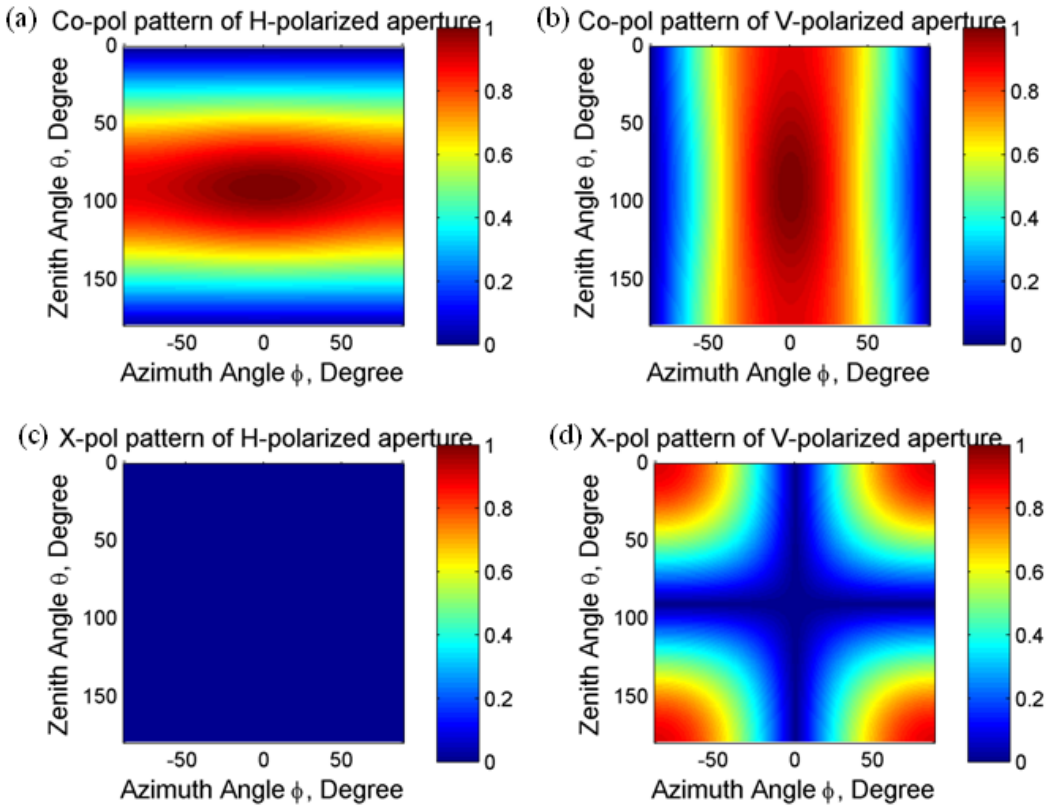


**Figure 2-4** Copolar and cross-polar electric fields for horizontally and vertically polarized apertures in an infinite ground plane, $a=0.55\lambda_o$, $b=0.25\lambda_o$).

The patterns of the electric field given by Eqns. (2-4) to (2-8) are plotted in Figure 2-4. The copolar and cross-polar patterns of horizontally polarized aperture are

shown in Figure 2-4a and c; and the copolar and cross-polar patterns of vertically polarized aperture are shown in Figure 2-4b and d. Because the polarization definition commonly used by radar meteorologists is definition 2 in Fig.1 of Ludwig (1973), the pattern of the vertically polarized aperture is not simply the pattern of the horizontally polarized aperture rotated 90° in y-z plane. In other words, radar meteorologists use $\mathbf{a}_\phi$ to represent the local H polarized field unit vector, and use $-\mathbf{a}_\theta$ to represent the local V polarized field unit vector (Bringi and Chandrasekar 2001, chapter 3; Zhang et al. 2009) (Figure 3-1); whether the H field is the copolar or cross-polar field depends whether the aperture is illuminated with H or V polarized waves (likewise for the V field). The cross-polar pattern (Figure 2-4d) of the V polarized aperture is given by Eqn. (2-7), and it shows that the vertical polarized aperture has an electrical field in the local horizontal direction (i.e. $\mathbf{a}_\phi$ in Figure 3-1) for directions away from the principal planes. However for radar observations of precipitation, this coupling from V to H is unwanted because hydrometeors typically have a vertical axis of symmetry, and thus hydrometeor properties are more easily measured using uncoupled H and V waves (Doviak et al. 1998, section III.1). Thus, this coupling needs to be accounted for and corrections need to be made to the observations in order to accurately characterize the type of precipitation and the measurement of its fall rate. In weather radars using mechanically steered parabolic reflectors (e.g., the WSR-88D), this coupling is typically negligible because the V and H are always aligned with the unit vectors $\mathbf{a}_\theta$ and $\mathbf{a}_\phi$ respectively.

*2.3.2 Ideal patch element*

A microstrip patch antenna consists of an electrically conducting ground plane, a substrate, and an electrically conducting patch on top, forming an open-ended cavity. If the substrate thickness is much thinner than the free space wavelength and the patch and ground plane are perfectly conducting, the four sides of this open-ended cavity can be modeled as perfect magnetic walls. In other words, the radiation field of a patch element can be calculated by assuming that the space below the patch is a resonant cavity bounded on two sides by walls (i.e., the patch and the ground plane) that perfectly conduct electric currents and on the other four sides by walls that perfectly conduct magnetic currents. Although the four open sides of the cavity leak radiation, only the two sides (i.e. radiating slots) perpendicular to the E-plane accounts for most of the radiation. This pair of sides acts like a pair of phased array aperture antennas in a two element array. For a square patch considered herein (Figure 2-5), the patch width is equal to the patch length (i.e., $W = L$). By the equivalence principle, the equivalent sources of the square patch are magnetic current densities having the same direction and value on the two opposing sides separated by length $L$ of the patch (Fig. 14.16 in Balanis 1997). Because the electric field fringes at the open ends, there is an effective patch length ($L_e$) separating the pair of magnetic current densities (i.e., $L_e$ is a little larger than the physical length $L$ (Eqn. (14.3) in Balanis 1997)). The difference between $L$ and $L_e$ is a function of patch dimension, PC board thickness, and substrate permittivity. Although the cavity model approximates the actual fields of the patch, it has been shown that input admittance, resonant frequencies, and the copolar radiation

patterns of the model cavity compare well with measurements (Balanis 1997, section 14.2.2).

For the square patch, the $TM_{010}$ and $TM_{001}$ modes (e.g. $TM_{010}$ is horizontal polarization; $TM_{001}$ is the vertical polarization) have the same resonant frequency. Both modes can be excited and coexist independently inside the patch. For small values of substrate thickness, the electric fields radiated from the horizontally polarized square patch are given by Eqn. (14-44) in Balanis (1997). In order to directly constitute the projection matrix in the next section, the cofactor $j\frac{2V_0 e^{-jk_0 r}}{\pi r}\cdot\frac{k_0 L}{2}$ is extracted out, so the normalized copolar electric field is:

$$E_{\phi}^{(h)} \approx \sin\theta \cdot g^{(\mathrm{h})}(\theta,\phi) \tag{2-10}$$

and the cross-polar field is

$$E_{\theta}^{(h)} \approx 0 \tag{2-11}$$

where,

$$g^{(\mathrm{h})}(\theta,\phi) = \frac{\sin(\frac{k_0 L}{2}\cos\theta)}{\frac{k_0 L}{2}\cos\theta}\cos(\frac{k_0 L_{\mathrm{e}}}{2}\sin\theta\sin\phi) \tag{2-12}$$

$V_0$ is the voltage across the open edges of the patch and the fringing fields at the edges account for most of the radiation.

Similarly, the cofactor $j\frac{2V_0 e^{-jk_0 r}}{\pi r}\cdot\frac{k_0 L}{2}$ is extracted out and normalized E fields of vertical polarized patch are calculated in Appendix A:

$$E_{\phi}^{(v)} \approx \cos\theta \sin\phi \cdot g^{(v)}(\theta,\phi) \tag{2-13}$$

$$E_{\theta}^{(v)} \approx -\cos\phi \cdot g^{(v)}(\theta,\phi) \tag{2-14}$$

Where

$$g^{(v)}(\theta,\phi) = \frac{\sin(\frac{k_0 L}{2}\sin\theta\sin\phi)}{\frac{k_0 L}{2}\sin\theta\sin\phi}\cos(\frac{k_0 L_e}{2}\cos\theta) \tag{2-15}$$

$L$ is the physical length of the square patch and is determined by the permittivity of the material in the cavity (typically $\lambda_o/3 < L < \lambda_o/2$). For an air substrate $L$ is $\lambda_o/2$; for high permittivity substrates $L$ approaches $\lambda_o/3$. The value of $L_e$ is assumed to be $L/0.95$, one commonly used in practice. Eqns. (2-10), (2-11), (2-13), and (2-14) are plotted in Figure 2-6 for one example of patch dimension (i.e. $L = 0.38\lambda_o$ and $L_e = 0.40\lambda_o$). The co- and cross-polarization patterns are not simple versions of one another simply rotated by $90^o$ when the patch excitation is rotated by $90^o$. This is because the coordinated system that defines the co-and cross-polar fields does not rotate (See definition 2 in Fig.1 of Ludwig (1973).

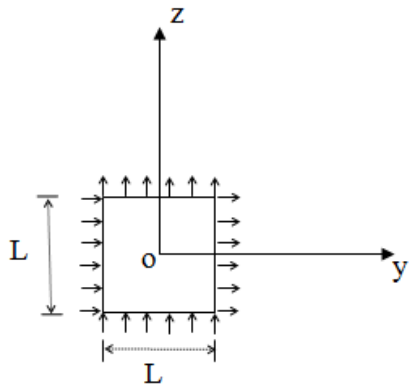


**Figure 2-5** Dual-polarized ideal square patch.

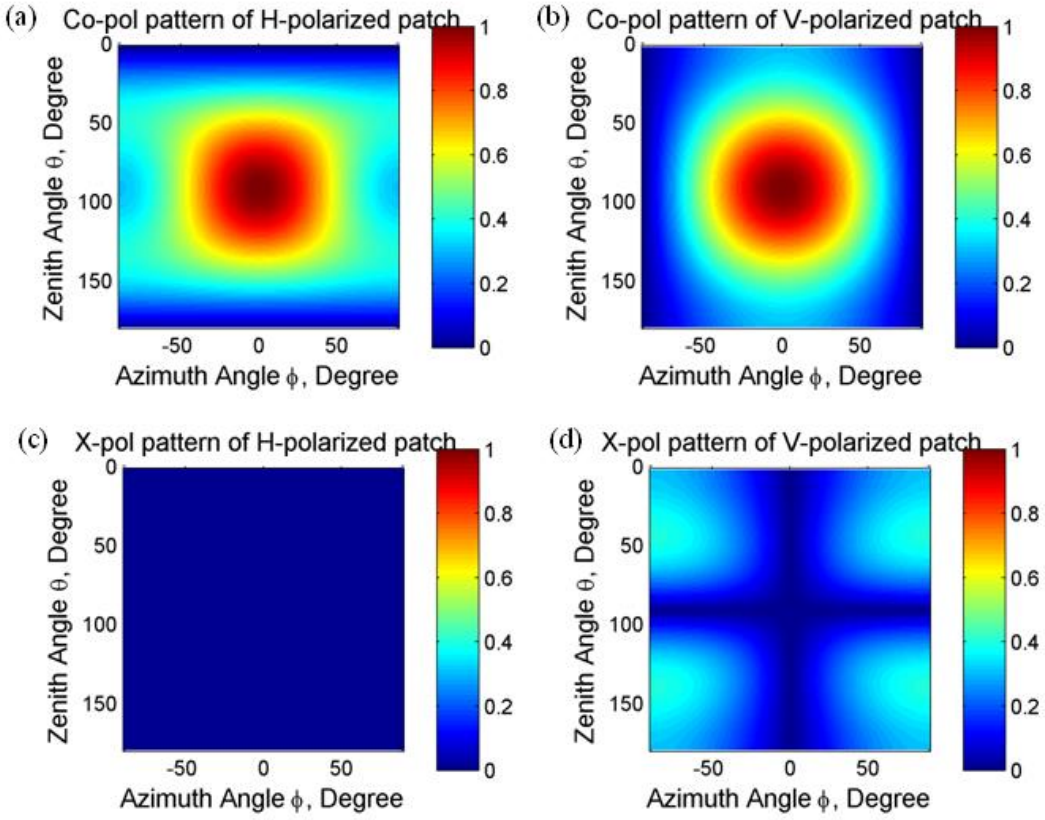


**Figure 2-6** Co and cross electric fields of horizontally and vertically polarized ideal patches (physical length: $L = 0.38\lambda_o$, effective length: $L_e = 0.40\lambda_o$).

The four open sides of the cavity leak radiation, radiating slots account for most of the radiation. However, the other two sides, called non-radiating slots, also contribute to the radiated field. Radiation fields of non-radiating slots of vertically polarized patch are derived in chapter 14 in Balanis (1997). Radiation from the non-radiating slots of horizontally polarized patch can be found in Appendix A. A comparison of the radiation fields of an ideal patch (considering both radiating and non-radiating slots) and the full wave (HFSS) simulated patch is in Appendix D. They are almost the same, and the slight difference is due to the fact that higher order mode exists in full wave analysis while only the base mode is assumed to exist in the ideal patch.

*2.3.3 Full wave simulated patch*

The full wave simulated antenna elements considered in this dissertation is a single layered $0.321\lambda$ square probe-fed patch on a substrate with a permittivity of 2.2 and a thickness of $0.0142\ \lambda$ with a ground plane size $0.81\lambda$ (Figure 2-7a). The substrate size is as large as the ground plane. The probe feed location is $0.045\lambda_o$ to the center of the patch and the probe feed has an inside center conductor with radius of $0.0039\ \lambda_o$ and outer conductor with radius of $0.0090\ \lambda_o$. The element separation is $0.5\lambda_o$ for both the PPPAR and CPPAR, and the mutual coupling between elements is neglected. Although the radiation patterns of a patch on a finite ground plane differ from those patterns of a patch on a conducting cylindrical or planar surface, and although mutual coupling will alter the radiation pattern of the patch embedded in the array, the methodology presented herein can use the embedded radiation pattern of patches mounted on realistic structures.

The HFSS (ANSYS) is used to compute the copolar and cross-polar radiation fields of the patch. . The H and V copolar and cross-polar patterns of the array are obtained by coherently adding the fields from each element of the array for both the CPPAR and PPPAR—an array factor could have been used for the PPPAR but not for the CPPAR (Josefsson and Persson 2006, chapter 2); thus realistic mainlobe and sidelobes are considered.

It should be noted that the probe-fed excitation of the patch antenna element generates higher order standing wave modes, although of lesser intensity than the fundamental $TM_{010}$ and $TM_{001}$modes in the open-ended patch cavity (e.g. $TM_{010}$ generates copolar H fields; $TM_{001}$ generates copolar V fields). These higher order modes cause slightly asymmetrical radiation patterns as seen in Figure 2-7 (e.g. the horizontal null line in Fig. 3e is at about $\theta = 96^{o}$, not the $90^{o}$ it would have if only the fundamental mode was present; This can result in the array null slight shifted a little angle due to the asymmetric of element pattern). This asymmetrical radiation patterns can also be found in Bhardwaj and Rahmat-Samii (2014). However, because the H port probe is symmetry about horizontal line, the cross-polar null in Figure 2-7d is at $\theta = 90^{o}$ . Mirror arrangement of the patches can eliminate asymmetry, which should result in a lower cross-polar field along the horizontal plane as seen in experiments (Perera et al. 2014)

Figure 2-7b-e presents the patch's radiation field. $F_{\mathbf{vv}}^{(p)}$ is the copolar pattern of the V field ($E_{\theta}$) if the V port is energized and vice versa for $F_{\mathbf{hh}}^{(p)}$. $F_{\mathbf{hv}}^{(p)}$ is the cross-

polar H ($E_\phi$) pattern if the V port is energized and vice versa for $F_{\mathbf{vh}}^{(p)}$. Both copolar and cross-pol patterns in this dissertation are normalized by the copolar peak ($F_{\mathbf{vv}}$).

Comparing patch patterns of the full wave simulation (Figure 2-7) with an ideal one defined by Lei et. al. (Fig.4 in Lei et al. 2013), $F_{\mathbf{vh}}^{(p)}$ (Figure 2-7d) is not zero as it is for the ideal patch. $F_{\mathbf{vh}}^{(p)}$ is due to the so-called non-radiating slots (Balanis 1997, chapter 14). But for the cross-polar field $F_{\mathbf{hv}}^{(p)}$ (Fig. 3e) both radiating and "non-radiating" slots contribute to cross-polar $E_\phi$; the radiating slots cause the geometrically induced cross-polar field. The ideal patch patterns considering both the radiating slots and non-radiating slots agree very well with the HFSS simulated patch patterns (Appendix D). It should also be noted the copolar phases of realistic patterns are not necessarily equal and zero as assumed by Zrnić et al. (2010) and the phases can be a function of $\theta, \varphi$ etc. as is seen in the phase plots not shown here. Thus in our computation of biases the amplitude and phases of the copolar and cross-polar patterns, which are dependent on beam direction, are included.

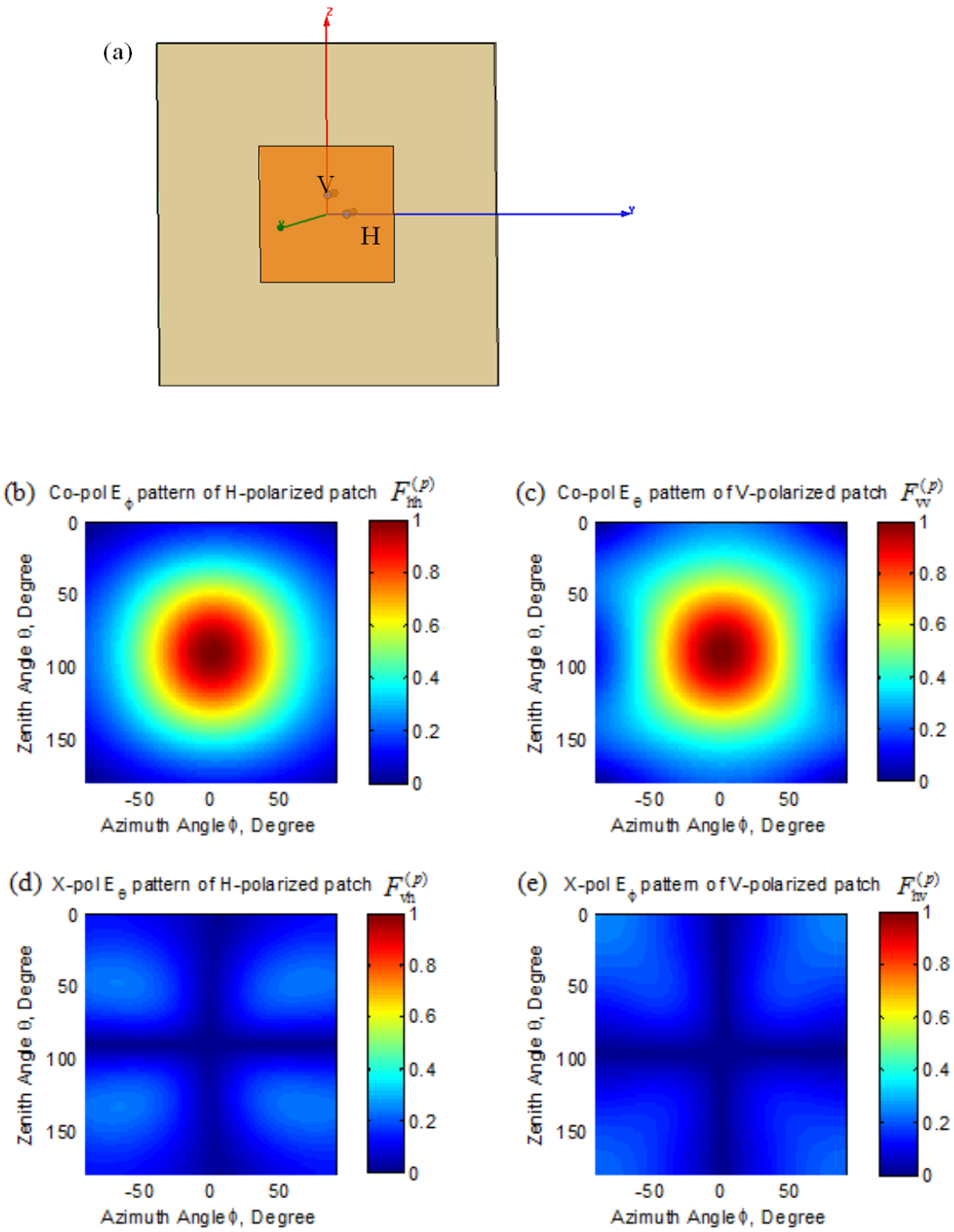


**Figure 2-7** HFSS simulated patch element radiation patterns normalized by the Copolar peak.

## 2.4 Theoretical radiation patterns of three polarimetric radars

Patterns of radiation from the WSR-88D, PPPAR and CPPAR are shown in Figure 2-8, Figure 2-9, Figure 2-10, and Figure 2-11 respectively. The sizes of antennas are given in the previous section "2.1 Description of the antennas". The antenna elements considered for arrays in this section—all the same for both the PPPAR and CPPAR—are the full wave simulated patch antennas discussed in this chapter. Tapers for arrays are given in the previous section "2.2 Aperture distribution and element weightings". Antnena element separation chosen for both PPPAR and CPPAR is 0.5 wavelengths. All patterns at broadside (can be slightly shifted at a small angle due to the asymmetric of element pattern) have type 2 cross-polar fields as defined by Zrnić et al. (2010)—a quad of 4 cross-polar peaks of alternating phase symmetrically located about the copolar beam. Only the PPPAR radiation pattern evolves into the type 1 cross-polar pattern (i.e., cross-polar radiation main lobe coaxial with the copolar beam) as the beam is steered away from the principal planes—it is the type 1 pattern that is the most effective in creating polarimetric parameter estimate bias.

For these four figures, the beam pointing elevation angle $\theta_e$ ($\theta_e = 90^o - \theta_0$) for all three antennas is chosen to be at 20° which is typically the highest elevation angle for weather radar, and the azimuth for all three beams is $\phi_o$ = 45°. This limit of the scanned sector gives the condition for maximum bias and gain change. All patterns of radiation are presented using the coordinate system of Figure 2-1. $F_{vv}$, etc. are elements for the electric field radiation matrix $\vec{\vec{\mathbf{F}}}$ defined by Zrnić et al. (2010). For the phased array, $\vec{\vec{\mathbf{F}}}$ includes both element factor and array factor, but it does not include any

adjustments to the projection loss nor for the change in the density of elements projected onto the vertical reference plane perpendicular to the broadside direction of the CPPAR. That is, the aperture distribution of the CPPAR does not quite match that of the WSR-88D. $F_{\mathbf{vv}}$ is the copolar pattern of $E_\theta$ if the V port is energized and vice versa for $F_{\mathbf{hh}}$. $F_{\mathbf{hv}}$ is proportional to the cross-polar H field ($E_\phi$) if the V port is energized and vice versa for $F_{\mathbf{vh}}$. Both copolar and cross-pol patterns in this dissertation are normalized by the copolar peak $F_{\mathrm{vv}}$ along the beam axis. Moreover, $F_{\mathrm{ij}} = \sqrt{g_{\mathrm{ij}}}\, f_{\mathrm{ij}}(\theta,\phi;\theta_0,\phi_0)$, where $f_{\mathrm{ij}}(\theta,\phi;\theta_0,\phi_0) = \left| f_{\mathrm{ij}}(\theta,\phi;\theta_0,\phi_0)\right| \exp\left[ j\gamma_{\mathrm{ij}}(\theta,\phi;\theta_0,\phi_0)\right]$ in the coordinated system of Figure 2-1, radiation patterns are functions of beam direction.

*2.4.1 WSR-88D radiation patterns*

Patterns for WSR-88D are shown for the vertically polarized radiation and the patterns of the other polarization are identical for WSR-88D. The copolar and cross–polar radiation amplitude patterns of the WSR-88D are calculated using theoretical formulations and then compared with measurements — $F_{\mathrm{hh}}$ patterns are identical as $F_{\mathrm{vv}}$; $F_{\mathrm{hv}}$ patterns are identical as $F_{\mathrm{vh}}$. The theoretical formulations are given in Appendix **B.** Because the theoretical and measured patterns are given in $(r,\theta',\phi')$ spherical coordinate system in which the polar axis is along the beam axis, Appendix **C** gives the transformation to plot the WSR-88D radiation patterns in the $(r,\theta,\phi)$ spherical coordinate (Figure 2-1) used by radar meteorologists so meaningful comparisons can be made.

The theoretical patterns of WSR-88D pointing at $(\theta_o, \phi_o) = (70^o, 45^o)$ are shown in Figure 2-8. Although not apparent in these figures, the WSR-88D patterns are slightly distorted (i.e., not circularly symmetric in the $(\theta, \phi)$ displays) due to the coordinate system transformation (Appendix **C**) —the lack of circular symmetry is, however, evident in the sidelobe patterns. Four equal cross-polar main lobes have alternating phase and the copolar phase is a constant through all the angles (Figure 2-8c).

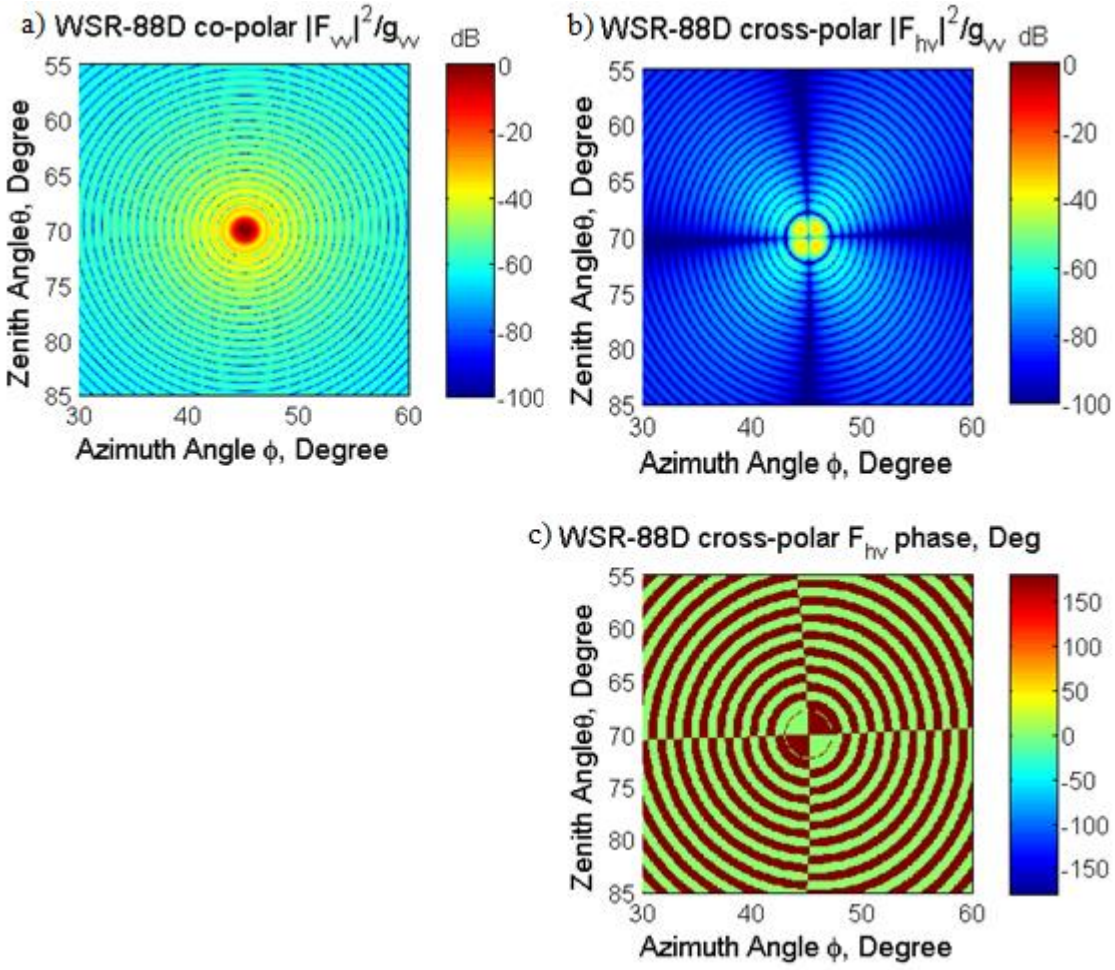


**Figure 2-8** The normalized theoretical one-way radiation patterns of the KOUN for a) the copolar $E_\theta$ , b) the cross-polar $E_\phi$, and c) the cross-polar phase. Wavelength $\lambda$ = 11.09 cm. Beam is directed at $\theta_o = 70^o$ and $\phi_o = 45^o$.

*2.4.2 The PPPAR radiation patterns*

The PPPAR patterns are calculated by multiplication of antenna element factor and array factor. The copolar and cross-polar fields are shown in Figure 2-9a and b. The cross-polar $E_\phi$ field pattern of the PPPAR has a main lobe coaxial with the copolar beam, and has a peak 12.4dB below the copolar peak at the mainbeam direction. Although not shown here, the cross-polar peak below the copolar peak of horizontal polarization is -11.2 dB. The cross-polar peak of horizontal polarization is larger than the cross-polar peak of vertically polarization because the antenna element cross-polar patterns are larger of horizontal polarization than that of the vertically polarization (Figure 2-7). As will be shown in Chapter 3 this geometrically induced cross-polar field and the difference of H and V gains causes significant bias. The copolar and cross-polar fields are the fields of the element pattern multiplied by the array factor. Thus the cross-polarization nulls of the element patterns remain along the principal planes ($\theta, \phi = 0^o$) and ($\theta = 90^o, \phi$) for ideal patch but these nulls slightly shift a few degree if the antenna element patterns are asymmetry which are shown and discussed in Fig. 3. Both the copolar and cross-polar beams have elliptical cross sections determined by the array factor. The orientation of the elliptically shaped beam, and the major to minor axis ratio is a function of beam direction—not so for the invariant circular beam of the WSR-88D. Figure 2-11a shows relatively good agreement of the mainlobe, even when $\theta_o$ = 70$^o$, $\phi_o$ = 45$^o$, but sidelobe locations differ. Although not shown, the broadside PPPAR beam has a higher gain and better azimuth resolution than the WSR-88D. This is because at broadside the aperture of the PPPAR is azimuthally larger than that of the WSR-88D (Figure 2-2). At $(\theta_o, \phi_o) = (90^o, 45^o)$, the PPPAR gain is the same as that of WSR-88D.

And the PPPAR gain with main beam pointing at $(\theta_o, \phi_o) = (70^o, 45^o)$ is 0.2 dB less than that of WSR-88D due to slightly less effective area. In Fig5c and d, the phase at boresight of copolar field is 72 degree and the phase at boresight of cross-polar field is 91 degree. This illustrates that gain as well as phases are a function of beam direction—thus corrections to eliminate bias will be a function of beam direction.

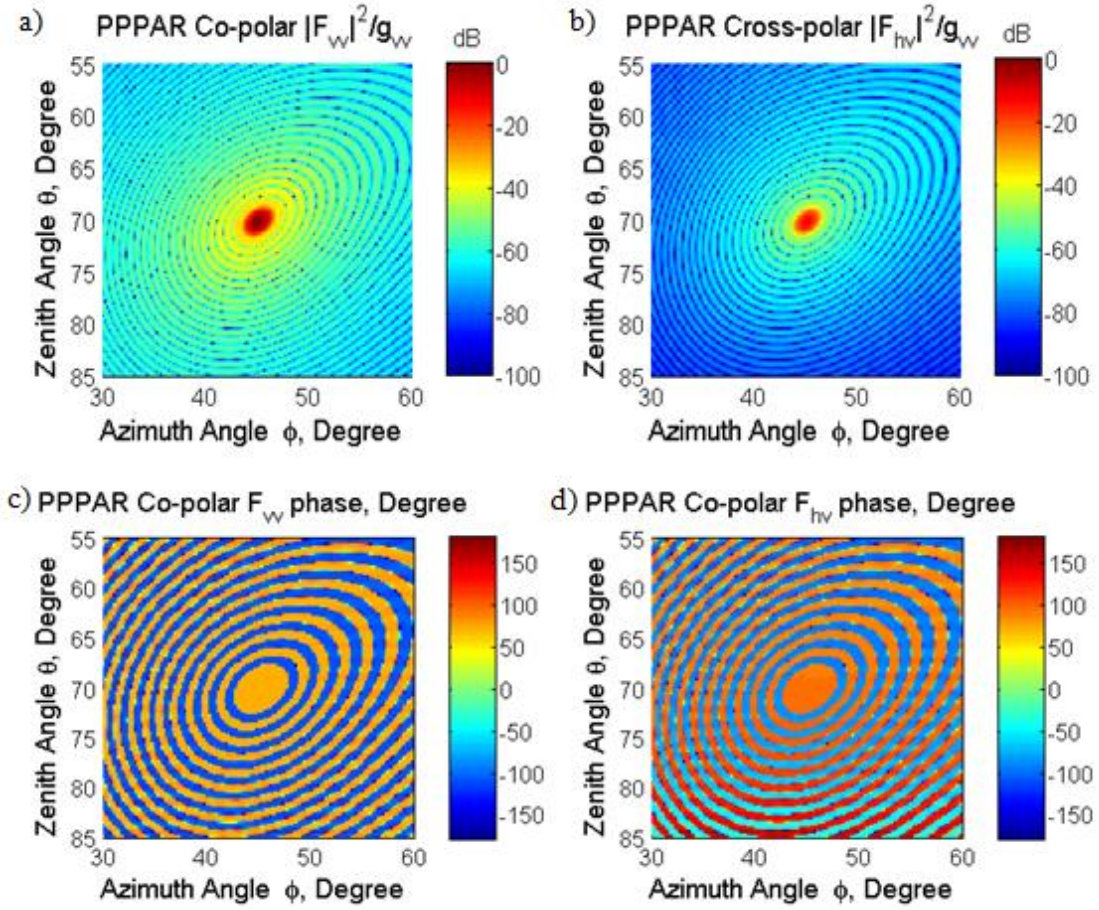


**Figure 2-9** The one-way power density patterns of a PPPAR array normalized by the gain at (45, 90°). a) the copolar $E_\theta$ field, b) the cross-polar $E_\varphi$ field, c) the copolar phase, and d) the cross-polar phase. Beam is directed at $\theta_o$ = 70° and $\phi_o$ = 45°.

*2.4.3 The CPPAR radiation patterns*

For any arbitrary shape of array, the electrical field with the mainbeam pointing at $(\theta_0, \phi_0)$ are given by

$$E(\theta,\phi) = \sum_{p=1}^{N} \left| w_p \right| EL_p(\theta,\phi) e^{ik\left[(x_p \sin\theta\cos\phi + y_p \sin\theta\sin\phi + z_p \cos\theta) - (x_p \sin\theta_0\cos\phi_0 + y_p \sin\theta_0\sin\phi_0 + z_p \cos\theta_0)\right]} \tag{2-16}$$

where $p$ is the index number of antenna elements ranging from 1 to N. $w_p$ is the amplitude weight for the p[th] element. $EL_p(\theta,\phi)$ is the element factor. If the elements distribute on a curved surface, $EL_p(\theta,\phi)$ varies for each element. Specificly, for cylindrical array, element factor is expressed as $EL(\theta, \phi - \phi_n)$, where $\phi_n$ is the azimuth angle of the n[th] column relative to the azimuth $\phi_0$ of the beam. $(x_p, y_p, z_p)$ are the location of p[th] element in a Cartesian cooridante system.

Figure 2-10 shows the copolar and cross polar radiation patterns with taper for the CPPAR. The weighting of array elements does not include compensation for element rotation nor for change of element density when projected onto the vertical plane centered on the central column of the active sector of the CPPAR. Thus the projected aperture distribution of the CPPAR does not match exactly that of the WSR-88D. Nevertheless, CPPAR gain at $(\theta_o, \phi_o) = (70^o, 45^o)$ is 0.2 dB less than that of WSR-88D gain due to less effective area. The copolar beams of the CPPAR and WSR-88D are reasonably matched at the extreme elevation angle of 20[o] (Figure 2-11b). Although not shown, the cross-polar field pattern of CPPAR with beam directed at 96.2[o] zenith

($90^o$ zenith angle for an ideal patch) has a quadrant of equal amplitude with mainlobes (about -36 dB) equally spaced around the copolar beam as does the WSR-88D which also has cross-polar peaks at about -36dB (Figure 2-11c). But unlike the WSR-88D for which the quad of 4 mainlobes do not change as elevation angle changes, the intensity of the pair of cross-polar peaks below the zenith angle $96.2^o$ plane (or horizontal principal plane for ideal patch) decreases in intensity, but the pair above, of equal amplitude and spaced about a half a beam width from the vertical principal plane, follows the copolar beam and increases in intensity with increase in elevation angle. The quadrant peaks condition shifts from being centered about a zenith angle $90^o$ for ideal patch to $96.2^o$ for simulated patch $\theta = 90^o$ (Figure 2-7) ); as stated earlier this is due to the asymmetrical pattern(Figure 2-7e) of the simulated patch caused by higher order modes in the patch cavity.

The vertical principal plane always bisects the cross-polar beam and forms a pair of cross-polar mainlobes of opposite phase and equal peak magnitudes of -24.9dB at $\theta_o = 70^o$. Whereas the PPPAR has a -12.4 dB boresight peak, the CPPAR cross-polar field is zero. Along the azimuth direction, the pair of cross-polar mainlobes (Figure 2-10b) are displaced from boresight by about 0.6° (Figure 2-11b), and each has a 3dB-beamwidth of about 0.6°. In the vertical direction the cross-polar mainlobes have a 3dB-beamwidth of about 1°.

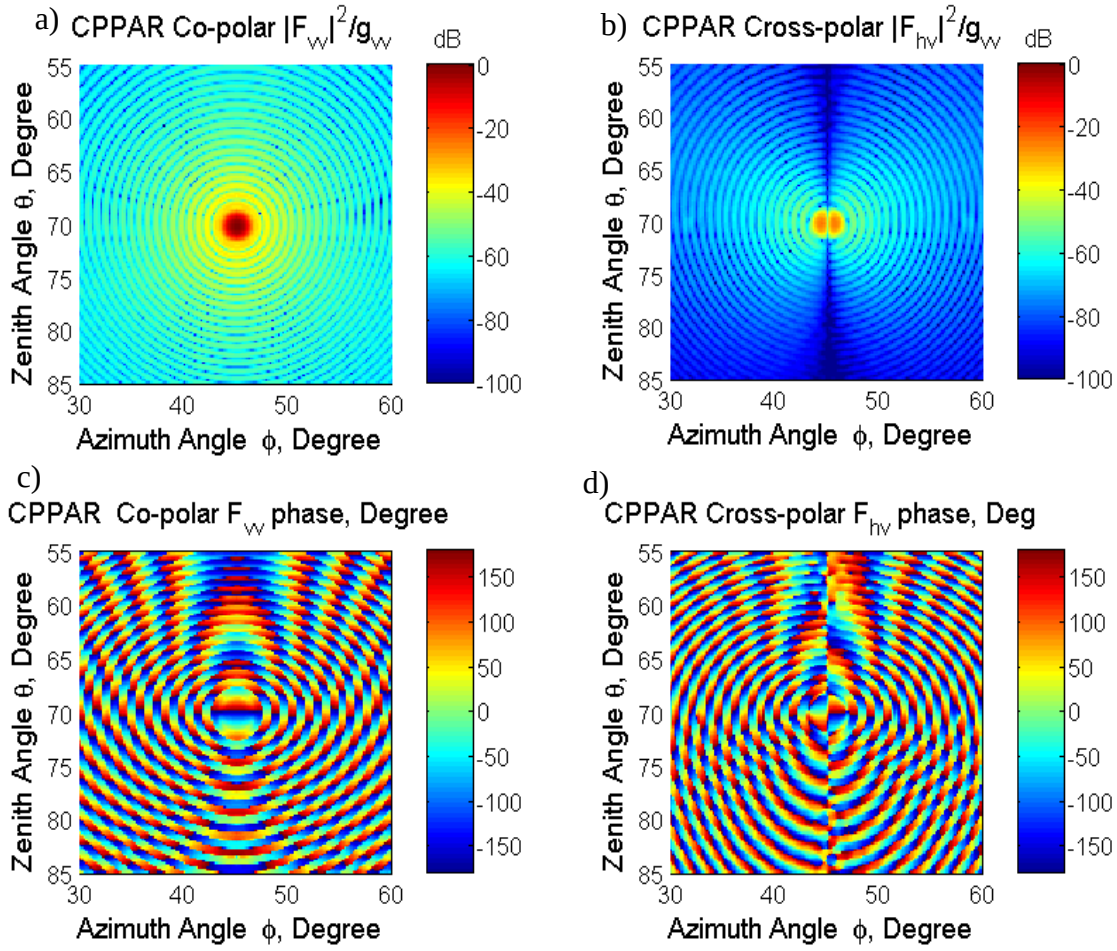


**Figure 2-10** The one-way power density patterns of the CPPAR array, normalized by gain $g_{vv}$. a) the copolar $E_\theta$ field and, b) the cross-polar $E_\varphi$ field, c) the copolar phase, and d) the cross-polar phase. Beam is directed at $\theta_o = 70^o$ and $\phi_o = 45^o$.

Because the CPPAR and WSR-88D have nearly the same aperture distribution, the copolar radiation patterns at broadside (i.e., $\theta_o = 90^o$, but any $\phi_o$) are nearly in agreement about the main lobe of the copolar beam—comparisons of these patterns (Figure 2-11b) show this to be true. Slight differences are due to the lack of compensation for changes in element density and gain due to element rotation. The

agreement would be better if the weights applied to the CPPAR elements included density and gain compensation (Zhang et al. 2011 ).

**2.5 Comparison of measured and theoretical radiation patterns**

The line plots in Figure 2-11a, b, and c compare the copolar and cross-polar radiation patterns of PPPAR, CPPAR and the WSR-88D at the limit of the scan region where the PPPAR geometrically induced cross-polar fields are the maximum.

In Figure 2-11a, the PPPAR copolar pattern is very similar to that of WSR-88D near the main lobe. The PPPAR pattern is not symmetrical about $\phi_o = 45^o$ in azimuth (as can also be seen from Figure 2-9), and the side lobes for PPPAR are slightly higher and sidelobe widths are slightly narrower at $\phi < 45^o$ rather than $\phi > 45^o$. These differences are due to the changes in the projection of the PPPAR's array area (e.g., larger for $\phi < 45^o$ than for $\phi > 45^o$).

The sidelobes of the WSR-88D were measured by Andrew Canada along the $30^o$ cut (Paramax 1992) ,and an eye-ball estimate of the envelope of these sidelobes at $\theta' > 2^o$ is shown with a dashed-dotted line (Doviak et al. 1998). This pattern cut lies midway between the narrow ridges of higher sidelobes (about 5 to 13 dB higher) due to the blockages by the spars and is therefore more representative of the sidelobe levels of the WSR-88D. The KOUN main lobe measurements (dots) are also obtained from Doviak et al. (1998).

The transformation in Appendix **C** is applied to the theoretical and measured data, and thus the beamwidth, in the $(\theta,\phi)$ coordinates of Figure 2-1 is slightly larger after the transformation. Specifically for measurement data in Figure 2-11, the azimuth beamwidth changed from $0.9^o$ at $(\theta_o,\phi_o)=(90°,0°)$ to $0.96^o$ at $(\theta_o,\phi_o)=(70°,45°)$ . Although the beamwidth of the WSR-88D measured in the spherical coordinate system with the polar axis along the beam does not change with elevation angle, it does change when measured in the coordinate system of Figure 2-1.

The CPPAR copolar pattern is very similar to that of WSR-88D near the main lobe (Figure 2-11b). Slight differences arise because for the beam at $(\theta_o,\phi_o)=(70°,45°)$ the CPPAR beam deviates slightly from the circular shape seen at broadside. WSR-88D sidelobe levels beyond $10^o$ azimuth are more than 50 dB below the copolar peak and are in agreement with measurements. The theoretical and measured sidelobe levels also agree well with the sidelobe levels measured for a dual-offset fed antenna having ultra-low sidelobes needed for weather radar research (Bringi et al. 2011). At the elevation angles of $0^o$, 20°, and $30^o$, the pair of CPPAR cross-polar peaks are -37dB, -25 dB, and -22 dB below the copolar peak. The cross-polar peaks of the dual-offset fed reflector are also two—versus the four for a center-fed parabolic antenna—and each has a peak gain at about -35.5 dB below the copolar gain (Bringi et al. 2011) similar to that for the CPPAR if the copolar beam is pointed at $\theta_o=90^o$.

The measured cross-polar Fhv field of WSR-88D can be found in Figure 2-11 in Zrnić et al. (2010), but it is reproduced in Figure 2-11c to compare with the theoretical

pattern computed in Appendix B and shown in Figure 2-8b. The line plot in Figure 2-11c is along $\phi' = 45^o$ and is plotted as a function of $\theta'$ ($\theta'$ and $\phi'$ are defined in Appendix B).

All the copolar patterns of CPPAR, PPPAR and WSR-88D agree well at angles near the main lobe. And the cross-polar levels for the CPPAR are much less than that for the PPPAR. On the other hand, $F_{hh}$, etc. are functions of beam direction for the PARs unlike that of the WSR-88D.

We show the patterns of WSR-88D, PPPAR, and CPPAR and make comparisons of pattern characteristics. By using the similar aperture size and the same taper discussed in previous sections, the normalized copolar patterns of phased arrays are almost the same as that of WSR-88D. However, the cross-polar patterns peak of PPPAR is high and CPPAR nature cross-polar patterns peaks are much lower than that of PPPAR and are more approaching the performance of WSR-88D. Those cross-polar fields of PPPAR can cause unacceptable large polarimetric radar parameter biases.

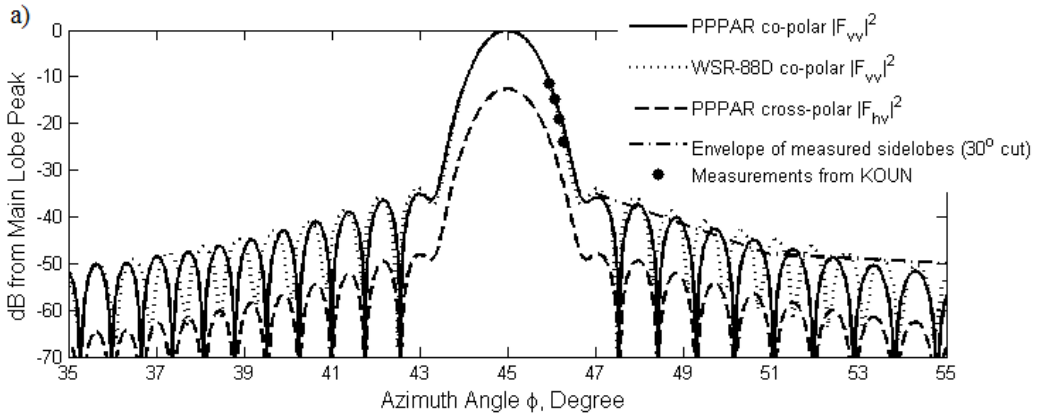

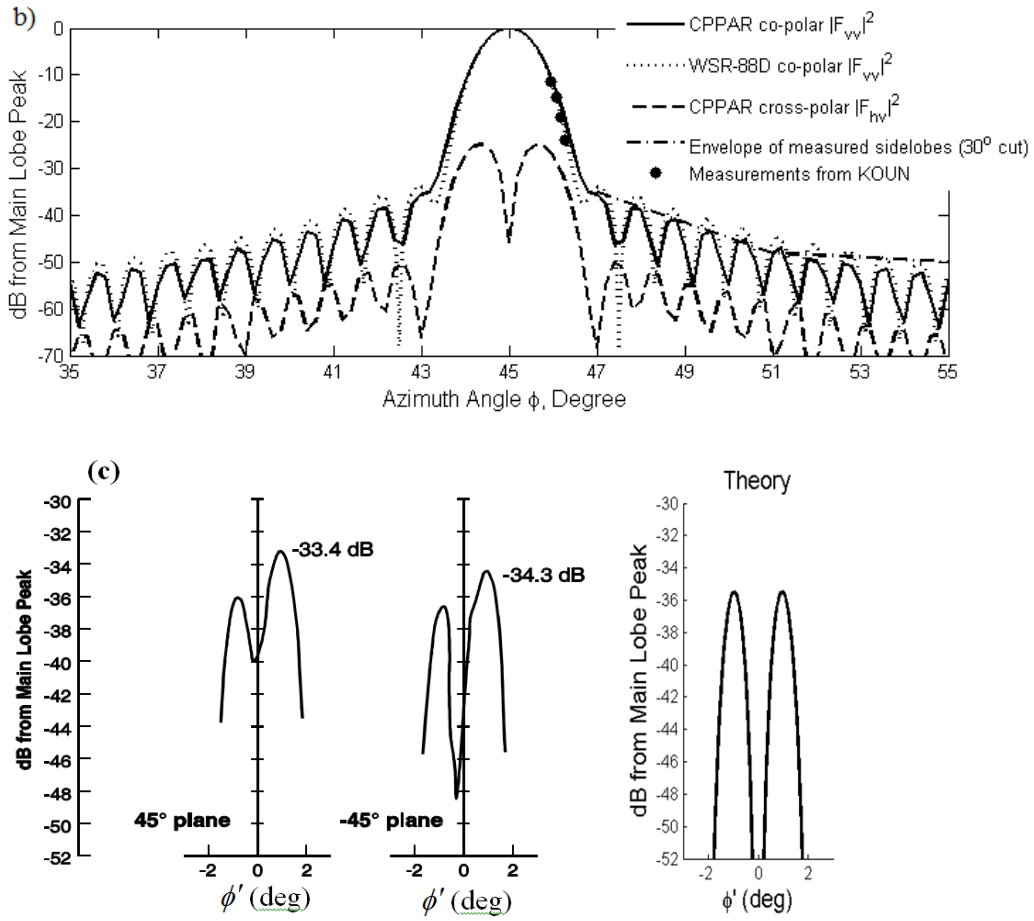


**Figure 2-11** Comparison of the theoretical and measured copolar $|Fvv|^2$ and cross-polar $|Fhv|^2$ radiation patterns of (a) PPPAR and WSR-88D, (b) CPPAR and WSR-88D; beam is directed at $\theta_0$ = 70° and $\phi_0$ = 45°, for frequency = 2905 MHz. (c) theoretical and measured $|Fhv|^2$ as a function of $\theta'$ for the WSR-88D along a $\phi' = \pm 45^o$ cut.

## 2.6 The biases of polarimetric radar parameters calculated by pattern integration

Zrnić et al. (2010) and Galletti and Zrnić (2011) calculated theoretical biases of $Z_{DR}$ and $\rho_{hv}$ estimates for a center-fed parabolic reflector antenna when either the SHV or the AHV modes of polarimetric data collection are used. Zrnić et al. (2010) introduce the SHV notation that defines copolar H and V waves of equal amplitude transmitted along the beam axis. Here we apply the notation STSR to designate that the H and V

ports of the array antenna are simultaneously excited with equal voltages (for the parabolic antenna SHV and AHV are synonymous with STSR and ATSR).

A Gaussian function was used by Zrnić et al. (2010) to model the copolar and cross-polar main lobes for the radiation patterns of parabolic reflector antennas. Although the main lobe is reasonably modeled by the Gaussian function, sidelobes are not. Furthermore, unlike the assumptions made by Zrnić et al. (2010), the copolar radiation pattern functions $F_{hh}$ and $F_{vv}$ for PPARS are not necessarily equal and real Gaussian functions, but are complex variables that are functions of $\theta, \varphi$. Moreover, for the reflector antenna, we use realistic radiation patterns to calculate the biases of $Z_{DR}$ and $\rho_{hv}$. Nevertheless the approach of Zrnić et al. (2010) can be generalized to compute biases for PPARs and parabolic reflector antennas having realistic radiation patterns. For the mechanically steered parabolic reflector there are no variations with direction. But for PPARs, the biases are a function of the beam scanning angle.

General formulas for the biases are derived in terms of radiation matrix elements given any kind of radar array element and any kind of antennas including PPPAR, CPPAR, and WSR-88D.

*2.6.1 the STSR mode*

To simplify calculations without sacrificing the objectives of this paper, $Z_{DR}$, $\rho_{hv}$ and $\varphi_{DP}$ biases are calculated under following conditions: 1) the intrinsic $Z_{DR}$ is produced by oblate hydrometeors having zero canting angles projected onto a plane

perpendicular to the beam axis; thus the off-diagonal terms of the backscattering matrix $\ddot{\mathbf{S}}$ are zero, 2) differential attenuation due to precipitation along the path of propagation can be neglected at 10-cm wavelengths, but differential phase shift $\Phi_{dp}$ cannot be neglected (Zrnić et al. 2010), and 3) reflectivity is spatially uniform. Thus as elevation angle is increased the axis of the oblate drops are assumed to increase so the drop's oblateness remains fixed. Although this latter condition is not expected in practice, it simplifies the solution without losing the principle aim of the work. We only need to assume reflectivity is uniform within the beam, a commonly accepted assumption. To simplify notation, the phase shifts $\phi_{hh}$ and $\phi_{vv}$ incurred during H and V propagation are incorporated into the backscattering matrix $\ddot{\mathbf{S}}$ (e.g., $\phi_{hh}$ is combined with $\delta_{hh}$ the phase shift upon backscatter for the H wave).

For the STSR mode, the matrix equation for the incremental voltages received in the H and V channels due to backscatter from a hydrometeor are given by Zrnić et al. (2010):

$$\begin{bmatrix} \delta V_{\mathbf{rh}} \\ \delta V_{\mathbf{rv}} \end{bmatrix} \equiv \mathbf{V_r} = \ddot{\mathbf{F}}^{\mathrm{T}} \ddot{\mathbf{S}} \ddot{\mathbf{F}} \vec{\mathbf{V}}_{\mathbf{t}} = \begin{bmatrix} F_{\mathbf{hh}} & F_{\mathbf{vh}} \\ F_{\mathbf{hv}} & F_{\mathbf{vv}} \end{bmatrix} \begin{bmatrix} s'_{\mathbf{hh}} & 0 \\ 0 & s_{\mathbf{vv}} \end{bmatrix} \begin{bmatrix} F_{\mathbf{hh}} & F_{\mathbf{hv}} \\ F_{\mathbf{vh}} & F_{\mathbf{vv}} \end{bmatrix} \begin{bmatrix} V_{\mathbf{th}} \\ V_{\mathbf{tv}} \end{bmatrix}, \qquad (2\text{-}17)$$

where $\ddot{\mathbf{F}}$ is the antenna's electric field radiation pattern matrix (or relative gain matrix) defined by Zrnić et al. (2010). $F_{\mathbf{hv}}$ is proportional to the cross-polar H radiated electric field ($E_\phi$) if the V port is energized and vice versa for $F_{\mathbf{vh}}$. $F_{\mathbf{ij}}(\theta,\phi) = \sqrt{g_{\mathbf{ij}}}\, f_{\mathbf{ij}}(\theta,\phi)$ where $f_{\mathbf{ij}}(\theta,\phi) = \left| f_{\mathbf{ij}}(\theta,\phi) \right| \exp\left[ j\gamma_{ij}(\theta,\phi) \right]$, and $\gamma_{ij}$ are the phases of the copolar and cross-polar fields- not necessarily the phase difference between the copolar and cross-

polar fields as can be assumed for the ideal reflector antenna. $\ddot{\mathbf{S}}$ is the backscattering matrix, but to account for differential propagation phase shift $\phi_{\mathrm{DP}}$ to and from the scatter $s'_{\mathrm{hh}} = s_{\mathrm{hh}} e^{j\phi_{DP}}$. $V_{\mathrm{th}}$ and $V_{\mathrm{tv}}$ are voltages applied simultaneously to the H and V antenna ports (for the array it is assumed that all element H and V voltages with weights specified by (2-1) to (2-3) are connected to a single H and V antenna port).

Zrnić et al. (2010) assumed a phase difference $\beta$ between the applied H and V voltages and assumed transmission lines from the antenna port to the element to be of equal length. Worst case $Z_{\mathrm{DR}}$ bias has been shown to occur for coaxial copolar and cross-polar beams if $\beta = 90^{\mathrm{o}}$ and if the phase difference between the copolar and cross-polar fields are in phase quadrature. In this case, the coaxial cross-polar peak needs to be 50 or more dB below the copolar peak to ensure that the $Z_{\mathrm{DR}}$ bias is less than 0.1 dB anywhere along the beam. $\beta$ can be controlled, and if $\beta = 0^{\mathrm{o}}$ or $180^{\mathrm{o}}$ (i.e., transmitted polarization is linear at a slant of $45^{\mathrm{o}}$ or $135^{\mathrm{o}}$), the acceptable cross-polar peak can be increased to 45 dB below the copolar peak, a relatively small 5 dB improvement. To simplify and to focus on the more significant bias sources associated with PPARs, we assume $\beta = 0^{\mathrm{o}}$ and $V_{\mathbf{th}} = V_{\mathbf{tv}} = 1$. Constants of proportionality are to make Eqn. (2-17) dimensionally correct, and the arguments of $F_{\mathrm{ij}}$ and $s_{\mathrm{ij}}$, are omitted to shorten the notation.

Eqn. (2-17) is applied to a single hydrometeor. But of interest is the spatial distribution of scatterers weighted by radiation pattern matrix elements. Under the

condition that the echoes from the neighboring area are uncorrelated, the expected powers received in the H and V channels are (Zrnić et al. 2010)

$$P_{\mathbf{h}} \sim \int_{\Omega} \left\langle \left| \delta V_{\mathbf{rh}} \right|^2 \right\rangle d\Omega , \tag{2-18}$$

$$P_{\mathbf{v}} \sim \int_{\Omega} \left\langle \left| \delta V_{\mathbf{rv}} \right|^2 \right\rangle d\Omega , \tag{2-19}$$

The bias of $Z_{DR}$ in dB is computed by subtracting the true value of $Z_{DR}$ from the estimated one. Thus $bias(Z_{DR})$ is given by

$$bias(Z_{\mathbf{DR}}) = 10 \cdot \log(P_{\mathbf{h}} / P_{\mathbf{v}}) - Z_{\mathbf{DR}}^{true} = 10 \cdot \log(B_1 / B_2) - Z_{\mathbf{DR}}^{true} , \tag{2-20}$$

where,

$$\begin{aligned} B_1 &= \frac{\int_{\Omega} \left\langle \left| \delta V_{\mathbf{rh}} \right|^2 \right\rangle d\Omega}{\left\langle \left| s_{\mathbf{vv}} \right|^2 \right\rangle} \\ &= Z_{\mathbf{dr}} \int_{\Omega} \left\{ \begin{array}{l} \left| F_{\mathbf{hh}} \right|^4 + \left| F_{\mathbf{hh}} \right|^2 \left| F_{\mathbf{hv}} \right|^2 + 2 \left| F_{\mathbf{hh}} \right|^2 \mathrm{Re}(F_{\mathbf{hh}}^* F_{\mathbf{hv}}) + \\ Z_{\mathbf{dr}}^{-1} \left[ \left| F_{\mathbf{vh}} \right|^2 \left| F_{\mathbf{vv}} \right|^2 + \left| F_{\mathbf{vh}} \right|^4 + 2 \left| F_{\mathbf{vh}} \right|^2 \mathrm{Re}(F_{\mathbf{vh}}^* F_{\mathbf{vv}}) \right] \\ +2 \left| \rho_{\mathbf{hv}}(0) \right| Z_{\mathbf{dr}}^{-0.5} \mathrm{Re} \left[ e^{-j\phi_{\mathbf{dp}}} \left( \begin{array}{l} F_{\mathbf{hh}}^{*\,2} F_{\mathbf{vh}}^{\;2} + F_{\mathbf{hh}}^* F_{\mathbf{hv}}^* F_{\mathbf{vh}}^{\;2} + \\ F_{\mathbf{hh}}^{*\,2} F_{\mathbf{vh}} F_{\mathbf{vv}} + F_{\mathbf{hh}}^* F_{\mathbf{hv}}^* F_{\mathbf{vv}} F_{\mathbf{vh}} \end{array} \right) \right] \end{array} \right\} d\Omega \end{aligned} \tag{2-21}$$

$$B_2 = \frac{\int_{\Omega} \left\langle \left| \delta V_{\mathbf{rv}} \right|^2 \right\rangle d\Omega}{\left\langle \left| s_{\mathbf{vv}} \right|^2 \right\rangle}$$

$$= \int_{\Omega} \left\{ \begin{array}{l} \left| F_{\mathbf{vv}} \right|^4 + \left| F_{\mathbf{vv}} \right|^2 \left| F_{\mathbf{vh}} \right|^2 + 2 \left| F_{\mathbf{vv}} \right|^2 \mathrm{Re}(F_{\mathbf{vv}}^* F_{\mathbf{vh}}) + \\ Z_{\mathbf{dr}} \left[ \left| F_{\mathbf{hh}} \right|^2 \left| F_{\mathbf{hv}} \right|^2 + \left| F_{\mathbf{hv}} \right|^4 + 2 \left| F_{\mathbf{hv}} \right|^2 \mathrm{Re}(F_{\mathbf{hv}}^* F_{\mathbf{hh}}) \right] \\ +2 \left| \rho_{\mathbf{hv}}(0) \right| Z_{\mathbf{dr}}{}^{0.5} \mathrm{Re} \left[ e^{-j\phi_{\mathbf{dp}}} \left( \begin{array}{l} F_{\mathbf{hv}}^{*\,2} F_{\mathbf{vv}}^2 + F_{\mathbf{hv}}^* F_{\mathbf{hh}}^* F_{\mathbf{vv}}^2 + \\ F_{\mathbf{hv}}^{*\,2} F_{\mathbf{vv}} F_{\mathbf{vh}} + F_{\mathbf{hh}}^* F_{\mathbf{hv}}^* F_{\mathbf{vv}} F_{\mathbf{vh}} \end{array} \right) \right] \end{array} \right\} d\Omega \tag{2-22}$$

Eqs.(2-21) and (2-22) are obtained by substituting (2-17) into (2-18) and (2-19). Lower case "dr" on Z indicates the ratio of H and V received powers, whereas the upper case "DR" subscript denotes $Z_{DR}$ in logarithmic units.

The bias of copolar correlation coefficient magnitude $|\rho_{hv}|$ and differential phase $\phi_{\mathbf{dp}}$ are given by

$$bias(|\rho_{\mathbf{hv}}|) = \frac{\left| \left\langle \delta V_{\mathbf{rh}}^* \delta V_{\mathbf{rv}} \right\rangle \right|}{\sqrt{\left\langle \left| \delta V_{\mathbf{rh}} \right|^2 \right\rangle \left\langle \left| \delta V_{\mathbf{rv}} \right|^2 \right\rangle}} - \left| \rho_{\mathbf{hv}}^{true} \right| \tag{2-23}$$

$$bias(\phi_{\mathbf{dp}}) = angle \left( \frac{\left\langle \delta V_{\mathbf{rh}}^* \delta V_{\mathbf{rv}} \right\rangle}{\sqrt{\left\langle \left| \delta V_{\mathbf{rh}} \right|^2 \right\rangle \left\langle \left| \delta V_{\mathbf{rv}} \right|^2 \right\rangle}} \right) - \phi_{\mathbf{dp}}^{true} \tag{2-24}$$

The bias of $|\rho_{hv}|$ and differential phase $\phi_{\mathbf{dp}}$ can be rewritten as

$$bias(|\rho_{\mathbf{hv}}|) = \frac{|B_3|}{\sqrt{B_1 B_2}} - \left| \rho_{\mathbf{hv}}^{true} \right| \tag{2-25}$$

$$bias(\phi_{\mathbf{dp}}) = angle\left(\frac{B_3}{\sqrt{B_1 B_2}}\right) - \phi_{\mathbf{dp}}^{true} \tag{2-26}$$

where $B_3$ is

$$\begin{aligned} B_3 &= \frac{\int_{\Omega} \left\langle \delta V_{\mathbf{rh}}^{*} \delta V_{\mathbf{rv}} \right\rangle d\Omega}{\left\langle \left| s_{\mathbf{vv}} \right|^2 \right\rangle} \\ &= \int_{\Omega} \begin{bmatrix} Z_{\mathbf{dr}} \left( \left| F_{\mathbf{hh}} \right|^2 F_{\mathbf{hh}}^{*} F_{\mathbf{hv}} + F_{\mathbf{hh}}^{*2} F_{\mathbf{hv}}^{\ 2} + \left| F_{\mathbf{hh}} \right|^2 \left| F_{\mathbf{hv}} \right|^2 + F_{\mathbf{hh}}^{*} F_{\mathbf{hv}} \left| F_{\mathbf{hv}} \right|^2 \right) \\ + \left| F_{\mathbf{vv}} \right|^2 F_{\mathbf{vv}} F_{\mathbf{vh}}^{*} + F_{\mathbf{vv}}^{\ 2} F_{\mathbf{vh}}^{*2} + \left| F_{\mathbf{vv}} \right|^2 \left| F_{\mathbf{vh}} \right|^2 \\ + \left| \rho_{\mathbf{hv}}(0) \right| e^{-j\phi_{dp}} Z_{\mathbf{dr}}^{\ 0.5} \left( F_{\mathbf{hh}}^{*2} F_{\mathbf{vv}}^{\ 2} + F_{\mathbf{hh}}^{*2} F_{\mathbf{vv}} F_{\mathbf{vh}} + F_{\mathbf{hh}}^{*} F_{\mathbf{vv}}^{\ 2} F_{\mathbf{hv}}^{*} \right) \\ + \left| \rho_{\mathbf{hv}}(0) \right| e^{j\phi_{dp}} Z_{\mathbf{dr}}^{\ 0.5} \left( F_{\mathbf{vh}}^{*2} F_{\mathbf{hv}}^{\ 2} + F_{\mathbf{vh}}^{*2} F_{\mathbf{hv}} F_{\mathbf{hh}} + F_{\mathbf{vh}}^{*} F_{\mathbf{vv}}^{*} F_{\mathbf{hv}}^{\ 2} \right) \\ + 2 \left| \rho_{\mathbf{hv}}(0) \right| Z_{\mathbf{dr}}^{\ 0.5} \mathrm{Re}\left( e^{-j\phi_{\mathbf{dp}}} F_{\mathbf{hh}}^{*} F_{\mathbf{hv}}^{*} F_{\mathbf{vv}} F_{\mathbf{vh}} \right) \end{bmatrix} d\Omega \end{aligned} \tag{2-27}$$

The sample results can be found in Chapter 3 section "3.3 Comparison of boresight contribution and integrations" and in Chapter 4 section "4.1 Bias of CPPAR" and section "4.2 Partial bias reduction of PPAR: adjusting antenna port voltages".

*2.6.2 the ATSR mode*

For the ATSR mode, we alternately set $V_{\mathrm{th}}$ to 1 and 0 and vice versa for $V_{\mathrm{tv}}$. The copolar H and cross polar echo voltages deduced from (2-17) are

$$\delta V_{\mathbf{rh}} = F_{\mathbf{hh}}^2 s_{\mathbf{hh}} + F_{\mathbf{vh}}^2 s_{\mathbf{vv}} \text{ , copolar} \tag{2-28}$$

$$\delta V_{\mathbf{rv}} = F_{\mathbf{hh}} F_{\mathbf{hv}} s_{\mathbf{hh}} + F_{\mathbf{vv}} F_{\mathbf{vh}} s_{\mathbf{vv}} \text{ cross-polar} \tag{2-29}$$

if $V_{\mathrm{th}} = 0$ and $V_{\mathrm{tv}} = 1$, and

$$\delta V_{\mathbf{rv}} = F_{\mathbf{vv}}^2 s_{\mathbf{vv}} + F_{\mathbf{hv}}^2 s_{\mathbf{hh}} \text{ , copolar} \tag{2-30}$$

$$\delta V_{\mathbf{rh}} = F_{\mathbf{hh}} F_{\mathbf{hv}} s_{\mathbf{hh}} + F_{\mathbf{vh}} F_{\mathbf{vv}} s_{\mathbf{vv}} \text{ cross-polar} \tag{2-31}$$

The strongest terms are the first terms in the copolar receiving channel and should dominate the second order cross-polar terms (in general $F_{hv} \neq F_{vh}$, (Zrnić et al. 2010)). The cross-polar terms given by (2-29) and (2-31) are first order in $F_{hv}$ and $F_{vh}$ and these terms set limits on how well the radar can measure $s_{hv}$, which is typically small for rain.

We can bring Eqns. (2-28) to (2-31) into Eqns. (2-18) and (2-19) to obtain the powers.

Then, the bias of $Z_{DR}$ in dB is computed from

$$bias(Z_{\mathbf{DR}}) \approx 10 \cdot \log(P_{\mathbf{h}} / P_{\mathbf{v}}) - Z_{\mathbf{DR}}^{true} = 10 \cdot \log(B_4 / B_5) - Z_{\mathbf{DR}}^{true}, \quad (2\text{-}32)$$

Where,

$$B_4 = \frac{\int_{\Omega} \left\langle \left| \delta V_{\mathbf{h}} \right|^2 \right\rangle d\Omega}{\left\langle \left| s_{\mathbf{vv}} \right|^2 \right\rangle} = \int_{\Omega} \left[ Z_{\mathbf{dr}} \left| F_{\mathbf{hh}} \right|^4 + \left| F_{\mathbf{vh}} \right|^4 + 2\rho_{\mathbf{hv}} Z_{\mathbf{dr}}^{0.5} \mathrm{Re}(e^{j\phi_{\mathbf{dp}}} F_{\mathbf{hh}}^{*2} F_{\mathbf{vh}}^{2}) \right] d\Omega \quad (2\text{-}33)$$

$$B_5 = \frac{\int_{\Omega} \left\langle \left| \delta V_{\mathbf{v}} \right|^2 \right\rangle d\Omega}{\left\langle \left| s_{\mathbf{vv}} \right|^2 \right\rangle} = \int_{\Omega} \left[ \left| F_{\mathbf{vv}} \right|^4 + Z_{\mathbf{dr}} \left| F_{\mathbf{hv}} \right|^4 + 2\rho_{\mathbf{hv}} Z_{\mathbf{dr}}^{0.5} \mathrm{Re}(e^{j\phi_{\mathbf{dp}}} F_{\mathbf{vv}}^{2} F_{\mathbf{hv}}^{*2}) \right] d\Omega \quad (2\text{-}34)$$

The bias of $|\rho_{hv}|$ and differential phase $\phi_{\mathbf{dp}}$ are given by

$$bias(|\rho_{\mathbf{hv}}|) = \frac{\left| \left\langle \delta V_{\mathbf{h}}^{*} \delta V_{\mathbf{v}} \right\rangle \right|}{\sqrt{\left\langle \left| \delta V_{\mathbf{h}} \right|^2 \right\rangle \left\langle \left| \delta V_{\mathbf{v}} \right|^2 \right\rangle}} - \left| \rho_{\mathbf{hv}}^{true} \right|, \quad (2\text{-}35)$$

$$bias(\phi_{\mathbf{dp}}) = angle\left( \frac{\left\langle \delta V_{\mathbf{rh}}^{*} \delta V_{\mathbf{rv}} \right\rangle}{\sqrt{\left\langle \left| \delta V_{\mathbf{rh}} \right|^2 \right\rangle \left\langle \left| \delta V_{\mathbf{rv}} \right|^2 \right\rangle}} \right) - \phi_{\mathbf{dp}}^{true} \quad (2\text{-}36)$$

The bias of $|\rho_{hv}|$ and differential phase $\phi_{dp}$ can be rewritten as

$$bias(|\rho_{hv}|) = \frac{|B_6|}{\sqrt{B_4 B_5}} - |\rho_{hv}^{true}| \tag{2-37}$$

$$bias(\phi_{dp}) = angle\left(\frac{B_6}{\sqrt{B_4 B_5}}\right) - \phi_{dp}^{true} \tag{2-38}$$

where $B_4$ and $B_5$ can be found in (2-33) and (2-34) respectively and $B_6$ is

$$B_6 = \frac{\int_{\Omega} \langle \delta V_h^* \delta V_v \rangle d\Omega}{\langle |s_{vv}|^2 \rangle} = \int_{\Omega} \begin{bmatrix} Z_{dr} F_{hh}^{*2} F_{hv}^{2} + F_{vv}^{2} F_{vh}^{*2} \\ +\rho_{hv} e^{j\phi_{dp}} Z_{dr}^{0.5} F_{hh}^{*2} F_{vv}^{2} \\ +\rho_{hv} e^{-j\phi_{dp}} Z_{dr}^{0.5} F_{hv}^{2} F_{vh}^{*2} \end{bmatrix} d\Omega \tag{2-39}$$

The general formulas given in this section can be used to calculate the biases for any kinds of antennas in the following chapters.

The sample results can be found in Chapter 3 section "3.3 Comparison of boresight contribution and integrations" and in Chapter 4 section "4.1 Bias of CPPAR" and section "4.2 Partial bias reduction of PPAR: adjusting antenna port voltages".

# Chapter 3 PPPAR Biases and Correction

Polarimetric weather radar provides multi-parameter measurements that reveal detailed precipitation microphysics, which has matured to the stage that the national network of WSR-88D radars is being upgraded with dual-polarization. Recently, phased array radar has received great attention, as it allows for fast data update to quickly track storm evolution. It is desirable to combine polarimetry and phased array technology into one system: polarimetric phased array radar (PPAR). The most common configuration for a phased array is planar arrangement. The planar PPAR (PPPAR), however, has significant deficiencies, including polarization coupling, increase in beam width, and loss of sensitivity when its beam scans away from the broadside. Due to these reasons, biases of polarimetric parameters occur as the beam scans. Some methods have been suggested to solve the coupling deficiency of PPPAR. A method considers a projection matrix or correction matrix to correct the polarization coupling (Zhang et al. 2009). If the projection matrix or correction matrix is known, the bias of dual polarization radar parameters can be corrected. This chapter is to discuss these biases and the corrections of these biases.

## 3.1 Projection and scattering matrices

The projection and scattering matrices for the PPAR are discussed. The projection matrix is first defined by Zhang et al. (2009) to represent the relation between the broadside transmitted wave $\vec{E}_{\mathrm{t}}(r,0,0)$ and the wave $\vec{E}_{\mathrm{i}}(r,\theta,\phi)$ locally incident in the direction $\theta,\phi$. Whereas the cross-polar radiation is independent of beam

axis direction for a mechanically steered beam, the cross-polar radiation intensity of a beam electronically steered by a PPAR does depends on beam axis direction. The projection matrices for both aperture and patches are given in this chapter.

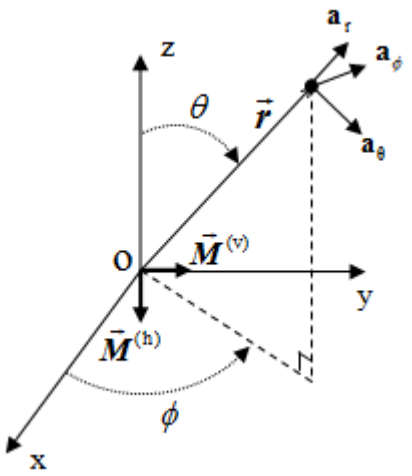


**Figure 3-1** The coordinate system for electric fields from a pair of radiating elements.
$\vec{M}^{(h)}$ is the magnetic current density of a horizontally polarized radiating element.
$\vec{M}^{(v)}$ is the magnetic current density of a vertically polarized radiating element.

*3.1.1 Projection matrix*

The projection matrix **P** is defined by $\vec{E}_i = \mathbf{P}\vec{E}_t$ and its entries represent projections of radiated fields $E_t$ along the broadside direction (x) onto the local H, V directions at $\vec{r}$ (Figure 3-1). The local horizontal is defined by $\mathbf{a}_\phi$; the local vertical is defined by $-\mathbf{a}_\theta$ (Figure 3-1). The broadside transmitted waves generated by the horizontally and vertically polarized elements are projected onto the local unit vectors $\mathbf{a}_\phi$ and $-\mathbf{a}_\theta$ to obtain the incident wave:

$$\vec{E}_{\mathrm{i}} = \begin{bmatrix} E_{\mathrm{i}\phi} \\ -E_{\mathrm{i}\theta} \end{bmatrix} = \mathbf{P} \begin{bmatrix} E_{\mathrm{th}} \\ E_{\mathrm{tv}} \end{bmatrix} = \mathbf{P}\vec{E}_{\mathrm{t}} \tag{3-1}$$

where the projection matrix $\mathbf{P}$ is:

$$\mathbf{P} = \begin{bmatrix} p_{11} & p_{12} \\ p_{21} & p_{22} \end{bmatrix} = \begin{bmatrix} E_{\phi}^{(\mathrm{h})} & E_{\phi}^{(\mathrm{v})} \\ -E_{\theta}^{(\mathrm{h})} & -E_{\theta}^{(\mathrm{v})} \end{bmatrix} \tag{3-2}$$

where the superscripts define H and V antenna ports. The H antenna port primiarly transmits horizontally polarized fields and V antenna port primiarly transmits vertically polarized fields, and all the electric fields on the right side of (3-2) are normalized by their respective broadside electric fields (e.g., $E_{\phi}^{(h)}(\theta,\phi)$ or $E_{\theta}^{(h)}(\theta,\phi)$ is normalized by $E^{(h)}\left(\frac{\pi}{2},0\right)$). Substituting the appropriate electric fields from Eqn. (2-4) to (2-15) into (3-2), the projection matrix for aperture or patch can be obtained. The projection matrix for the aperture is:

$$\mathbf{P} = \begin{bmatrix} \sin\theta \cdot f^{(\mathrm{h})}(\theta,\phi) & \cos\theta\sin\phi \cdot f^{(\mathrm{v})}(\theta,\phi) \\ 0 & \cos\phi \cdot f^{(\mathrm{v})}(\theta,\phi) \end{bmatrix} \tag{3-3}$$

The $f^{(\mathrm{h})}(\theta,\phi)$ and $f^{(\mathrm{v})}(\theta,\phi)$ given by (2-6) and (2-9) in the above matrix are due to the finite size of the aperture compared to the infinite small size of dipole in one direction. The terms other than $f^{(\mathrm{h})}(\theta,\phi)$ and $f^{(\mathrm{v})}(\theta,\phi)$ have similar forms as the P-matrix of Hertzian dipoles (Zhang et al. 2009). The slightly different form is due to the complementary characteristics (Kraus et al. 2002, chapter 9-2) of the dipole and the rectangular aperture in an infinite ground plane; whereas a vertically oriented electric dipole generates fields isotropic in the x-y plane (i.e., the H-plane of the dipole), a vertically oriented narrow slot, having horizontally polarized fields, is well represented by a vertically oriented magnetic dipole that generates fields isotropic in the E-plane,

also the x-y plane. That is, the H-plane of the vertically oriented electric dipole and the E-plane of the vertically oriented narrow slot are both the horizontal plane at z= 0.

Similarly, the projection matrix for the patch is:

$$\mathbf{P} = \begin{bmatrix} \sin\theta \cdot g^{(\mathrm{h})}(\theta,\phi) & \cos\theta \sin\phi \cdot g^{(\mathrm{v})}(\theta,\phi) \\ 0 & \cos\phi \cdot g^{(\mathrm{v})}(\theta,\phi) \end{bmatrix} \tag{3-4}$$

where the sine function in $g^{(\mathrm{h})}$ and $g^{(\mathrm{v})}$ given by (2-12) and (2-15) is due to the finite size of the antenna and the cosine function in them is the array factor for the two radiating slots on opposite sides of the patch. By comparing the P-matrix of aperture and patch elements with the P-matrix of the crossed dipole element in Zhang et al. (2009) and assuming that $f$ and $g$ in (3-3) and (3-4) are equal to one, the P-matrices have the following relationships:

$\left(\mathbf{P}^{T}_{\mathrm{dipole}}\right)^{-1} \propto \mathbf{P}_{\mathrm{aperture}}$, $\left(\mathbf{P}^{T}_{\mathrm{dipole}}\right)^{-1} \propto \mathbf{P}_{\mathrm{patch}}$, $\left(\mathbf{P}^{T}_{\mathrm{aperture}}\right)^{-1} \propto \mathbf{P}_{\mathrm{dipole}}$, and $\left(\mathbf{P}^{T}_{\mathrm{patch}}\right)^{-1} \propto \mathbf{P}_{\mathrm{dipole}}$.

*3.1.2 Scattering matrix*

The back scattering electric field $\vec{E}_s$ can be expressed as (Doviak and Zrnić 2006, section 8.5.2.1)

$$\vec{E}_{\mathrm{s}} = \begin{bmatrix} E_{\mathrm{sh}} \\ E_{\mathrm{sv}} \end{bmatrix} = \mathbf{S}^{(b)} \vec{E}_{\mathrm{i}} \times \frac{\exp(-jkr)}{r} \tag{3-5}$$

where $\mathbf{S}^{(b)} = \begin{bmatrix} s^{(b)}_{\mathrm{hh}} & s^{(b)}_{\mathrm{hv}} \\ s^{(b)}_{\mathrm{vh}} & s^{(b)}_{\mathrm{vv}} \end{bmatrix}$, is defined as the scattering matrix of a hydrometeor which relates the backscattered electric field to the incident electric field. The electric fields at

the receiving array element (assumed to be the same as the transmitting array element) can be expressed as (Zhang et al. 2009):

$$\vec{E}_{\mathrm{r}} = \begin{bmatrix} E_{\mathrm{rh}} \\ E_{\mathrm{rv}} \end{bmatrix} = \mathbf{P}^T \begin{bmatrix} E_{\mathrm{s}\phi} \\ -E_{\mathrm{s}\theta} \end{bmatrix} = \mathbf{P}^T \vec{E}_{\mathrm{s}} \tag{3-6}$$

$\vec{E}_{\mathrm{r}}$ is the electrical field at the receiving antenna port. By combing(3-1), (3-5) and(3-6), $\vec{E}_{\mathrm{r}}$ can be expressed as:

$$\vec{E}_{\mathrm{r}} = \mathbf{P}^T \mathbf{S}^{(b)} \mathbf{P} \vec{E}_{\mathrm{t}} \times \frac{\exp(-jkr)}{r} \tag{3-7}$$

where $\mathbf{S}^{(p)} = \mathbf{P}^T \mathbf{S}^{(b)} \mathbf{P}$ is the scattering matrix for the PPAR. If the propagation effect is included and the transmission matrix is added, (3-7) is extended to (Zhang et al. 2009):

$$\vec{E}_{\mathrm{r}} = \mathbf{P}^T \mathbf{S}' \mathbf{P} \vec{E}_{\mathrm{t}} \times \frac{\exp(-jkr)}{r} \tag{3-8}$$

where $\mathbf{S}' \equiv \mathbf{T}\mathbf{S}^{(b)}\mathbf{T}$ and $\mathbf{T}$ is the transmission matrix (Zhang et al. 2009). Then, the backscattering matrix for the PPAR is

$$\begin{aligned} \mathbf{S}^{(p)} &\equiv \mathbf{P}^T \mathbf{S}' \mathbf{P} \\ &= \begin{bmatrix} p_{11}^2 s'_{\mathrm{hh}} + p_{21}^2 s'_{\mathrm{vv}} + p_{11}p_{21}(s'_{\mathrm{vh}} + s'_{\mathrm{hv}}) & p_{11}p_{12}s'_{\mathrm{hh}} + p_{21}p_{22}s'_{\mathrm{vv}} + p_{11}p_{22}s'_{\mathrm{hv}} + p_{12}p_{21}s'_{\mathrm{vh}} \\ p_{11}p_{12}s'_{\mathrm{hh}} + p_{21}p_{22}s'_{\mathrm{vv}} + p_{11}p_{22}s'_{\mathrm{vh}} + p_{12}p_{21}s'_{\mathrm{hv}} & p_{12}^2 s'_{\mathrm{hh}} + p_{22}^2 s'_{\mathrm{vv}} + p_{12}p_{22}(s'_{\mathrm{vh}} + s'_{\mathrm{hv}}) \end{bmatrix} \end{aligned} \tag{3-9}$$

To simplify (3-9) it is noted that $p_{21}$ is zero for ideal aperture and patch antennas according to(3-2), (3-3) and(3-4). Thus (3-9) reduces to:

$$\begin{aligned} \mathbf{S}^{(p)} &\equiv \mathbf{P}^T \mathbf{S}' \mathbf{P} \\ &= \begin{bmatrix} p_{11}^2 s'_{\mathrm{hh}} & p_{11}p_{12}s'_{\mathrm{hh}} + p_{11}p_{22}s'_{\mathrm{hv}} \\ p_{11}p_{12}s'_{\mathrm{hh}} + p_{11}p_{22}s'_{\mathrm{vh}} & p_{12}^2 s'_{\mathrm{hh}} + p_{22}^2 s'_{\mathrm{vv}} + p_{12}p_{22}(s'_{\mathrm{vh}} + s'_{\mathrm{hv}}) \end{bmatrix} \end{aligned} \tag{3-10}$$

The off-diagonal terms in (3-10) are even smaller because, for most meteorological observations of interest, hydrometeors have a vertical axes of symmetry and therefore $s'_{hv} = s'_{vh} \approx 0$. Thus (3-10) is further simplified to:

$$\mathbf{S}^{(p)} \equiv \mathbf{P}^T \mathbf{S}' \mathbf{P} = \begin{bmatrix} p_{11}^2 s'_{hh} & p_{11} p_{12} s'_{hh} \\ p_{11} p_{12} s'_{hh} & p_{12}^2 s'_{hh} + p_{22}^2 s'_{vv} \end{bmatrix} \tag{3-11}$$

The superscript 'prime' here means the scattering matrix measured by radar using a mechanically steered beam with propagation effect included (Zhang et al. 2009). In order to recover $\mathbf{S}'$ for PPAR,

$$\mathbf{S}' \equiv \mathbf{C}^T \mathbf{S}^{(p)} \mathbf{C} \tag{3-12}$$

where $\mathbf{C}$ is defined as correction matrix and $\mathbf{C} = \mathbf{P}^{-1}$.

There are two polarimetric transmitting/receiving modes in weather radar operation. One is ATSR (Alternate Transmit Simultaneous Receive) mode, wherein the H and V polarized waves are alternately transmitted but simultaneously received. And the other is STSR (Simultaneous Transmit and Simultaneous Receive) mode, wherein the H and V polarized waves are simultaneously transmitted and simultaneously received.

### 3.1.2.1 Scattering matrix for the ATSR mode

In ATSR mode, all the elements of scattering matrix $\mathbf{S}^{(p)}$ can be measured, and the correction for the ATSR mode of PPAR is given by solving (3-10) for $\mathbf{S}'$. For example, the backscattering coefficient $s'_{hh}$ can be obtained by dividing the top left

matrix element by $p_{11}^2$. Then, $s'_{hv}$ and $s'_{vh}$ can be calculated from the off-diagonal terms of (3-10). Finally, $s'_{vv}$ can be obtained because the other three elements of the scattering matrix are now known.

If the Doppler effect is considered (Zrnić et al. 2011), (3-9) need to be modified. The sample time between alternately transmitted H and V is equal to the PRT (i.e., Pulse Repetition Time). The phase shifts caused by scatterers' motion are different in the H and V due to the PRT time difference. In ATSR mode, we consider the two consecutive times with indices $2i$ and $2i+1$, where $i$ is an integer, multiplied by the pulse repetition time $T_s$. Even indices indicate that a horizontally polarized wave is transmitted whereas odd indices indicate that a vertically polarized wave is transmitted. Thus the backscattering matrix of PPAR, modified for the Doppler effect, is:

$$\mathbf{S}^{(p)} = \begin{bmatrix} s_{hh}^{(p)}(2i) & s_{hv}^{(p)}(2i+1) \\ s_{vh}^{(p)}(2i) & s_{vv}^{(p)}(2i+1) \end{bmatrix} = \begin{bmatrix} s_{hh}^{(p)}(2i) & e^{-j2k_0\hat{v}T_s} \cdot s_{hv}^{(p)}(2i) \\ s_{vh}^{(p)}(2i) & e^{-j2k_0\hat{v}T_s} \cdot s_{vv}^{(p)}(2i) \end{bmatrix} \tag{3-13}$$

where, $\hat{v}$ is the radial velocity, which can be estimated from the auto-correlation of either

$s_{hh}^{(p)}$ or $s_{vv}^{(p)}$. The elements in the (3-13) can be found in (3-9) and they are given by:

$$s_{hh}^{(p)}(2i) = p_{11}^2 s'_{hh}(2i) + p_{21}^2 s'_{vv}(2i) + p_{11}p_{21}(s'_{vh}(2i) + s'_{hv}(2i)) \tag{3-14}$$

$$s_{vh}^{(p)}(2i) = p_{11}p_{12}s'_{hh}(2i) + p_{21}p_{22}s'_{vv}(2i) + p_{11}p_{22}s'_{vh}(2i) + p_{12}p_{21}s'_{hv}(2i) \tag{3-15}$$

$$s_{hv}^{(p)}(2i+1) = p_{11}p_{12}s'_{hh}(2i+1) + p_{21}p_{22}s'_{vv}(2i+1) + p_{11}p_{22}s'_{hv}(2i+1) + p_{12}p_{21}s'_{vh}(2i+1) \tag{3-16}$$

$$s_{vv}^{(p)}(2i+1) = p_{12}^2 s'_{hh}(2i+1) + p_{22}^2 s'_{vv}(2i+1) + p_{12}p_{22}(s'_{vh}(2i+1) + s'_{hv}(2i+1)) \tag{3-17}$$

Because $p_{21} = 0$ for the ideal radiating elements being considered here, (3-14) to (3-17) are simplified to:

$$s_{\mathrm{hh}}^{(p)}(2i) = p_{11}^2 s'_{\mathrm{hh}}(2i) \tag{3-18}$$

$$s_{\mathrm{vh}}^{(p)}(2i) = p_{11}p_{12}s'_{\mathrm{hh}}(2i) + p_{11}p_{22}s'_{\mathrm{vh}}(2i) \tag{3-19}$$

$$s_{\mathrm{hv}}^{(p)}(2i+1) = p_{11}p_{12}s'_{\mathrm{hh}}(2i+1) + p_{11}p_{22}s'_{\mathrm{hv}}(2i+1) \tag{3-20}$$

$$s_{\mathrm{vv}}^{(p)}(2i+1) = p_{12}^2 s'_{\mathrm{hh}}(2i+1) + p_{22}^2 s'_{\mathrm{vv}}(2i+1) + p_{12}p_{22}(s'_{\mathrm{vh}}(2i+1) + s'_{\mathrm{hv}}(2i+1)) \tag{3-21}$$

Assuming the P matrix is known, $s'_{\mathrm{hh}}(2i)$ can be obtained from (3-18). Then we bring $s'_{\mathrm{hh}}(2i)$ into (3-19), allowing us to calculate $s'_{\mathrm{vh}}(2i)$. In(3-20), $s'_{\mathrm{hv}}(2i+1)$ can be obtained if the Doppler term $e^{j2k_0\hat{v}T_s}$ is known, (it can be estimated from either of the auto-correlations $< s_{\mathrm{hh}}^{(p)*}(2i) \cdot s_{\mathrm{hh}}^{(p)}(2i+2) >$ or $< s_{\mathrm{vv}}^{(p)*}(2i+1) \cdot s_{\mathrm{vv}}^{(p)}(2i+3) >$ ; brackets denote ensemble average), and $s'_{\mathrm{hh}}(2i)$ has already been calculated. Finally, $s'_{\mathrm{vv}}(2i+1)$ can be obtained by (3-21) if $s'_{\mathrm{hh}}(2i), s'_{\mathrm{vh}}(2i), s'_{\mathrm{hv}}(2i+1)$, and $e^{j2k_0\hat{v}T_s}$ are known.

### 3.1.2.2 Scattering matrix for the STSR mode

Another radar operation mode is the STSR. Doppler effects are not coupled to the polarimetric variables in the STSR mode. However the four elements of scattering matrix cannot all be obtained in the STSR mode. In order to precisely calculate the diagonal terms of the scattering matrix, the off-diagonal terms must be zero. Fortunately most precipitation media have $s'_{\mathrm{hv}} = s'_{\mathrm{vh}} \approx 0$ and the off-diagonal terms can typically be ignored. Because the broadside H, V transmitted fields can have amplitude and phase

differences, we assume $E_{\text{th}} = \gamma E_{\text{tv}} e^{j\psi}$, where $\gamma$ is the amplitude ratio of the broadside electric fields and $\psi$ is their relative phase. From (3-8) with an assumption of no cross-polar scattering, we have

$$\begin{aligned}\begin{bmatrix} E_{\text{rh}} \\ E_{\text{rv}} \end{bmatrix} &= \mathbf{P}^T \begin{bmatrix} s'_{\text{hh}} & 0 \\ 0 & s'_{\text{vv}} \end{bmatrix} \mathbf{P} \begin{bmatrix} E_{\text{th}} \\ E_{\text{tv}} \end{bmatrix} \frac{\exp(-jkr)}{r} \\ &= \begin{bmatrix} E_{\text{th}}(p_{11}^2 s'_{\text{hh}} + p_{21}^2 s'_{\text{vv}}) + E_{\text{tv}}(p_{11}p_{12}s'_{\text{hh}} + p_{21}p_{22}s'_{\text{vv}}) \\ E_{\text{th}}(p_{11}p_{12}s'_{\text{hh}} + p_{21}p_{22}s'_{\text{vv}}) + E_{\text{tv}}(p_{12}^2 s'_{\text{hh}} + p_{22}^2 s'_{\text{vv}}) \end{bmatrix} \frac{\exp(-jkr)}{r}\end{aligned} \tag{3-22}$$

For an ideal aperture and an ideal patch for which the radiation from the non-radiating slots are ignored, $p_{21} = 0$, and thus

$$\begin{bmatrix} E_{\text{rh}} \\ E_{\text{rv}} \end{bmatrix} = \begin{bmatrix} E_{\text{th}}(p_{11}^2 s'_{\text{hh}}) + E_{\text{tv}}(p_{11}p_{12}s'_{\text{hh}}) \\ E_{\text{th}}(p_{11}p_{12}s'_{\text{hh}}) + E_{\text{tv}}(p_{12}^2 s'_{\text{hh}} + p_{22}^2 s'_{\text{vv}}) \end{bmatrix} \frac{\exp(-jkr)}{r} \tag{3-23}$$

Equation (3-23) can be used to solve $s'_{\text{hh}}$ and $s'_{\text{vv}}$.

### 3.2 Biases of polarimetric variables

The biased polarimetric variables (i.e. due to the coupling of H and V radiation for beams steered away from the broadside direction) reflectivities, differential reflectivity, correlation coefficient, and LDR for both the ATSR and STSR modes are presented next. Throughout this section, a narrow beam radar and homogeneous scatter distribution assumptions are made in the calculation of covariances (Doviak and Zrnić 2006, section 8.5.2.2).

#### *3.2.1 Reflectivity Factor*

The intrinsic reflectivity factors at horizontal and vertical polarizations are given by

$$Z_{\mathrm{h,v}} = \frac{4\lambda^4 N}{\pi^4 \left|K_{\mathrm{w}}\right|^2} \left\langle \left| s_{\mathrm{hh,vv}}^{(b)} \right|^2 \right\rangle \tag{3-24}$$

where

$$\left\langle \left| s_{\mathrm{hh,vv}}^{(b)} \right|^2 \right\rangle = \int p(D) \left| s_{\mathrm{hh,vv}}^{(b)}(D) \right|^2 dD \tag{3-25}$$

$N$ represents the number density of scatterers per unit volume. $p(D)$ represents the probability density function of the scatterers' diameters. Compared to drop size distribution $n(D)$ (Doviak and Zrnić 2006, section 4.4), $p(D)$ is normalized and its integral over all possible values of $D$ is one. $p(D)$ computed from $n(D)$ is given by

$$p(D) = \frac{n(D)}{\int_0^\infty n(D) dD} = \frac{n(D)}{N} \tag{3-26}$$

The horizontal and vertical reflectivity factors $Z'_{\mathrm{h,v}}$ measured by the radar using a mechanically steered beam are

$$Z'_{\mathrm{h,v}} = \frac{4\lambda^4 N}{\pi^4 \left|K_{\mathrm{w}}\right|^2} \left\langle \left| s'_{\mathrm{hh,vv}} \right|^2 \right\rangle \tag{3-27}$$

$Z'_{\mathrm{h,v}}$ are different from the intrinsic reflectivity factors $Z_{\mathrm{h,v}}$ by the propagation effect (Doviak and Zrnić 2006, sectioin 8.5.2.2; details can be found in Eqn. (23) in Zhang et al. 2009).

By the same definition as (3-24) and (3-27), the reflectivity factor for horizontally polarized waves from the array element for the PPAR is

$$
\begin{aligned}
Z_{\mathrm{h}}^{(p)} &= \frac{4\lambda^4 N}{\pi^4 \left|K_{\mathrm{w}}\right|^2} \left\langle \left| s_{\mathrm{hh}}^{(p)} \right|^2 \right\rangle \\
&= \frac{4\lambda^4 N}{\pi^4 \left|K_{\mathrm{w}}\right|^2} \left\langle \left| p_{11}^2 s'_{\mathrm{hh}} + p_{21}^2 s'_{\mathrm{vv}} \right|^2 \right\rangle \\
&= p_{11}^4 Z'_{\mathrm{h}} + p_{21}^4 Z'_{\mathrm{v}} + 2\sqrt{Z'_{\mathrm{h}} Z'_{\mathrm{v}}}\, \mathrm{Re}[\rho'_{\mathrm{hv}}] p_{11}^2 p_{21}^2
\end{aligned}
\tag{3-28}
$$

where $p_{11}$ and $p_{21}$ are elements of the $P$ matrix defined in (3-2). For an ideal element, $p_{21} = 0$, and thus

$$
Z_{\mathrm{h}}^{(p)} = p_{11}^4 Z'_{\mathrm{h}} \tag{3-29}
$$

The horizontal reflectivity factor for PPAR is simply $Z'_{\mathrm{h}}$ obtained with a mechanically steered beam scaled by $p_{11}^4$. But the reflectivity factor for vertically polarized waves is

$$
\begin{aligned}
Z_{\mathrm{v}}^{(p)} &= \frac{4\lambda^4 N}{\pi^4 \left|K_{\mathrm{w}}\right|^2} \left\langle \left| s_{\mathrm{vv}}^{(p)} \right|^2 \right\rangle, \\
&= \frac{4\lambda^4 N}{\pi^4 \left|K_{\mathrm{w}}\right|^2} \left\langle \left| p_{12}^2 s'_{\mathrm{hh}} + p_{22}^2 s'_{\mathrm{vv}} \right|^2 \right\rangle, \\
&= p_{12}^4 Z'_{\mathrm{h}} + p_{22}^4 Z'_{\mathrm{v}} + 2\sqrt{Z'_{\mathrm{h}} Z'_{\mathrm{v}}}\, \mathrm{Re}[\rho'_{\mathrm{hv}}] p_{12}^2 p_{22}^2,
\end{aligned}
\tag{3-30}
$$

where $p_{12}$ and $p_{22}$ are also elements of the $P$ matrix defined in (3-2). For aperture and patch elements, the $P$ matrices are from (3-3) and (3-4). If the same procedure is implemented on PPAR to obtain the reflectivities, it is seen that the measured reflectivities obtained with a PPAR are biased compared with the reflectivities measured with the mechanically steered radar. The bias depends on the projection matrix (i.e. the steering angle and the radiation pattern), the horizontal and vertical reflectivities, and the copolar correlation coefficient. From(3-29), it is seen that the bias of horizontal reflectivity depends on $p_{11}$, which are $\sin\theta \cdot f^{(\mathrm{h})}(\theta, \phi)$ and

$\sin(\theta)\cdot g^{(h)}(\theta,\phi)$ for aperture and patch elements respectively. As the beam points gradually off the broadside, the bias of reflectivity increases from zero. For example, if the beam points at $(\theta,\phi)$ = (75°, 30°), $Z_{\mathrm{h}}^{(p)} = 0.6489 Z'_{\mathrm{h}}$, which is a significant difference between the reflectivity factor measured by PPAR and the reflectivity factor measured with a mechanically steered dish antenna. From(3-30), it is seen that $Z_{\mathrm{v}}^{(p)}$ depends on $Z'_{\mathrm{h}}$, $Z'_{\mathrm{v}}$, $\rho'_{\mathrm{hv}}$, as well as on the projection matrix.

*3.2.2 Differential Reflectivity*

Differential reflectivity is the ratio of horizontal and vertical reflectivities, and it is a measure of the oblateness of the hydrometers. For the mechanically steered beam, the definition of differential reflectivity is (Doviak and Zrnić 2006, section 8.5)

$$Z'_{\mathrm{DR}} = 10\log\left(\frac{\left\langle\left|s'_{\mathrm{hh}}\right|^2\right\rangle}{\left\langle\left|s'_{\mathrm{vv}}\right|^2\right\rangle}\right) \tag{3-31}$$

If the same measurement procedure is implemented on a PPAR as for the mechanically steered beam, the differential reflectivity measured with a PPAR for the ATSR mode would be

$$\begin{aligned} Z_{\mathrm{DR}}^{(p)}(\mathrm{ATSR}) &= 10\log\left(\frac{\left\langle\left|s_{\mathrm{hh}}^{(p)}\right|^2\right\rangle}{\left\langle\left|s_{\mathrm{vv}}^{(p)}\right|^2\right\rangle}\right) \\ &= 10\log\left(\frac{p_{11}^4 Z'_{\mathrm{h}} + p_{21}^4 Z'_{\mathrm{v}} + 2\sqrt{Z'_{\mathrm{h}} Z'_{\mathrm{v}}}\,\mathrm{Re}[\rho'_{\mathrm{hv}}]p_{11}^2 p_{21}^2}{p_{12}^4 Z'_{\mathrm{h}} + p_{22}^4 Z'_{\mathrm{v}} + 2\sqrt{Z'_{h} Z'_{v}}\,\mathrm{Re}[\rho'_{\mathrm{hv}}]p_{12}^2 p_{22}^2}\right) \\ &= 10\log\left(\frac{p_{11}^4 Z'_{\mathrm{dr}} + p_{21}^4 + 2\sqrt{Z'_{\mathrm{dr}}}\,\mathrm{Re}[\rho'_{\mathrm{hv}}]p_{11}^2 p_{21}^2}{p_{12}^4 Z'_{\mathrm{dr}} + p_{22}^4 + 2\sqrt{Z'_{\mathrm{dr}}}\,\mathrm{Re}[\rho'_{\mathrm{hv}}]p_{12}^2 p_{22}^2}\right) \end{aligned} \tag{3-32}$$

Figure 3-2a, Figure 3-3a, and Figure 3-3b present the $Z_{DR}$ bias, for the ATSR mode, as a function of azimuth $\phi$ and several $\theta$ for aperture and patch elements. The parameters used for calculations are $Z'_{dr} = 1.0$ and $\rho_{hv} = 0.9$ in all cases. The $Z_{DR}$ bias for the aperture antenna is positive at $\pm 45°$ azimuth because the vertically polarized wave is weaker than the horizontally polarized wave, as shown in Figure 2-4. At 0° azimuth and $\theta < 90°$, the $Z_{DR}$ bias is negative because the horizontally polarized wave is weaker than the vertically polarized wave. This trend is opposite that seen for the dipole in Zhang et al. (2009) because of the complementary property of dipole and aperture antennas. Figure 3-3b shows that the dimension of the patch can largely change the $Z_{DR}$ bias, and a judicious selection patch size can make the $Z_{DR}$ bias almost zero for all azimuths if $\theta = 90° \pm 20°$. For instance, because a patch having L = $0.38\lambda_o$ and $L_e$ = $0.40\lambda_o$ generates nearly equivalent radiation patterns for H and V polarized waves in the intervals about $\theta = 90° \pm 20°$ and $\phi = \pm 45°$ (Figure 2-6), there is minimal $Z_{DR}$ bias in this angular sector. In (3-32), $Z'_{dr}$ is coupled with $\rho'_{hv}$ and they need to be solved jointly. Another method is directly correcting the scattering matrix presented in section 3.1.2 Scattering matrix to obtain $Z_{DR}$.

If the STSR mode is used, $Z_{DR}$ bias depends not only on the beam direction, but also on the amplitude ratio and relative phase of transmitted electric fields in the H and V elemental antennas. If the same measurement procedure is implemented on a PPAR as for the mechanically steered beam, the differential reflectivity measured with a PPAR for the STSR mode would be

$$Z_{\mathrm{DR}}^{(p)}(\mathrm{STSR}) = 10\log\left(\frac{\left\langle \left|s_{\mathrm{hh}}^{(p)}\right|^2 \right\rangle}{\left\langle \left|s_{\mathrm{vv}}^{(p)}\right|^2 \right\rangle}\right) \tag{3-33}$$

$$= 10\log\left(\frac{\left|E_{\mathrm{th}}(p_{11}^2 s'_{\mathrm{hh}} + p_{21}^2 s'_{\mathrm{vv}}) + E_{\mathrm{tv}}(p_{11}p_{12}s'_{\mathrm{hh}} + p_{21}p_{22}s'_{\mathrm{vv}})\right|^2}{\left|E_{\mathrm{th}}(p_{11}p_{12}s'_{\mathrm{hh}} + p_{21}p_{22}s'_{\mathrm{vv}}) + E_{\mathrm{tv}}(p_{12}^2 s'_{\mathrm{hh}} + p_{22}^2 s'_{\mathrm{vv}})\right|^2}\right)$$

where the ratio of H and V backscattering matrix elements are given by (3-22). If $p_{21} = 0$, (3-33) is simplified to

$$Z_{\mathrm{DR}}^{(p)}(\mathrm{STSR}) = 10\log\left(\frac{\left|b_{\mathrm{s}}\right|^2 Z'_{\mathrm{dr}}}{\left|c_{\mathrm{s}}\right|^2 Z'_{\mathrm{dr}} + a^2 + 2a\,\mathrm{Re}(c_{\mathrm{s}}\rho'_{\mathrm{hv}})\sqrt{Z'_{\mathrm{dr}}}}\right) \tag{3-34}$$

where

$$a = E_{\mathrm{tv}}p_{22}^2,\quad b_{\mathrm{s}} = E_{\mathrm{th}}p_{11}^2 + E_{\mathrm{tv}}p_{11}p_{12},\quad c_{\mathrm{s}} = E_{\mathrm{th}}p_{11}p_{12} + E_{\mathrm{tv}}p_{12}^2. \tag{3-35}$$

Figure 3-2b, c, d, Figure 3-3c, d, and Figure 3-4 show that the bias of $Z_{\mathrm{DR}}$ for the STSR mode is a function of different parameter values. The bias of $Z_{\mathrm{DR}}$ for the STSR mode is not symmetric about the x-z plane because (3-34) is not symmetric about $\phi = 0$ if the P matrix elements are put into (3-34). The amplitude ratio changes the bias of $Z_{\mathrm{DR}}$ because it produces differences on H and V projected to local H and V directions. The $Z_{\mathrm{DR}}$ bias also depends on the relative phase $\psi$. As $\psi$ changes, the $Z_{\mathrm{DR}}$ bias at the zero azimuth angle does not change, but at any other azimuth angles it changes slightly. The size of patch greatly changes the $Z_{\mathrm{DR}}$ bias as shown in the right panels of Figure 3-3 and Figure 3-4. The correction can also be made by jointly solving $Z'_{\mathrm{dr}}$ and $\rho'_{\mathrm{hv}}$ if the power imbalance and relative phase is small.

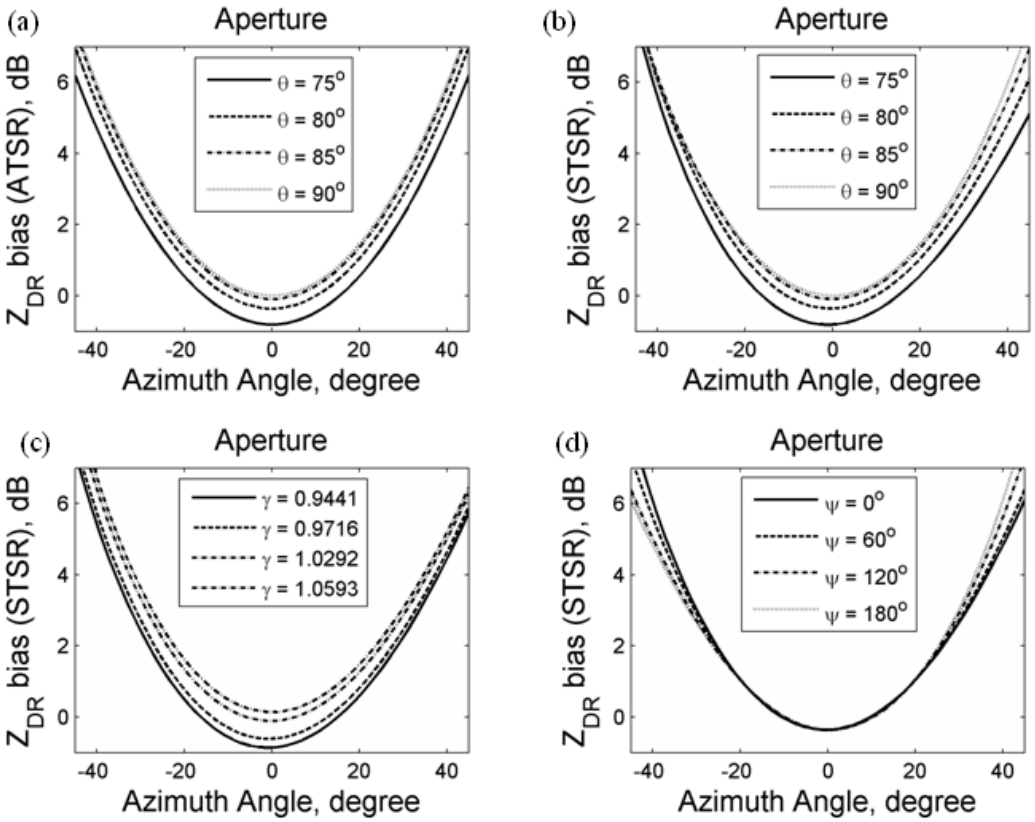


**Figure 3-2** Bias of differential reflectivity PPAR with apertures antenna elements ($TE_{10}$ mode and mounted on an infinite ground plane, $a=0.55\lambda_o$ , $b=0.25\lambda_o$) for the following cases. (a) ATSR mode, various $\theta$ (b) STSR mode, various $\theta$ but $\gamma = 1$ and $\psi = 0^o$. (c) STSR mode, various $\gamma$ but $\theta = 80^o$ and $\psi = 0^o$. (d) STSR mode, various $\psi$ but $\gamma = 1$ and $\theta = 80^o$ . ( $Z'_{dr} = 1.0$ and $\rho_{hv} = 0.9$ in all cases.)

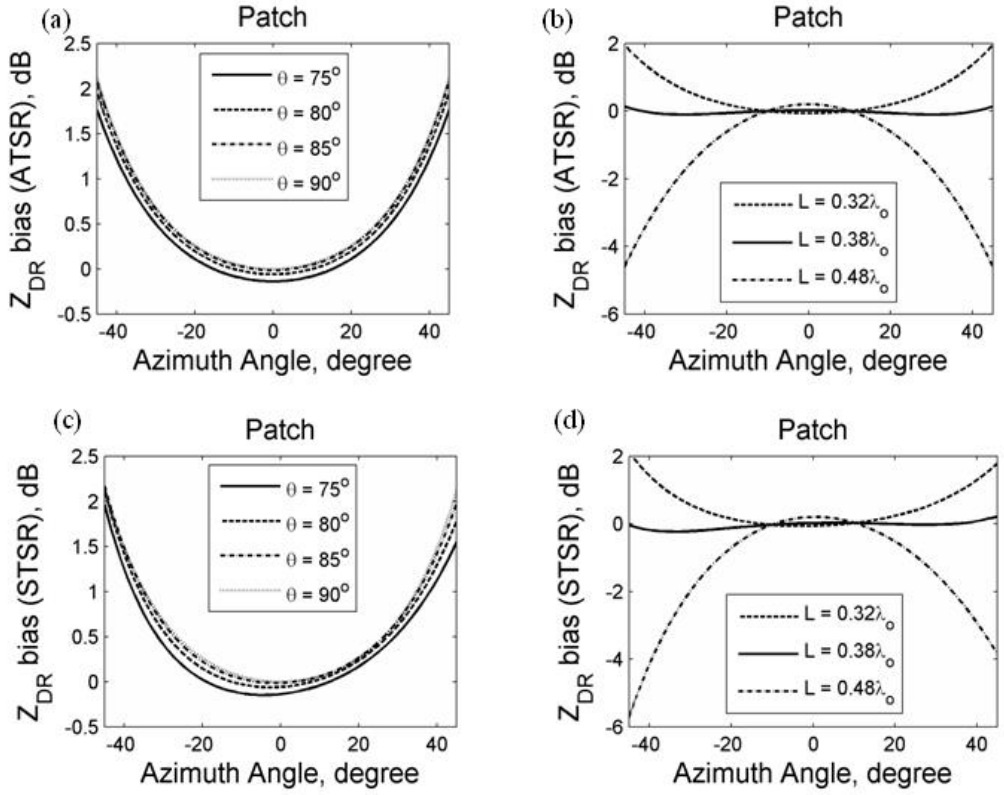


**Figure 3-3** Bias of differential reflectivity of PPAR with patch antenna elements for the following cases. (a) ATSR mode, various $\theta$, but L = $0.32\lambda_o$ (b) ATSR mode, various patch dimension but $\theta = 80^o$ (c) STSR mode, various $\theta$ but $\gamma = 1$, $\psi = 0^o$, and L = $0.32\lambda_o$ (d) STSR mode, various patch dimension but $\theta = 80^o$, $\gamma = 1$, and, $\psi = 0^o$ ($L_e = L / 0.95$ in all cases.)

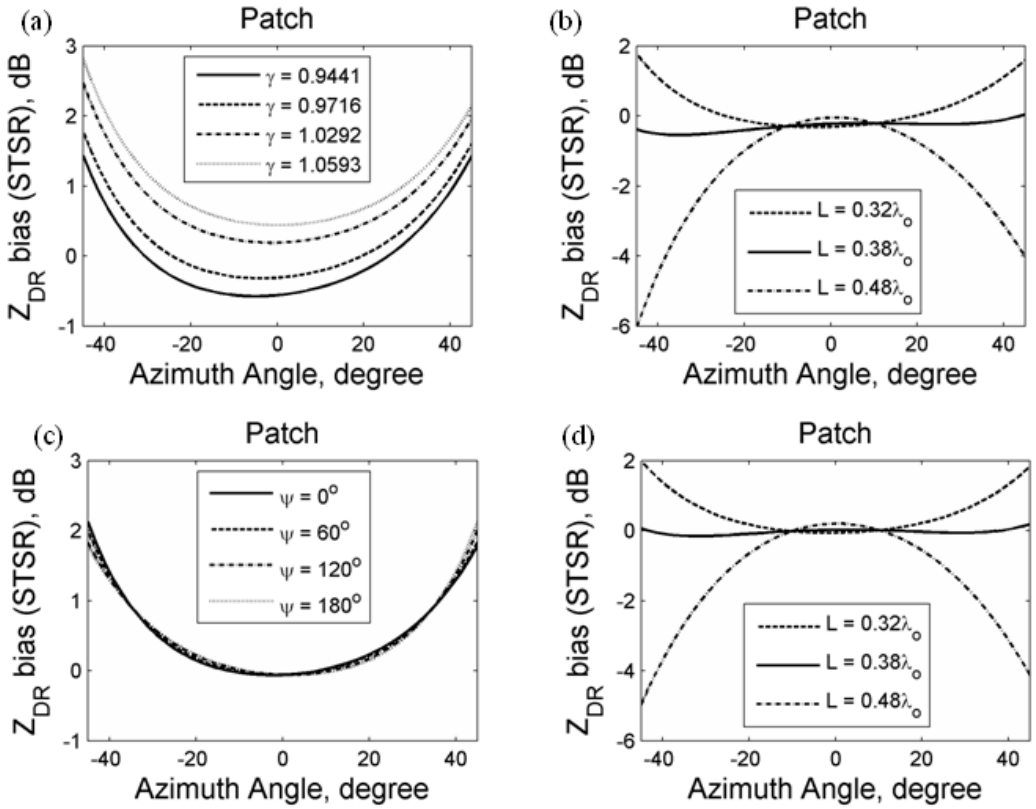


**Figure 3-4** Bias of differential reflectivity of PPAR with patch antenna elements for the following cases: (a) STSR mode, various $\gamma$ but $\theta = 80^o, \psi = 0^o$, and L = 0.32λ$_o$. (b) STSR mode, various patch dimension but $\theta = 80^o$, $\gamma = 0.9716$, and $\psi = 0^o$ (c) STSR mode, various $\psi$ but $\gamma = 1$, $\theta = 80^o$ , and L = 0.32λ$_o$ (d) STSR mode, various patch dimension but $\theta = 80^o, \gamma = 1$, and, $\psi = 60^o$ ($Z'_{dr} = 1.0$, $\rho_{hv} = 0.9$, and $L_e = L / 0.95$ in all cases).

*3.2.3 Correlation coefficient*

The copolar cross correction coefficient between H and V polarizations is defined as (Doviak and Zrnić 2006, sectioin 8.5)

$$\rho_{hv} = \frac{\left\langle s_{hh}^{(b)*} s_{vv}^{(b)} \right\rangle}{\sqrt{\left\langle \left| s_{hh}^{(b)} \right|^2 \right\rangle \left\langle \left| s_{vv}^{(b)} \right|^2 \right\rangle}}. \tag{3-36}$$

For the mechanically steered beam, the measured copolar cross correlation coefficient is

$$\rho'_{\mathrm{hv}} = \frac{\left\langle s'^{*}_{\mathrm{hh}} s'_{\mathrm{vv}} \right\rangle}{\sqrt{\left\langle \left| s'_{\mathrm{hh}} \right|^2 \right\rangle \left\langle \left| s'_{\mathrm{vv}} \right|^2 \right\rangle}} \tag{3-37}$$

The correlation coefficient and the one measured by a mechanically steered beam are related by the differential phase $\phi_{DP}$. That is

$$\rho'_{\mathrm{hv}} = \exp(j\phi_{DP})\rho_{\mathrm{hv}} \tag{3-38}$$

If the same measurement procedure is implemented on a PPAR as for the mechanically steered beam, the correlation coefficient measured by PPAR operated in the ATSR mode is

$$\begin{aligned}
\rho^{(p)}_{\mathrm{hv}}(\mathrm{ATSR}) &= \frac{\left\langle s^{*(p)}_{\mathrm{hh}} s^{(p)}_{\mathrm{vv}} \right\rangle}{\sqrt{\left\langle \left| s^{(p)}_{\mathrm{hh}} \right|^2 \right\rangle \left\langle \left| s^{(p)}_{\mathrm{vv}} \right|^2 \right\rangle}} \\
&= \frac{\left\langle (p^2_{11} s'_{\mathrm{hh}} + p^2_{21} s'_{\mathrm{vv}})^{*} (p^2_{12} s'_{\mathrm{hh}} + p^2_{22} s'_{\mathrm{vv}}) \right\rangle}{\sqrt{\left\langle \left| (p^2_{11} s'_{\mathrm{hh}} + p^2_{21} s'_{\mathrm{vv}}) \right|^2 \right\rangle \left\langle \left| p^2_{12} s'_{\mathrm{hh}} + p^2_{22} s'_{\mathrm{vv}} \right|^2 \right\rangle}} \\
&= \frac{p^2_{11} p^2_{12} Z'^{1/2}_{\mathrm{dr}} + p^2_{21} p^2_{12} \rho'^{*}_{\mathrm{hv}} + p^2_{11} p^2_{22} \rho'_{\mathrm{hv}} + p^2_{21} p^2_{22} Z'^{-1/2}_{\mathrm{dr}}}{\sqrt{\left( p^4_{11} + p^4_{21} Z'^{-1}_{\mathrm{dr}} + 2 p^2_{11} p^2_{21} \mathrm{Re}(\rho'_{\mathrm{hv}}) Z'^{-1/2}_{\mathrm{dr}} \right) \cdot \left( p^4_{12} Z'_{\mathrm{dr}} + p^4_{22} + 2 p^2_{12} p^2_{22} \mathrm{Re}(\rho'_{\mathrm{hv}}) Z'^{1/2}_{\mathrm{dr}} \right)}}
\end{aligned} \tag{3-39}$$

If the array element is ideal, $p_{21} = 0$, and $\rho^{(p)}_{\mathrm{hv}}(A\mathrm{TSR})$ reduces to

$$\rho^{(p)}_{\mathrm{hv}}(\mathrm{ATSR}) = \frac{p^2_{11} p^2_{12} Z'^{1/2}_{\mathrm{dr}} + p^2_{11} p^2_{22} \rho'_{\mathrm{hv}}}{p^2_{11} \cdot \sqrt{p^4_{12} Z'_{\mathrm{dr}} + p^4_{22} + 2 p^2_{12} p^2_{22} \mathrm{Re}(\rho'_{\mathrm{hv}}) Z'^{1/2}_{\mathrm{dr}}}} \tag{3-40}$$

If the PPAR operates in the STSR mode, the measured correlation coefficient is

$$\rho_{\mathrm{hv}}^{(p)}(\mathrm{STSR}) = \frac{\left\langle \left[ E_{\mathrm{th}}(p_{11}^2 s'_{\mathrm{hh}} + p_{21}^2 s'_{\mathrm{vv}}) + E_{\mathrm{tv}}(p_{11}p_{12}s'_{\mathrm{hh}} + p_{21}p_{22}s'_{\mathrm{vv}}) \right]^* \left[ E_{\mathrm{th}}(p_{11}p_{12}s'_{\mathrm{hh}} + p_{21}p_{22}s'_{\mathrm{vv}}) + E_{\mathrm{tv}}(p_{12}^2 s'_{\mathrm{hh}} + p_{22}^2 s'_{\mathrm{vv}}) \right] \right\rangle}{\sqrt{\left\langle \left| E_{\mathrm{th}}(p_{11}^2 s'_{\mathrm{hh}} + p_{21}^2 s'_{\mathrm{vv}}) + E_{\mathrm{tv}}(p_{11}p_{12}s'_{\mathrm{hh}} + p_{21}p_{22}s'_{\mathrm{vv}}) \right|^2 \right\rangle} \sqrt{\left\langle \left| E_{\mathrm{th}}(p_{11}p_{12}s'_{\mathrm{hh}} + p_{21}p_{22}s'_{\mathrm{vv}}) + E_{\mathrm{tv}}(p_{12}^2 s'_{\mathrm{hh}} + p_{22}^2 s'_{\mathrm{vv}}) \right|^2 \right\rangle}} \quad . \tag{3-41}$$

If the array element is ideal, $p_{21} = 0$, and $\rho_{\mathrm{hv}}^{(p)}(\mathrm{STSR})$ reduces to

$$\rho_{\mathrm{hv}}^{(p)}(\mathrm{STSR}) = \frac{a\rho'_{\mathrm{hv}} + c_{\mathrm{s}}\sqrt{Z'_{\mathrm{dr}}}}{\sqrt{a^2 + |c_{\mathrm{s}}|^2 Z'_{\mathrm{dr}} + 2a\sqrt{Z'_{\mathrm{dr}}}\,\mathrm{Re}(c_{\mathrm{s}}\rho'_{\mathrm{hv}})}} \tag{3-42}$$

where $a = E_{\mathrm{tv}} p_{22}^2$, $c_{\mathrm{s}} = E_{\mathrm{th}} p_{11} p_{12} + E_{\mathrm{tv}} p_{12}^2$.

The $\rho_{\mathrm{hv}}$ bias for an aperture element is shown in Figure 3-5, and the $\rho_{\mathrm{hv}}$ bias for a patch element is shown in Figure 3-6 and Figure 3-7. Comparing Figure 3-5 with $\rho_{\mathrm{hv}}$ bias of dipole (Fig.4 and 5 in Zhang et al. 2009), the $\rho_{\mathrm{hv}}$ bias of an aperture element is in mirror symmetry to the $\rho_{\mathrm{hv}}$ bias, if the elements are crossed dipoles. In the ATSR mode (Figure 3-5a and Figure 3-6a) and if $Z'_{\mathrm{dr}} = 1$, the $\rho_{\mathrm{hv}}$ bias of aperture and patch are the same as the $\rho_{\mathrm{hv}}$ bias of dipole (Zhang et al. 2009). As the $Z'_{\mathrm{dr}}$ varies, the $\rho_{\mathrm{hv}}$ bias varies slightly (Figure 3-6b). In the STSR mode, $\rho_{\mathrm{hv}}$ bias depends on the beam direction, the amplitude ratio and relative phase between H and V fields, $Z'_{\mathrm{dr}}$, and the radiation pattern of the antenna element. In Figure 3-6 and Figure 3-7, the patch size does not change the $\rho_{\mathrm{hv}}$ bias at zero azimuths, but at other azimuths the $\rho_{\mathrm{hv}}$ bias are slightly changed by patch size. The $\rho_{\mathrm{hv}}$ bias correction can be done by either directly correcting the scattering matrix or jointly solving $Z'_{\mathrm{dr}}$ and $\rho'_{\mathrm{hv}}$.

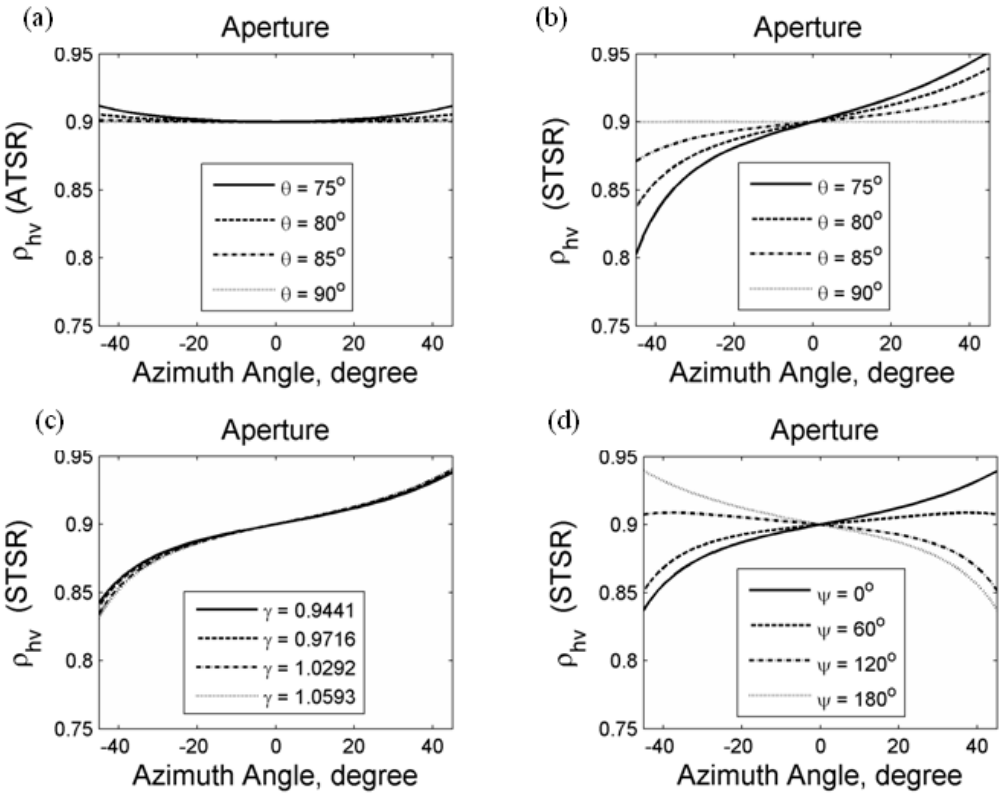


**Figure 3-5** $\rho_{hv}$ of PPAR with aperture antenna elements ($TE_{10}$ mode and mounted on an infinite ground plane, a=0.55$\lambda_o$ , b=0.25$\lambda_o$) for the following cases (a) ATSR mode, various $\theta$ (b) STSR mode, various $\theta$ but $\gamma = 1$ and $\psi = 0^o$. (c) STSR mode, various $\gamma$ but $\theta = 80^o$ and $\psi = 0^o$. (d) STSR mode, various $\psi$ but $\gamma = 1$ and $\theta = 80^o$ . ($Z'_{dr} = 1.0$ and $\rho_{hv} = 0.9$ in all cases.)

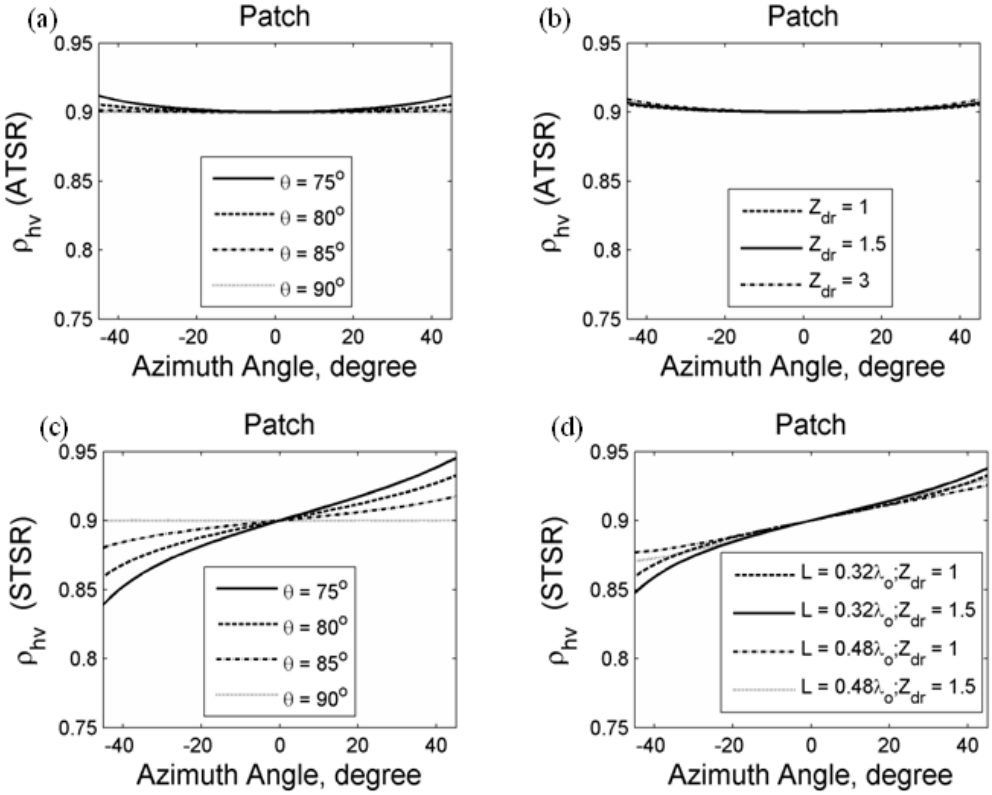


**Figure 3-6** $\rho_{hv}$ of PPAR with patch antenna elements for the following cases. (a) ATSR mode, various $\theta$ but $Z'_{dr} = 1.0$ and $L = 0.32\lambda_o$ (b) ATSR mode, various $Z_{dr}$ but $\theta = 80^o$ ,and $L = 0.32\lambda_o$ (c) STSR mode, various $\theta$ but $Z'_{dr} = 1.0$, $\gamma = 1$, $\psi = 0^o$, and $L = 0.32\lambda_o$ (d) STSR mode, various patch dimension and $Z_{dr}$ but $\theta = 80^o$, $\gamma = 1$, and, $\psi = 0^o$. ( $\rho_{hv} = 0.9$ and $L_e = L / 0.95$ in all cases.)

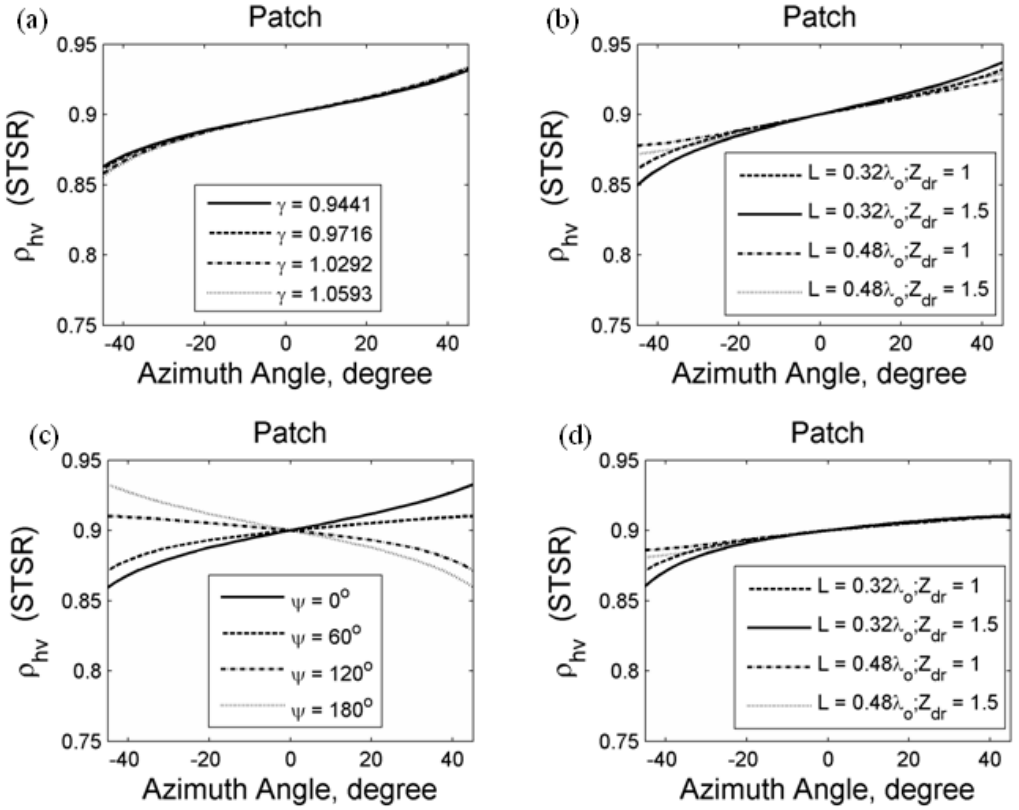


**Figure 3-7** $\rho_{hv}$ of PPAR with patch antenna elements for the following cases. (a) STSR mode, various $\gamma$ but $Z'_{dr} = 1.0$, $\theta = 80^o$, $\psi = 0^o$, and L = 0.32λo. (b) STSR mode, various $Z_{dr}$ and patch dimension but $\theta = 80^o$, $\gamma = 0.9716$, and $\psi = 0^o$ (c) STSR mode, various $\psi$ but $Z'_{dr} = 1.0$, $\gamma = 1$, $\theta = 80^o$, and L = 0.32λo. (d) STSR mode, various $Z_{dr}$ and patch dimension but $\theta = 80^o$, $\gamma = 1$, and, $\psi = 60^o$ ($\rho_{hv} = 0.9$ and $L_e = L / 0.95$ in all cases.)

*3.2.4 LDR (Linear depolarization ratio)*

The LDR can be measured if the ATSR mode is used. $LDR_h$ is the ratio of vertical received power and horizontal received power in dB when horizontally polarized waves are transmitted. If the same measurement procedure is implemented on a PPAR as for the mechanically steered beam, the $LDR_h$ measured by PPAR is given by

$$
\begin{aligned}
LDR_{\mathrm{h}}^{(p)} &= 10\log\left(\frac{\left\langle\left|s_{\mathrm{vh}}^{(p)}\right|^2\right\rangle}{\left\langle\left|s_{\mathrm{hh}}^{(p)}\right|^2\right\rangle}\right) \\
&= 10\log\left(\frac{\left\langle\left|p_{11}p_{12}s'_{\mathrm{hh}} + p_{21}p_{22}s'_{\mathrm{vv}}\right|^2\right\rangle}{\left\langle\left|p_{11}^2 s'_{\mathrm{hh}} + p_{21}^2 s'_{\mathrm{vv}}\right|^2\right\rangle}\right) \\
&= 10\log\left(\frac{p_{11}^2 p_{12}^2 Z'_{\mathrm{dr}} + p_{21}^2 p_{22}^2 + 2p_{11}p_{12}p_{21}p_{22}\sqrt{Z'_{\mathrm{dr}}}\,\mathrm{Re}(\rho'_{\mathrm{hv}})}{p_{11}^4 Z'_{\mathrm{dr}} + p_{21}^4 + 2p_{11}^2 p_{21}^2\sqrt{Z'_{\mathrm{dr}}}\,\mathrm{Re}(\rho'_{\mathrm{hv}})}\right)
\end{aligned}
\tag{3-43}
$$

The intrinsic LDR is negative infinity (in dB) if hydrometeors' axes of symmetry are vertical (i.e., $s_{\mathrm{vh}}^{(b)} = s_{\mathrm{hv}}^{(b)} = 0$).

$\mathrm{LDR_v}$ is the ratio of horizontal received power and vertical received power in dB when vertically polarized waves are transmitted. If the same measurement procedure is implemented on a PPAR as for the mechanically steered beam, the $\mathrm{LDR_v}$ measured by PPAR is given by

$$
\begin{aligned}
LDR_{\mathrm{v}}^{(p)} &= 10\log\left(\frac{\left\langle\left|s_{\mathrm{hv}}^{(p)}\right|^2\right\rangle}{\left\langle\left|s_{\mathrm{vv}}^{(p)}\right|^2\right\rangle}\right) \\
&= 10\log\left(\frac{\left\langle\left|p_{11}p_{12}s'_{\mathrm{hh}} + p_{21}p_{22}s'_{\mathrm{vv}}\right|^2\right\rangle}{\left\langle\left|p_{12}^2 s'_{\mathrm{hh}} + p_{22}^2 s'_{\mathrm{vv}}\right|^2\right\rangle}\right) \\
&= 10\log\left(\frac{p_{11}^2 p_{12}^2 Z'_{\mathrm{dr}} + p_{21}^2 p_{22}^2 + 2p_{11}p_{12}p_{21}p_{22}\sqrt{Z'_{\mathrm{dr}}}\,\mathrm{Re}(\rho'_{\mathrm{hv}})}{p_{12}^4 Z'_{\mathrm{dr}} + p_{22}^4 + 2p_{12}^2 p_{22}^2\sqrt{Z'_{\mathrm{dr}}}\,\mathrm{Re}(\rho'_{\mathrm{hv}})}\right)
\end{aligned}
\tag{3-44}
$$

In Figure 3-8 and Figure 3-9, bias of LDR increases as the beam steers away from $\theta = 90^{\mathrm{o}}; \phi = 0^{\mathrm{o}}$. For a crossed aperture, the $\mathrm{LDR_v}$ bias is a few decibels larger than the $\mathrm{LDR_h}$ bias because the vertical polarized power is lower than the horizontally polarized power at larger $|\phi|$. For patch elements, different sizes of patches can have different

result sets of $LDR_h$ and $LDR_v$ (Figure 3-9b and d). LDR can be corrected by calibrating the scattering matrix.

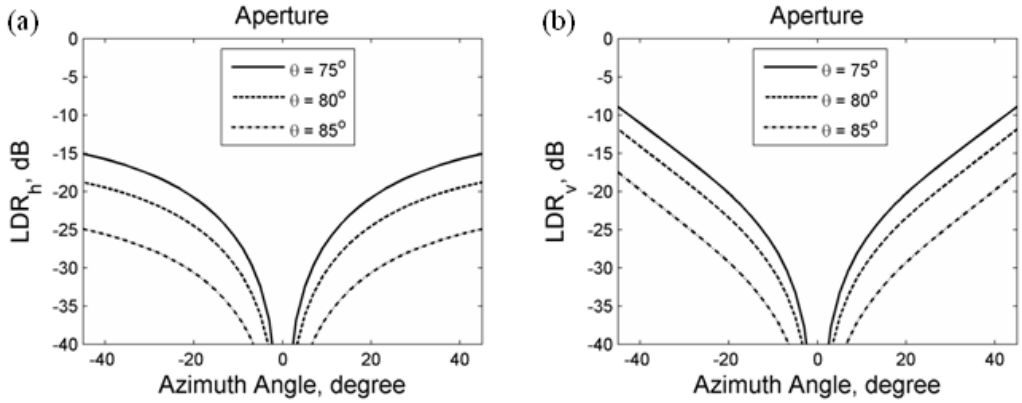


**Figure 3-8** *LDR* versus the electronically steered beam direction of PPAR with aperture antenna elements ($TE_{10}$ mode and mounted on an infinite ground plane, $a=0.55\lambda_o$, $b=0.25\lambda_o$) . (a) $LDR_h$ (b) $LDR_v$ ( $Z'_{dr}=1.0$ and $\rho_{hv}=0.9$ in all cases)

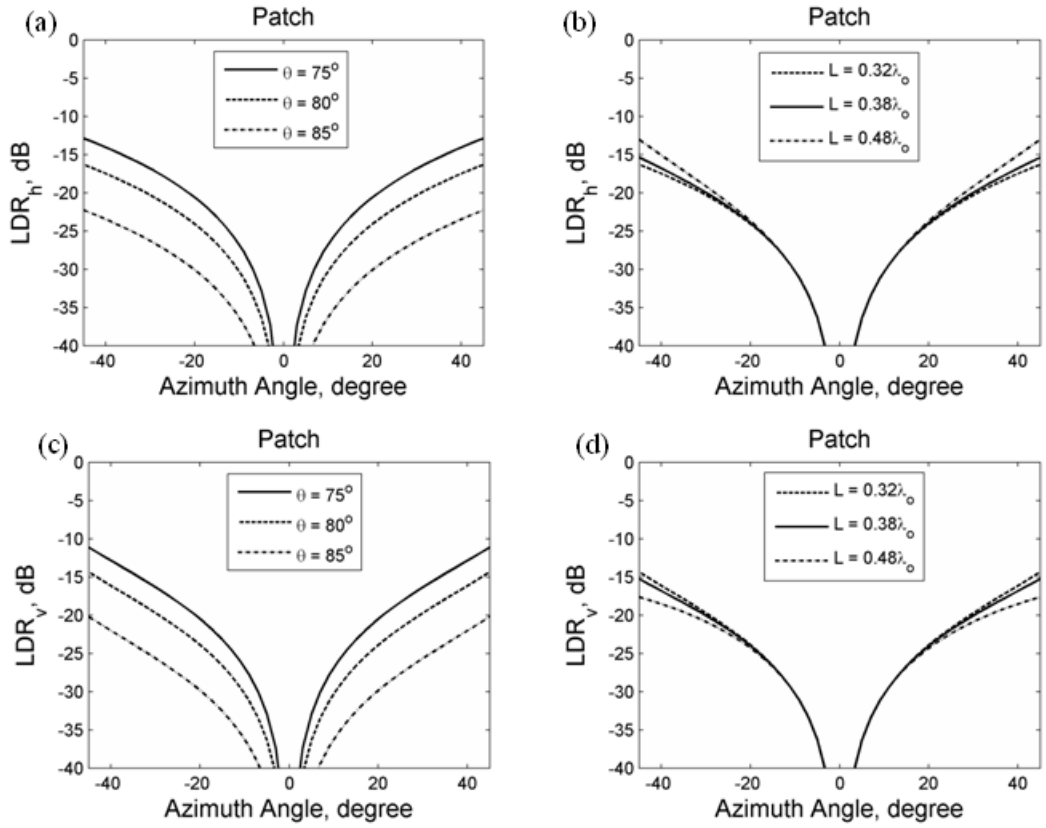


**Figure 3-9** LDR of PPAR with patch antenna elements for the following cases. (a) $LDR_h$, various $\theta$ but $L = 0.32\lambda_o$. (b) $LDR_h$, various patch dimension but $\theta = 80^o$. (c) $LDR_v$, various $\theta$ but $L = 0.32\lambda_o$. (d) $LDR_v$, various patch dimension but $\theta = 80^o$ ($Z'_{dr} = 1.0$, $\rho_{hv} = 0.9$, and $L_e = L / 0.95$ in all cases.)

Ideal aperture and patch radiation elements are studied to correct biases in polarimetric parameters, which are expected if the parameters are measured with the electronically steered beam of a planar polarimetric phased array radar PPAR. It is shown that if the element's far field radiation pattern is known (either from a theoretical formula or measurement), the projection matrix can be found, from which a correction matrix can be derived to mitigate biases. The theoretical projection matrices for aperture and patch elements are derived, and it is shown they are nearly complementary to the

projection matrix for crossed dipoles (section Projection matrix). The projection matrices are related as: $\left(\mathbf{P}_{\text{dipole}}^{T}\right)^{-1} \propto \mathbf{P}_{\text{aperture}}$ and $\left(\mathbf{P}_{\text{dipole}}^{T}\right)^{-1} \propto \mathbf{P}_{\text{patch}}$. The biases expected in PPAR measured polarimetric parameters such as $Z_{\text{DR}}$, $\rho_{\text{hv}}$, and *LDR*, are functions of the element's radiation pattern, beam direction, the copolar correlation coefficient, the reflectivity field, and the array factor. Bias correction of $Z_{\text{DR}}$ and $\rho_{\text{hv}}$ can be done by either directly correcting the scattering matrix or jointly solving $Z'_{\text{dr}}$ and $\rho'_{\text{hv}}$ (sections 3.2.2 Differential Reflectivity and 3.2.3 Correlation coefficient). Bias correction of LDR can be done by calibrating the scattering matrix or by formulas (3-43) and (3-44) . It is shown that by using a patch size to obtain the same patterns for horizontally and vertically polarized fields, the bias of $Z_{\text{DR}}$ is almost zero between elevation 0° to 15° for both ATSR and STSR modes. This is an important property that can be utilized in antenna design for PPAR so that polarization correction is minimal.

For future work, because it is difficult to isolate the H and V polarized waves if they co-exist in each element aperture, the layout and shape of pairs of H and V polarized apertures in an array needs to be considered to minimize coupling. Coupling between array elements and feed lines is another issue that needs to be examined.

### 3.3 Comparison of boresight contribution and integrations

Zhang et al. (2009) and Lei et al. (2013) calculated the biases of polarimetric parameters considering only the boresight contribution of the radiation pattern (i.e., the effect of the entire copolar and cross-polar radiation patterns were ignored). In this

section, we compare the biases from the boresight contributions and those biases calculated when the entire radiation patterns are integrated.

In order to obtain the integral contribution, the formulas in previous section (i.e. the section '2.6 The biases of polarimetric radar parameters calculated by pattern integration') are used. The biases of polarimetric parameters considering only the boresight contribution of patch antenna can be found in Lei et al. (2013). The patch element used in both calculations is shown in Figure 2-7. From Figure 3-10, it is found that the results of integral contribution are very similar to results of boresight contributions. These two only have very slight differences. The reasons are, for weather radar application, beams are narrow, most power is located within the mainlobe, and all sidelobes together contribute a relative small amount of power. Therefore, under these conditions, the simplified boresight formulas in Zhang et al. (2009), Zrnić et al. (2010), and Lei et al. (2013) can be used to calculate biases for PPPAR instead of using complex pattern integration formulas; these boresight formulas are equivalent to multiplying the element pattern with the array factor, provided the beams are directed more than a beamwidth from the principal plane. But patterns of the CPPAR still require complex pattern integration.

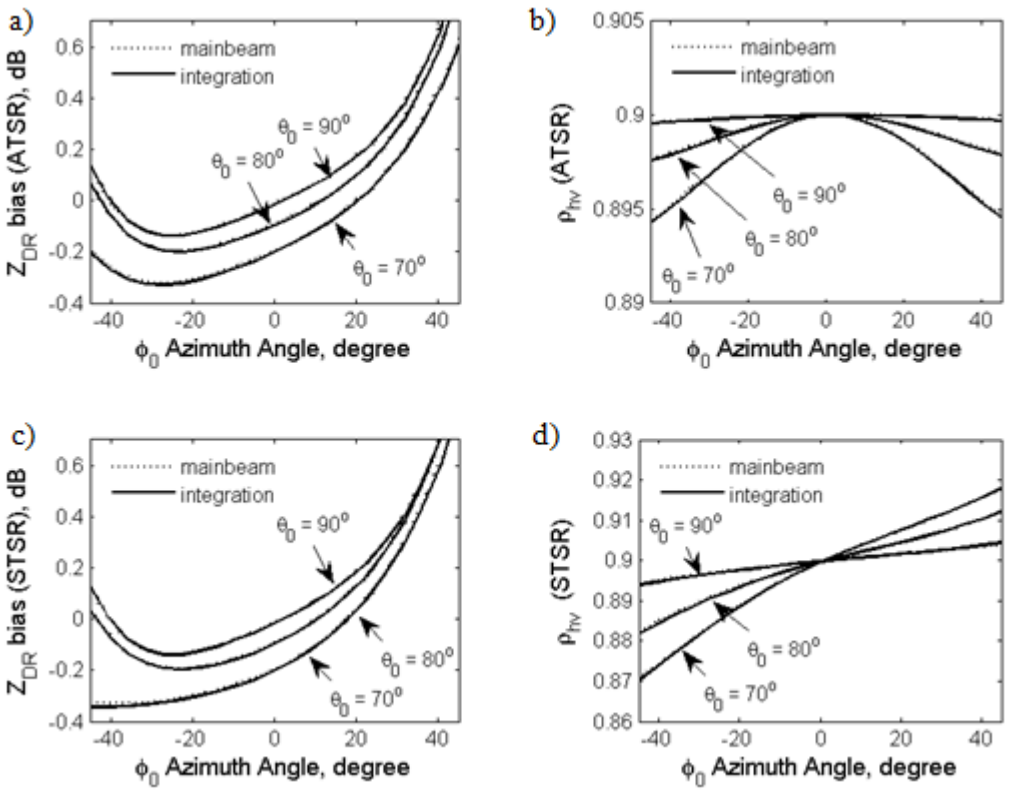


**Figure 3-10** $\rho_{hv} = 0.90$, $Z_{DR} = 1dB$ $\theta_o = 70^o$ with mainbeam's various azimuth angle, tapered. a) $Z_{DR}$ bias ATSR mode, b) $\rho_{hv}$ bias ATSR mode, c) $Z_{DR}$ bias STSR mode, d) $\rho_{hv}$ bias STSR mode

# Chapter 4 CPPAR Bias and Correction

The PPPAR discussed in the previous chapter, however, has significant deficiencies including polarization coupling, the increase in beam width and the loss of sensitivity when its beam scans away from the broadside. One method considers a projection matrix or correction matrix to correct the polarization coupling which has been discussed in chapter 3 (Zhang et al. 2009). Another new method to build a cylindrical polarimetric phased array radar (CPPAR) is introduced by Zhang et al. (2011). CPPAR has the property that the beam is always in the vertical principal plane and thus geometrically introduced cross-polar fields are zero. The incident fields generated from horizontal and vertical polarized antenna port of CPPAR will be orthogonal in all beam directions. The CPPAR would essentially eliminate the beam-to-beam calibration that is required for a PPPAR. In the azimuth, the mainlobe is always at broadside and scan is achieved by shifting the column of active elements. For example, when the mainlobe points to 15 degrees in elevation, the normalized cross-polarization along boresight for cylindrical array is zero (i.e., negative infinity dB) (Balanis 1997), but has cross-polar peaks and its left and right nearby pixel pattern values are about −28dB. The very low cross-polorization effect of CPPAR benefits from its symmetric structure in all azimuths.

The CPPAR is divided into four equal sectors (i.e., 90 degrees angle per sector), as shown in Figure 2-2. Each sector forms one beam. Radar beams scan similar to the way a fan rotates. The curvature of the cylindrical surface will cause an undesired pattern increase at far angles, which might be caused by asymmetrical and blockage of

the cylindrical phased array at far angles. Four equal sectors are chosen because then the undesired pattern increase is within an acceptable range.

### 4.1 Bias of CPPAR

In this section, the biases of CPPAR polarimetric radar parameters are calculated. General formulas are derived in the last section of Chapter 2, but results are presented for patch elements on planar and cylindrical surfaces, and operating at a frequency of 2.705 GHz—this frequency has been chosen because it is the one for KOUN, a prototype dual polarimetric WSR-88D for which we have radiation pattern measurements to compare with theoretical patterns presented in Chapter 2 '2.4.1 WSR-88D radiation patterns'. The HFSS simulated patch element shown in Figure 2-7 are used to calculate the biases from Figure 4-1 to Figure 4-4.

Figure 4-1 shows the biases of $Z_{\mathbf{DR}}$, $|\rho_{\mathbf{hv}}|$ and $\phi_{dp}$ as functions of $\theta_e$ with $\phi_0 = 45^o$ for the three antennas (Figure 2-2) operating in the STSR mode. Here we assume that true $Z_{\mathbf{DR}}$ is a constant independent of elevation angle. There are multiple sources of cross-polar fields that can cause bias (e.g., radiation from the so-called non radiating sides of the patch in Balanis (1997, chapter 14)); edge effects associated with the finite size ground plane; geometrically induced cross-polar field, etc). Another source of bias is the differential gains in the H and V copolar radiation patterns of the patch.

In Figure 4-1, the PPPAR and CPPAR elements have weights given by (2-2) and (2-3) but without density and polarimetric compensation. Therefore, both the bias

caused by the geometrically induced cross-polar field and the bias caused by differential gains in the H and V contribute the biases shown in Figure 4-1a. In Figure 4-1a, as the elevation angle increases, the PPPAR $Z_{DR}$ bias decreases because the horizontally polarized patch fields (Figure 2-7b) reduce more than the vertically polarized patch fields (Figure 2-7c). For the planar array, the $Z_{DR}$ bias is always positive at azimuth $45^{o}$, which is consistent with the results in Lei et al. (2013) when patch length L is $0.32\lambda$. The size of the patch influences the ratio of H and V of gains and therefore influences the sign of the $Z_{DR}$ bias. The CPPAR has much lower $Z_{DR}$ and $\rho_{hv}$ biases than the PPPAR. Because the CPPAR beam is azimuthally steered by commutation, the beam is always in a vertical principal plane which rotates azimuthally and synchronously with the beam. If the H and V gains of the patch were matched, the theoretical bias of the CPPAR would be zero as is the bias for the the WSR-88D and will be shown in the next section '4.2 Partial bias reduction of PPAR: adjusting antenna port voltages'. Therefore, the small negative increase of $Z_{DR}$ bias for the CPPAR (Figure 4-1a) is due to the differential gain of the patch.

Applying Eqns. (2-20) to (2-27) to the theoretical patterns of WSR-88D and integrating $\theta$ and $\Phi$ from -30 degrees to 30 degrees, the $Z_{DR}$ and $\rho_{hv}$ biases for WSR-88D are obtained. To save computational time, we choose ± 30 degree about boresight—because most powers are located inside this region, and integration outside this region doesn't affect the results. The $Z_{DR}$ bias is -0.0005 dB. In Zrnić et al. (2010), the $Z_{DR}$ bias, assuming a Gaussian shape for the main lobe for the cross-polar field with a peak of -35.5dB, is about -0.0016 dB.

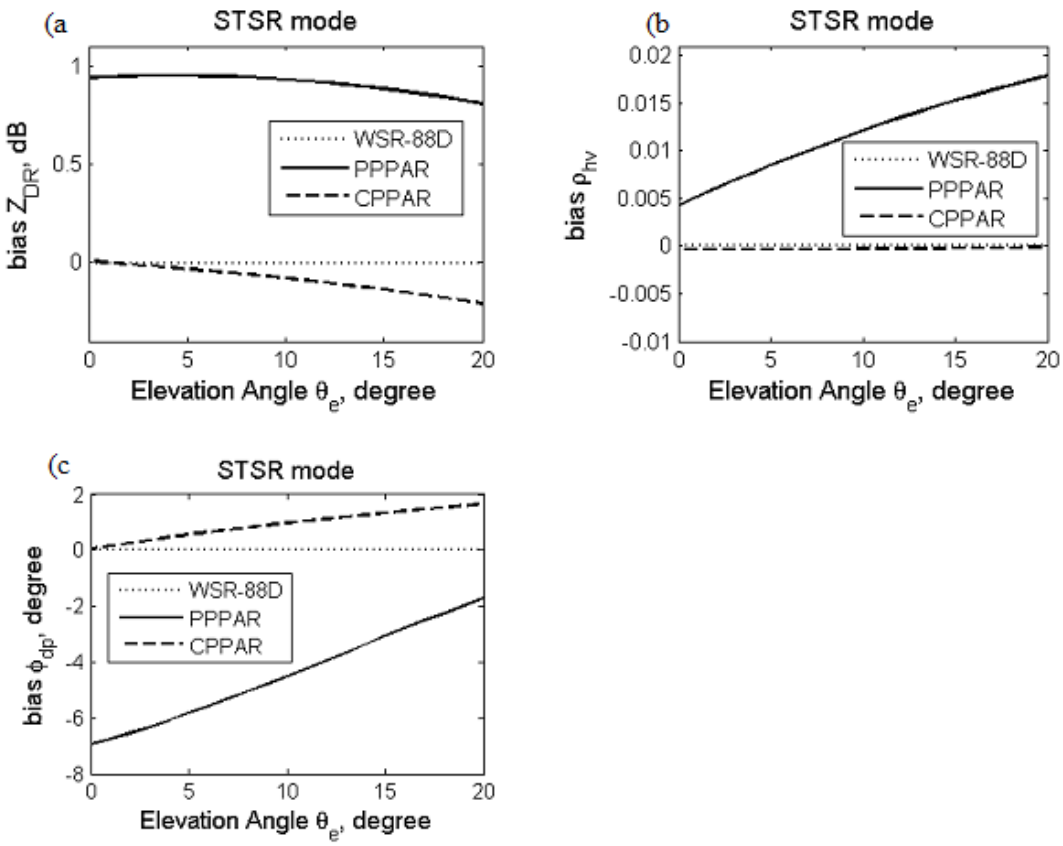


**Figure 4-1** Biases vs beam's elevation angle $\theta_e$ for the STSR mode. $\rho_{hv} = 0.90$, $Z_{dr} = 1$, $\phi_{DP} = 0$. Density and rotational compensation are not included. The beam is pointed at $\phi_0 = 45^o$, a) $Z_{DR}$ bias, b) $\rho_{hv}$ bias , c) $\phi_{dp}$ bias.

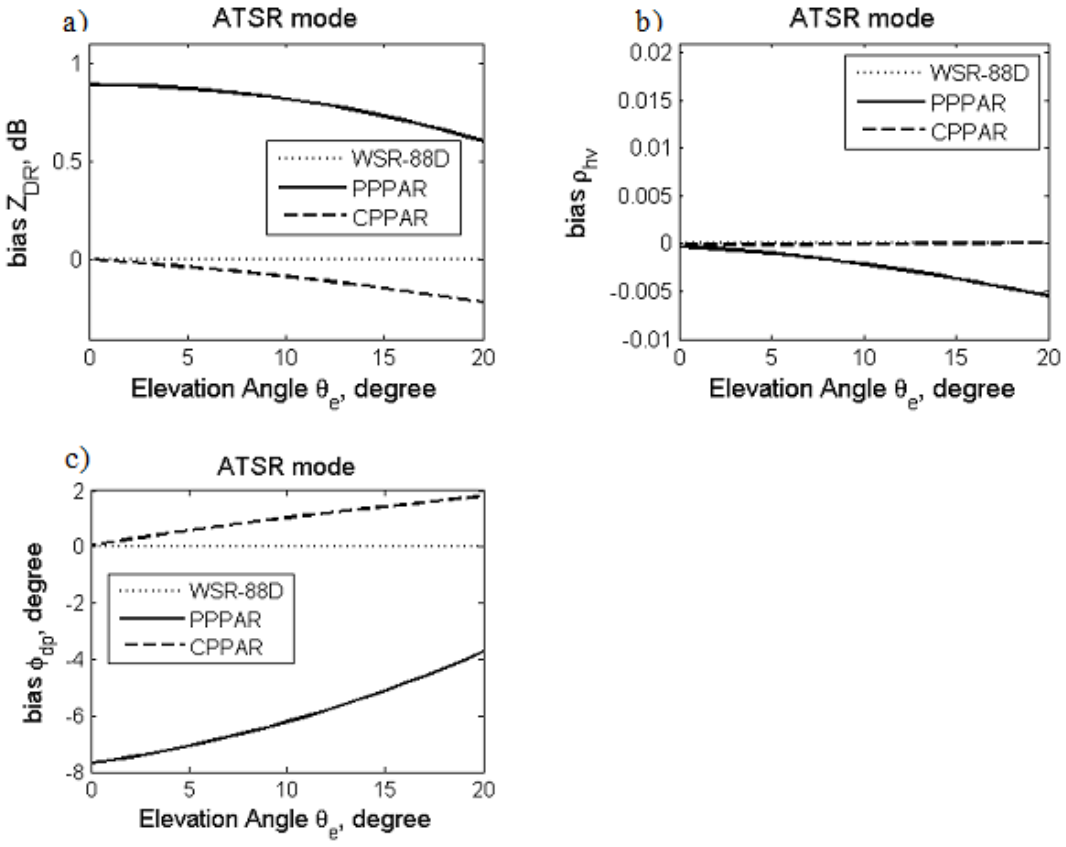


**Figure 4-2** Biases vs beam's elevation angle $\theta_e$ for the ATSR mode, $\rho_{hv} = 0.90$, $Z_{dr} = 1$, $\phi_{DP} = 0$. Density and rotational compensation are not included. The beam is pointed at $\phi_0 = 45^o$, a) $Z_{DR}$ bias, b) $\rho_{hv}$ bias , c) $\phi_{dp}$ bias.

### 4.2 Partial bias reduction of PPAR: adjusting antenna port voltages

In this section, input voltages are adjusted to partially correct $Z_{DR}$ biases due to PPPAR and CPPAR H and V copolar peak gain differences. To obtain the adjustment factors to the input voltages to correct the imbalance in the H and V copolar fields, we neglect the cross-polar terms of $\ddot{\mathbf{F}}$ in (2-17). The copolar transmit and receive patterns are the same, so we only need to derive the voltage adjustments to achieve equal H, V boresight fields incident on the scatterer. The voltage adjustments to achieve equal echo power for spherical scatterers require an additional adjustment which simply is the

square of the adjusted input voltages derived herein. Under these conditions and in the boresight direction, we have

$$\begin{bmatrix} F_{\mathrm{hh}}(\theta_0,\varphi_0) & F_{\mathrm{hv}}(\theta_0,\varphi_0) \\ F_{\mathrm{vh}}(\theta_0,\varphi_0) & F_{\mathrm{vv}}(\theta_0,\varphi_0) \end{bmatrix} \begin{bmatrix} V_{\mathrm{th}} \\ V_{\mathrm{tv}} \end{bmatrix} \\ = \begin{bmatrix} F_{\mathrm{hh}}(\theta_0,\varphi_0)V_{\mathrm{th}} + F_{\mathrm{hv}}(\theta_0,\varphi_0)V_{\mathrm{tv}} \\ F_{\mathrm{vh}}(\theta_0,\varphi_0)V_{\mathrm{th}} + F_{\mathrm{vv}}(\theta_0,\varphi_0)V_{\mathrm{tv}} \end{bmatrix} \approx \begin{bmatrix} F_{\mathrm{hh}}(\theta_0,\varphi_0)V_{\mathrm{th}} \\ F_{\mathrm{vv}}(\theta_0,\varphi_0)V_{\mathrm{tv}} \end{bmatrix} \tag{4-1}$$

Eqn. (4-1) applies to PPPAR. For CPPAR, all $\varphi_0$ in Eqn. (4-1) is replaced with $\varphi_0 - \varphi_n$. To calculate $Z_{DR}$ and $\rho_{hv}$ bias we are concerned with received power, so we can neglect the received echo phases. We could adjust both input voltages so that the total input power remains the same, but to simplify our analyses we assume only the H port patch voltage is adjusted so H and V echo powers are equal. In this case the adjusted H port patch power needs to be

$$\left(V_{\mathrm{th}}^{(a)}\right)^2 = \left(\frac{F_{\mathrm{vv}}(\theta_0,\varphi_0)}{F_{\mathrm{hh}}(\theta_0,\varphi_0)}\right)^2 \left(V_{\mathrm{tv}}\right)^2 \tag{4-2}$$

which applies to the PPPAR. For CPPAR, all $\varphi_0$ in Eqn. (4-2) are replaced with $\varphi_0 - \varphi_n$, where $\phi_o$ and $\phi_n$ are defined in Eqn. (2-3). But for the CPPAR the relative copolar gain varies only with changes in elevation angle. Because the array factor gain is independent of the polarization, the relative H and V gain functions in Eqn. (4-2) are those associated with the array element. But the relative gain of the array is needed in Eqn. (4-2) to correct reflectivity biases as a function of beam direction.

Because in Chapter 2 section '2.6 The biases of polarimetric radar parameters calculated by pattern integration,' bias formulas are derived assuming magnitudes of

$V_{\text{th}}$ and $V_{\text{tv}}$ are equal. In this section we apply voltages given by Eqn. (4-2) to correct for changes differential H, V gains. Moreover, because in section 3 we computed CPPAR radiation patterns without compensating for polarization and element density effects for the CPPAR, we have included those and recalculated the radiation matrix for the CPPAR including these compensations. However, the biases formulas derived in Chapter 2 still apply just by replacing $\ddot{\mathbf{F}}$ with $\ddot{\mathbf{F}}'$, which is given by

$$\ddot{\mathbf{F}}'=\begin{bmatrix} F'_{\mathbf{hh}} & F'_{\mathbf{hv}} \\ F'_{\mathbf{vh}} & F'_{\mathbf{vv}} \end{bmatrix}=\begin{bmatrix} \dfrac{F_{\mathbf{hh}}}{F_{\mathbf{hh}}(\theta_0,\varphi_0)} & \dfrac{F_{\mathbf{hv}}}{F_{\mathbf{vv}}(\theta_0,\varphi_0)} \\ \dfrac{F_{\mathbf{vh}}}{F_{\mathbf{hh}}(\theta_0,\varphi_0)} & \dfrac{F_{\mathbf{vv}}}{F_{\mathbf{vv}}(\theta_0,\varphi_0)} \end{bmatrix} \tag{4-3}$$

which applies to the PPPAR for the gain compensation. For CPPAR, polarization compensation is more complicated obtained by $\dfrac{1}{F_{\mathbf{hh}}(\theta_0,\varphi_n-\varphi_0)}$ for horizontal polarization and $\dfrac{1}{F_{\mathbf{vv}}(\theta_0,\varphi_n-\varphi_0)}$ for vertical polarization (that is all $\varphi_0$ in Eqn. (4-3) are replaced with $\varphi_0-\varphi_n$). For the CPPAR, the element density is not uniform as with the PPPAR. So the density compensation for the CPPAR is simply obtained by applying the multiplicative factor to $\cos(\phi_o-\phi_n)$ to Egn. (2-3) as did (Zhang et al. 2011).

The CPPAR and PPPAR $Z_{\text{DR}}$ and $\rho_{\text{hv}}$ biases, recalculated using adjusted voltages and the modified radiation matric $\ddot{\mathbf{F}}'$ for the CPPAR, are presented in Figure 4-3 and Figure 4-4 for the STSR and ATSR modes of data collection.

After differential gain compensation, $Z_{\mathbf{DR}}$ biases are greatly reduced. Comparing Figure 4-1a and Figure 4-3a, the $Z_{DR}$ bias caused by different gains of H and V is larger than the $Z_{DR}$ bias caused by geometrically induced cross-polar fields. In Figure 4-3a, $Z_{\mathbf{DR}}$ biases for the CPPAR and WSR-88D are equal and zero for all directions. Moreover, although the $Z_{DR}$ bias for the PPPAR is significantly larger than for the CPPAR, the bias at low elevation angles less than $20^o$ is acceptably small.

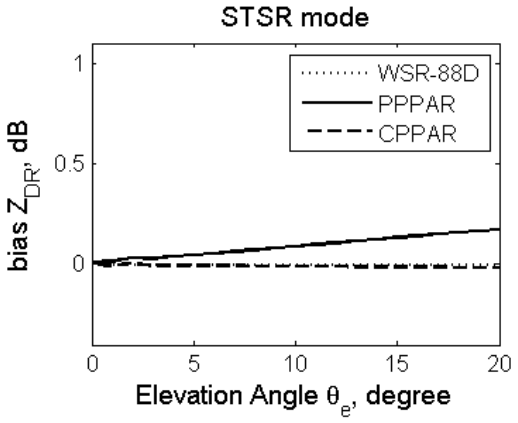


**Figure 4-3** $Z_{DR}$ bias after input voltage adjustments vs beam's elevation angle $\theta_e$ for the STSR mode ( $\phi_0 = 45^o$, $\rho_{hv} = 0.90$, $Z_{dr} = 1$, $\phi_{DP} = 0$ ).

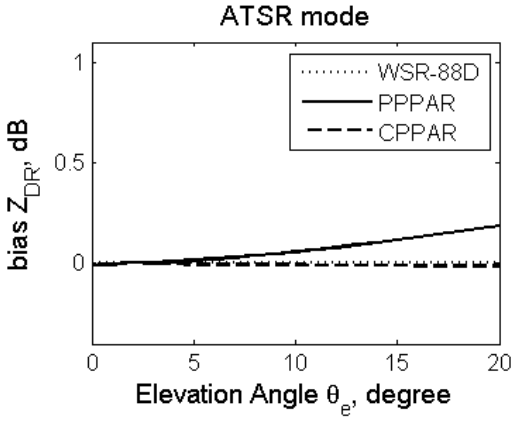


**Figure 4-4** As Fig.4-3, but for the ATSR mode.

Another method to decrease the incident cross-polar fields can be acheived by adjusting H and V port voltages of PPAR. Specificly, it is realized by transmiting H and a small amount of V (or by transmiting V and a small amount of H) to obtain a pure $E_\phi$ (or $E_\theta$) field(Lei et al. 2012).

## 4.3 Characteristics of CPPAR

Array lattices and element separations are examined using simulations to determine the optimal configuration that has the desired sidelobe level and cross-polarization isolation needed for quality precipitation measurements. The simulation results are verified by the linear and ring array theory. Different lattice structures (i.e., rectangular and triangular) and their corresponding performances are compared, yielding the minimum number of array elements. Copolar and cross-polar pattern changes caused by 1) errors in mechanical positioning of the array elements, 2) quantization errors of the phase shifters, and 3) elements failures, are also examined. Tolerable error limits are provided for system design.

### *4.3.1 Element Separation and Grating lobes*

The cylindrical array can be considered as a combination of linear arrays in elevation and ring arrays in azimuth. For weather radar, the scan domain is always between 0° and 30° in elevation. For linear arrays, a scan to 30° without grating lobes in visible space needs element spacing (Balanis 1997, chapter 6):

$$\frac{d}{\lambda_0} = \frac{1}{1+\sin(30^o)} = 0.6667 \tag{4-4}$$

where $d$ is the element spacing and $\lambda_0$ is the free space wavelength. Therefore a $0.6667\lambda_0$ vertical direction separation of elements on the cylindrical array will place the grating lobe outside $30^o$ of visible space in elevation, as will be shown in the following section "Array Lattice". For the horizontal separation, ring array theory can be found in Hansen (2009). The azimuth $\phi$ of the grating lobe is approximated by

$$\sin(\frac{\phi}{2}) \approx -\frac{r}{2s} \tag{4-5}$$

Where $r = 0, \pm 1, \pm 2, ...$ and s is the inter-element spacing on the ring and normalized by $\lambda_0$ . $r = 0$ gives the mainlobe at $\phi = 0$ . Positive and negative $r$ give grating lobes at positive and negative $\phi$ under the condition $\left| r/2s \right| \le 1$ . To eliminate grating lobes in the visible space (i.e. front half hemisphere of array), we choose $\phi = \pm 90^o$ and the separation turns out to be $s \approx 0.707$ . In theory, the critical point (i.e., where the grating lobe is at the edge of visible space) is $0.707\lambda_0$ separation. However, the computed critical separation obtained from our simulation is s = 0.73, which is a little larger than theory, but consistent with Hansen (Fig. 11.5 in Hansen 2009).

*4.3.2 Array Lattice*

The element lattice is designed according to the scan domain and the specified location of the grating lobes. If the scan domain is defined, an optimum lattice design uses a minimum number of elements to eliminate the peak of the grating lobes from being inside the visible space.

First, the critical points of grating lobes just outside the visible space, for the three lattices shown in Figure 4-6, are shown in Figure 4-5. In Figure 4-5, a sine space coordinate system is used in which $w = \cos\theta$, $v = \sin\theta\cos\phi$. The dots outside the unit circle are the grating lobe locations if the mainlobe is at broadside (i.e., the centers of the circles). The green arrows represent the shift of the grating lobe locations when the beam is scanned to 30° in elevation. The green arrow inside the unit circle is the scan domain of the radar, and the arrow length is cos(60°) − cos(90°) = 0.5.

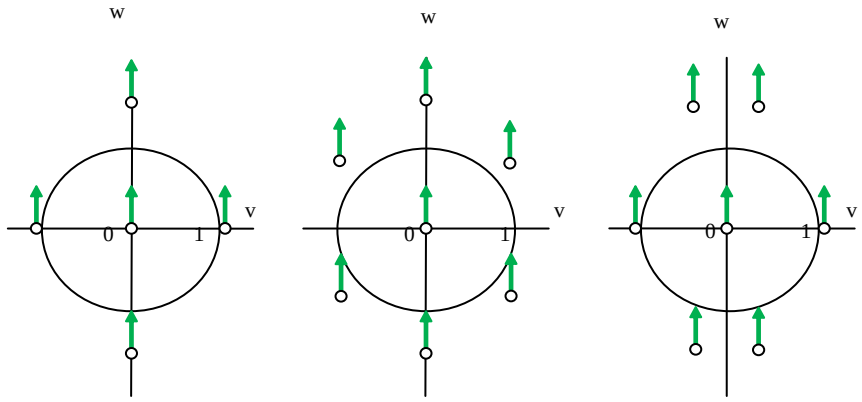


**Figure 4-5** Sine-space grating-lobe locations for three lattice structures shown in **Figure 4-6**: rectangular lattice (left panel), horizontally staggered triangular lattice (center panel), and vertically staggered triangular lattice (right panel)

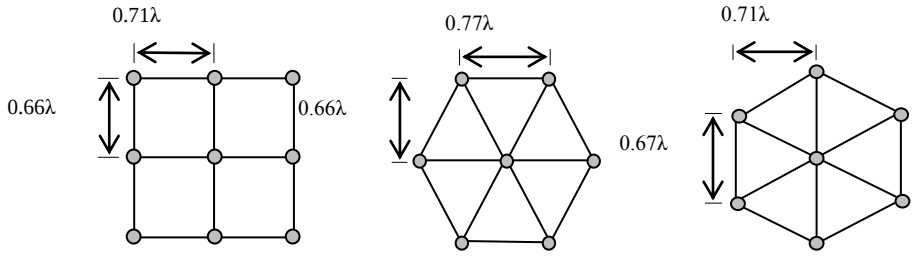


**Figure 4-6** Three lattice structures of array elements: Rectangular lattice (left), horizontally staggered triangular lattice (center), and vertically staggered triangular lattice (right)

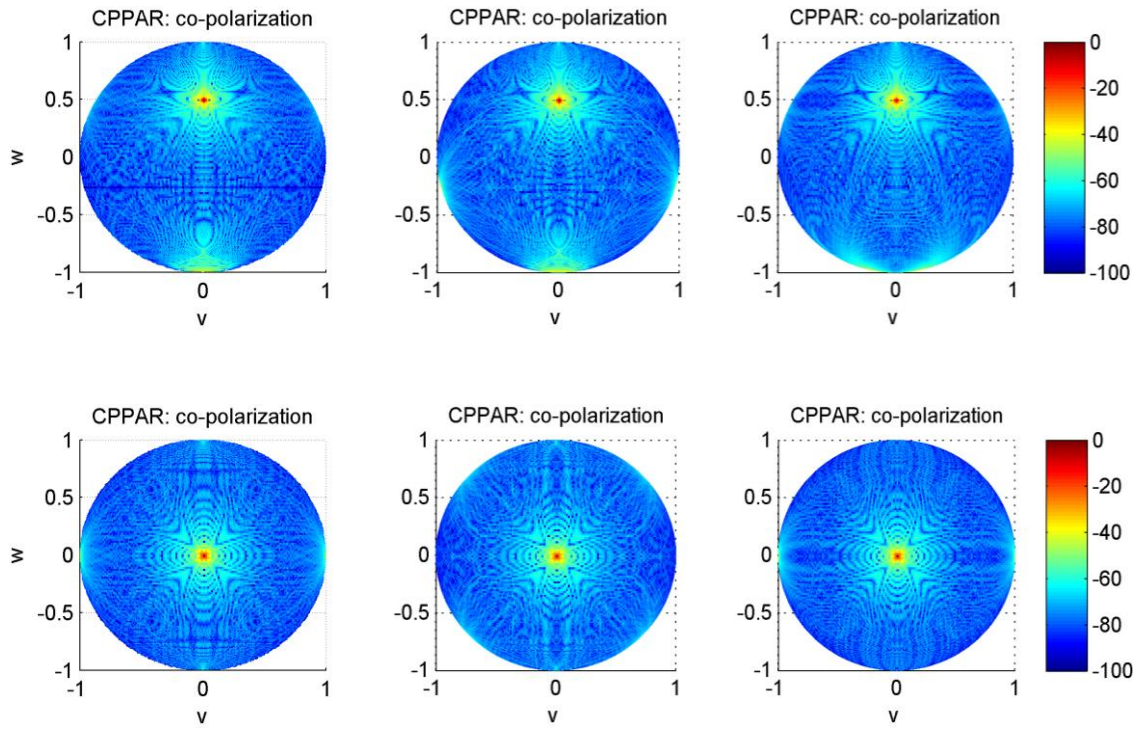


**Figure 4-7** Patterns for main beam at broadside (bottom row) and 30° elevation (top row) for the three corresponding lattice structures shown in **Figure 4-6**.

Then, a set of simulations is run for various element separations, for each of the three lattice structures shown in Figure 4-5. The set of seperations that generated copolar radiation patterns that satisfied the conditions given in the next paragraph are entered into Figure 4-6, and the corresponding patterns are presented in Figure 4-7. The corresponding simulation results for the element separations given in Figure 4-6 generate one-way patterns (Figure 4-7) that satisfy the specified conditions.

For the simulation, the cylindrical array size is specified to be 8.54m in height and 6.0387m in radius. If an angular sector of active elements is 90°, this CPPAR antenna will generate a 1° beam, one comparable to that of the WSR-88D. This is so because the projection of each 90° sector onto a plane perpendicular to the beam of

cylindrical array is the same size as the area of the WSR-88D's antenna. Array elements are crossed horizontal and vertical free space dipoles so that both H and V polarized waves can be transmitted and received. A taper is applied to the excitation of the array elements so as to mimic the aperture distribution of WSR-88D given by Eqn. (2-3). If the grating lobes lie just outside visible space and the value of grating lobes at the edge are set to be just below $-30$dB, the element separation is determined and recorded in Figure 4-6.

Rectangular lattice

Due to its easier fabrication, a rectangular lattice is most common and is studied first. In the left panel of Figure 4-5, the grating lobe coming in from the bottom determines the element spacing in the vertical direction; $0.66\lambda_0$ entered into Figure 4-6 is determined by running a set of simulations. The grating lobes that come in from left and right determine the azimuth separation (i.e., $0.71\lambda_0$ circumferential distance along the ring); this is also determined by running a set of simulations. The agreement of the element spacing obtained from simulations and that obtained from theory for the linear and ring array given in the previous section verify the correctness of the simulation. The broadside and 30° patterns are shown in the left two panels in Figure 4-7. The color scale of the patterns in this dissertation shows that the patterns are all dB below the mainlobe peak.

Triangular lattice

Triangular lattice has two forms: a horizontally staggered triangular lattice and a vertically staggered one. The middle panel in Figure 4-5 is grating lobes at the edge of visible space for the horizontally staggered lattice. The bottom grating lobe determines the vertical separation of elements; the separation of $0.66\lambda_0$ was obtained from running a set of simulations. The azimuth separation of the lattice is determined by lower left and lower right grating lobes when beam scans to a 30 degree elevation. By running a set of simulated patterns for different azimuth spacings, the azimuth separation of $0.77\lambda_0$ was obtained as shown in the middle panel of Figure 4-6. The corresponding copolar patterns are shown in the middle two panels in Figure 4-7. Similarly, the element separations for vertically staggered lattice are determined and are shown in the right panels of Figure 4-5, Figure 4-6, and Figure 4-7.

Let's take the horizontally staggered triangle lattice as an example to calculate the spacing using the relation of grating lobe locations and element separation. For planar array, theoretically derived formulas for grating lobe location and element separation relationship in sine space are availabe (Hansen 2009, chapter 2.2). However, there are no available formulas of grating lobe locations and element separation relationship for cylindrical array. Therefore, the methods for planar array are modified to predict the grating lobe location and element separation relationship for CPPAR. Here is an example of how we use the sine space to calculate the element separation by avoiding grating lobe locations for CPPAR. In Figure 4-8, due to curvature of CPPAR, the grating lobes move along curved lines when the beam does an elevation scan. Dots represent grating lobe locations. The green arrow inside the unit circle gives the scan

domain and its length is cos(60°)=0.5. If the bottom grating lobe is at the edge of unit circle when scanning to 30° elevation, coordinates of dot A before scanning (i.e., beam at broadside) are ( − 1.5,0). Then, the y coordinate of dot B is calculated by $-1.5/2+\cos(60°) = -0.25$. Because dot B is on the unit circle, coordinates of B are (0.9682, $-0.25$), and the azimuth and elevation angles of B are about 90° and $-14.48°$ respectively. Element spacing can be approximately calculated using the equation (Hansen 2009):

$\sin(\phi/2) \approx -r/2s\cos(\theta)$, where $\theta$ is the elevation angle in Fig.11.12 in Hansen (2009). The azimuth separation is given by $s \approx 1/[2\cos(-14.48^o)\sin(45^o)] = 0.73$. Vertical separation is $1/1.5 = 0.667\lambda_0$. If grating lobes are outside unit circle and set to be $-30$dB which is an acceptable sidelobe level for weather radar, the separations are slightly smaller than these. Therefore, theoretically derived separations approximate the separations obtained from simulations as shown in the middle panel of Figure 4-6.

Due to the curvature of cylindrical array, there are denser columns than rows projected onto an equivalent planar array. Therefore, the horizontally staggered lattice, which makes the columns dense, uses fewer array elements than the vertically staggered lattice, which makes the rows dense. To achieve the same grating lobes performance, the element ratio of rectangular vs. triangular lattice is 100:92. Thus the triangular lattice has 8% fewer elements compared with the rectangular lattice. Normally, a triangular lattice saves 15% elements for a planar array.

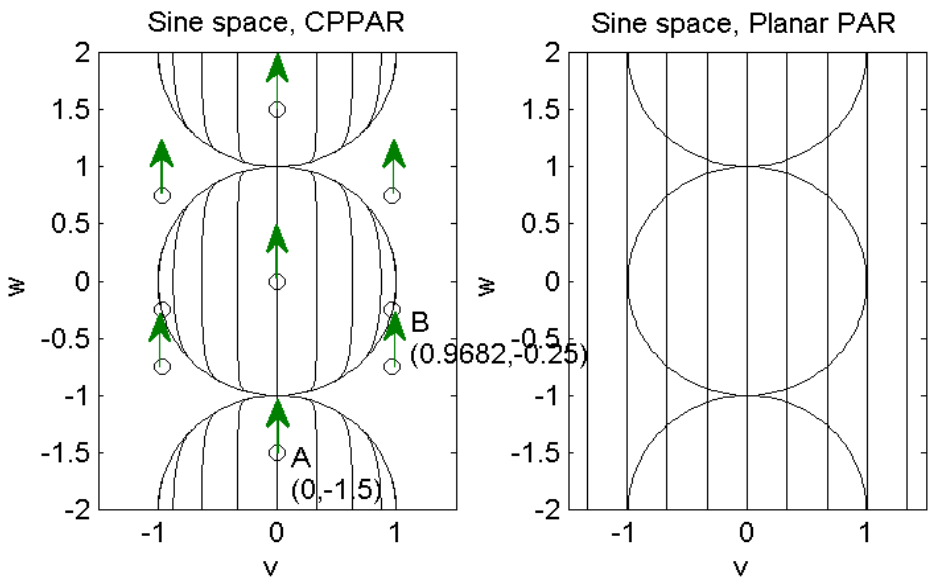


**Figure 4-8** Grating lobe paths of CPPAR and PPPAR

*4.3.3 Error Effects*

Copolar and cross-polar radiation patterns are affected by 1) errors in mechanical positioning of the array elements, 2) element failures, and, 3) errors in the phase shifter; changes in radiation patterns are now discussed.

Radiation pattern changes due to errors in positioning array elements (Figure 4-9) shows that copolar sidelobes increase by less than 10 dB for standard errors in locating elements is less than 0.05 cm in x, y, or z direction, and cross-polar radiation increases by less than 10dB. Thus containing increases in copolar sidelobes and cross-polar radiation should be relatively easy achievable for the 10-cm wavelength weather radar because fabrication techniques should be capable of placing element with accuracies finer than a half a mm.

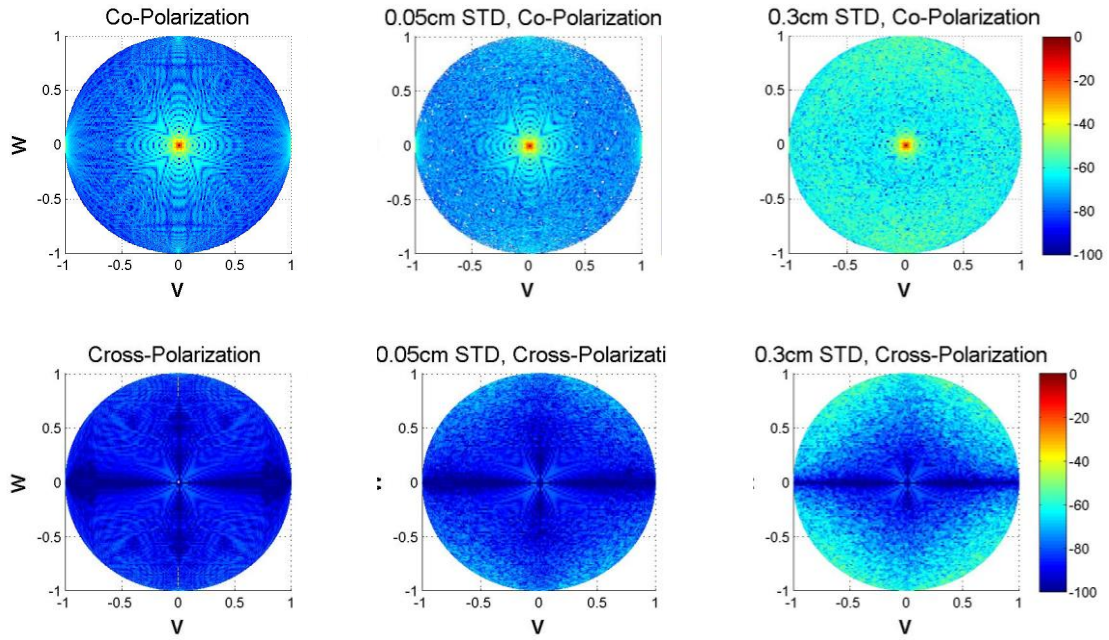


**Figure 4-9** Mechanical positioning errors. Copolar and cross-polar patterns for main beam at broadside. First column are patterns for perfect element location; second column patterns are obtained if 0.0045λ standard derivation is added to each element location; third column results are for adding 0.027λ standard derivation to element locations.

It is a finite probability, however small, that a fault in the hardware or power suppy may cause antenna element to fail. An element failure simulation shows that if randomly selected elements fail, the sidelobes increase. Figure 4-10 shows the array patterns if 1% or 10% of the array elements fail.

A typical phase shifter has a finite number of quantized phase states. The phase quantization introduces undesired quantization beams and affects gain and sidelobe levels. Phase quantization simulations shows that a 6 bit phase shifter does not have much effect of the patterns compared to none quantization patterns. And 6 bit phase shifter meets our needs for weather radar (Figure 4-11).

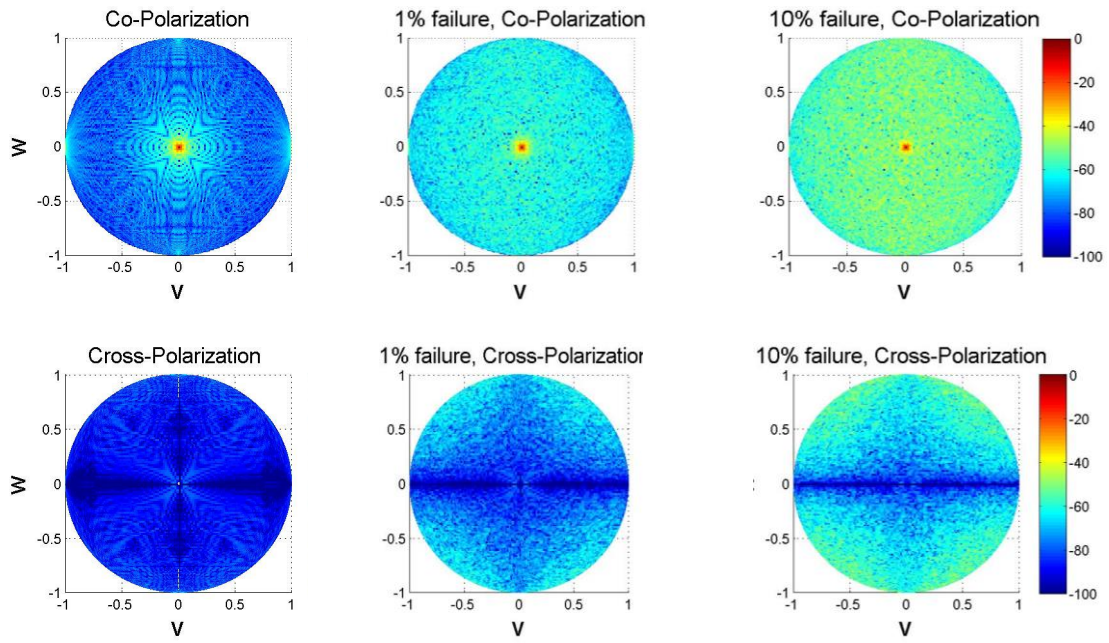


**Figure 4-10** Random element failures. Co-pol and cross-pol patterns for main beam at broadside. First column is no element failure; second column is 1% element failure; third column is 10% element failure.

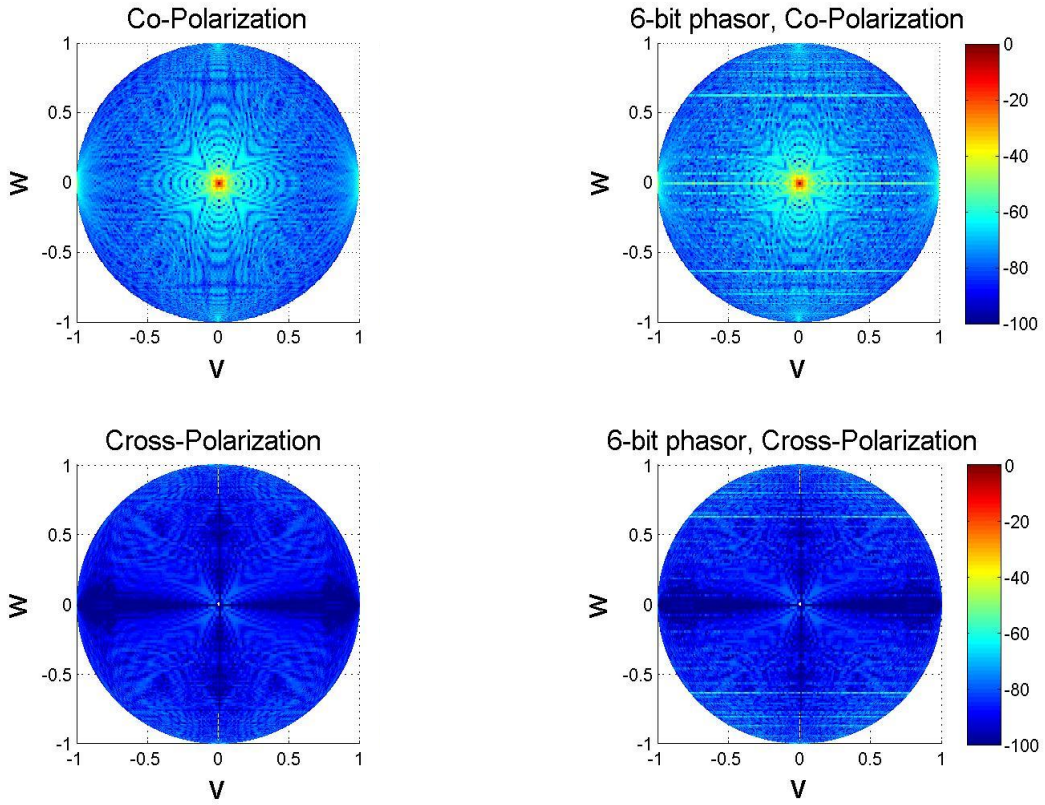


**Figure 4-11** Discretization of phase. Copolar and cross-polar patterns for main beam at broadside. First column is no quantization; second column is using 6-bit phasor.

# Chapter 5 Multi-faced PPAR

In the previous chapter, we present the advantages of the Cylindrical Polarimetric Phased Array Radar (CPPAR) over those of the Planar Polarimetric Phased Array Radar (PPPAR) for weather applications. However, due to the manufacturing complexity of the CPPAR, multi-faced PPAR is introduced to find the design trade-offs (Figure 5-1).

The CPPAR's beam direction is always in the vertical plane bisecting the active sector, and azimuth scans are obtained by commuting the array excitation column by column. Similar to the multi-faced PPAR, the beam direction is always in the vertical plane bisecting the active sector although the active section is not always exactly symmetric in azimuth any more. This slight asymmetry of the active section causes increases in biases of polarimetric radar parameters. The performance of multi faced PPAR lies between that of CPPAR and PPPAR as will be shown.

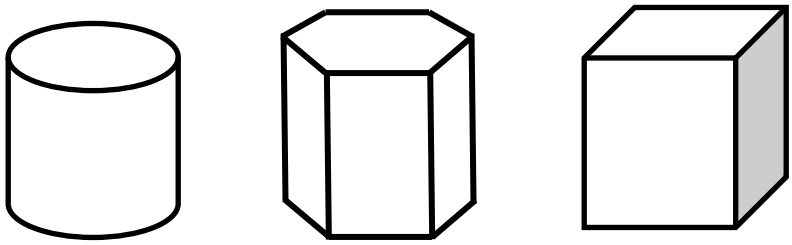

**Figure 5-1** Cylindrical, multi-faced, and four-face planar PPAR

In this chapter, we calculate polarimetric radar parameter biases of multi-phased PPAR. The size of multi-faced PPAR is chosen as 5 meters in diameter and 3.53 meters in height, with 0.5 $\lambda$ element separations for all cases. A 90 degree active sector is

always used (i.e. 4 sectors). For 12 columns per face of the multi-faced PPAR, the radian corresponding to each face is 15° as shown in Figure 5-2a; for 8 columns per face, the radian corresponding to each face is 10° as shown in Figure 5-2b; and for 4 columns per face, the radian corresponding to each face is 5.07° as shown in Figure 5-2c. By running simulations, we found that the radiation patterns from multi-faced PPAR are not exactly azimthally symmetric any more, as in those of CPPAR.

By using the general formulas from (2-20) to (2-27) and (2-32) to (2-39) in the last section of Chapter 2, we integrate the radiation patterns to calculate the biases of $Z_{DR}$ and $\rho_{hv}$. Figure 5-3, Figure 5-4, and Figure 5-5 are the results of the $Z_{DR}$ and $\rho_{hv}$ biases for 12 columns per face, 8 columns per face, and 4 columns per face multi-faced PPAR respectively. In these figures, 7.5°, 5°, and 2.5° are the azimuth limits for these three structures respectively because the biases period vary in azimuth. The elevation angle is chosen as 20 degree and the ideal dipole is used as the antenna element.

The variation of $Z_{DR}$ bias in azimuth is about 0.04 dB for 12 columns per face and 0.02 dB for 8 columns per face and nearly zero dB for 4 columns per face. The bias variations are small and tolerable for weather observations.

In order to compare with multi-faced PPAR, the biases for CPPAR are also calculated using the same parameters of multi-faced PPAR. For the similarly sized CPPAR (i.e. the 5 meters diameter and 3.53 meters in height), the biases are fixed

values at -0.169 dB for $Z_{DR}$ in STSR mode, -0.164 dB for $Z_{DR}$ in ATSR mode, -0.0009 for $\rho_{hv}$ in STSR mode, and -0.0015 for $\rho_{hv}$ in ATSR mode.

The results of 4 columns per face multi-faced PPAR approach the results of CPPAR. The average $Z_{DR}$ biases of 8 columns per face multi-faced PPAR increase about 0.03 dB compared with CPPAR and average $Z_{DR}$ biases of 12 columns per face multi-faced PPAR increase about 0.06 dB compared with CPPAR. Therefore, the more columns on one face of a multi-faced PPAR, the larger the $Z_{DR}$ biases.

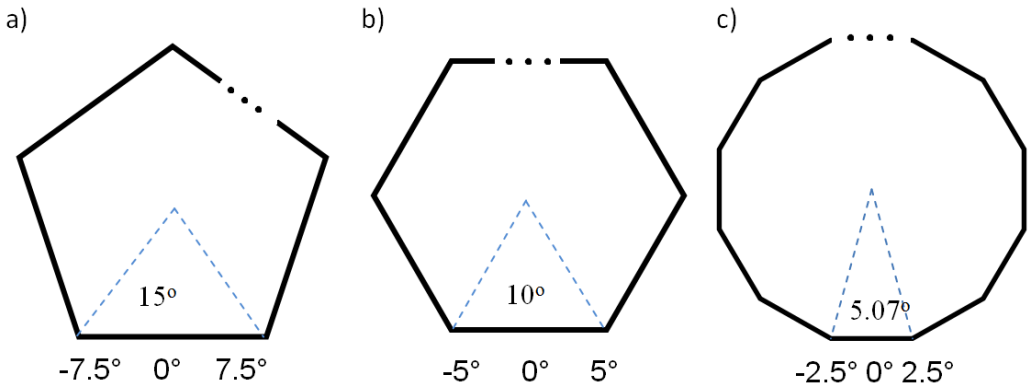


Figure 5-2 top view of multi-faced PPAR: a) 12, columns per face, b) 8 columns per face, and c) 4 columns per face.

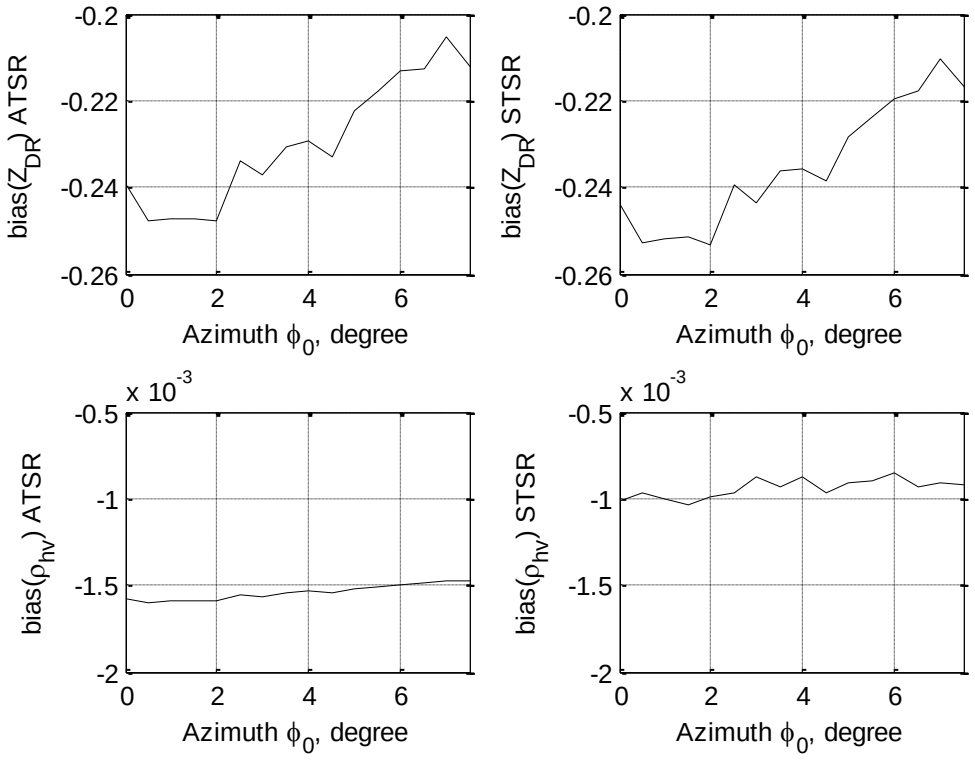


**Figure 5-3** $Z_{DR}$ and $\rho_{hv}$ biases for 12 columns per face multi-faced PPAR, $\theta_0 = 70^0$, $\rho_{\mathrm{hv}} = 0.9$, $Z_{DR} = 1dB$, ideal dipole element. Top row: $Z_{DR}$ biases in dB for the ATSR and STSR modes. Bottom row: $\rho_{hv}$ biases for the ATSR and STSR modes.

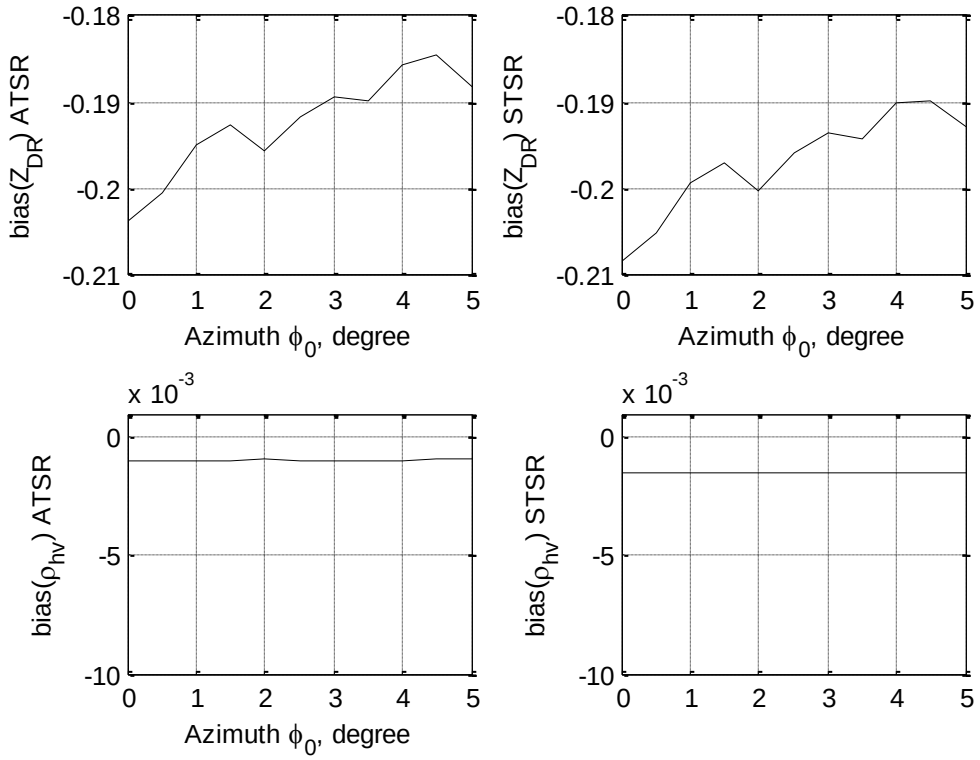


Figure 5-4 $Z_{DR}$ and $\rho_{hv}$ biases for 8 columns per face multi-faced PPAR, $\theta_0 = 70^0$, $\rho_{\mathrm{hv}} = 0.9$, $Z_{DR} = 1dB$, ideal dipole element. Top row: $Z_{DR}$ biases in dB for the ATSR and STSR modes. Bottom row: $\rho_{hv}$ biases for the ATSR and STSR modes.

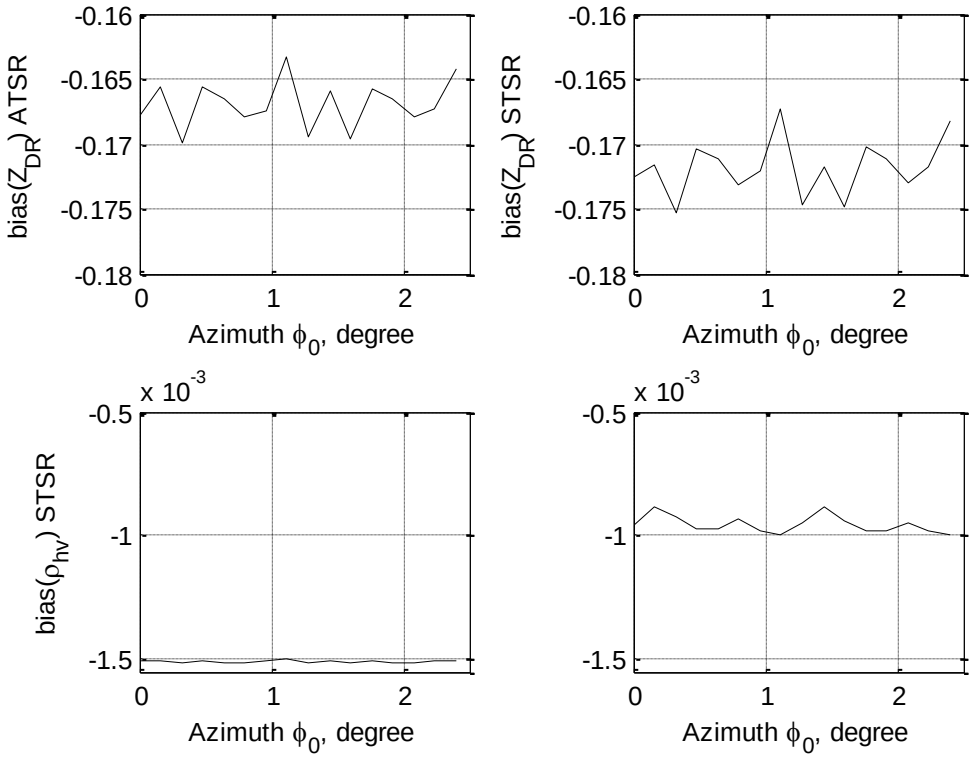


**Figure 5-5** $Z_{DR}$ and $\rho_{hv}$ biases for 4 columns per face multi-faced PPAR, $\theta_0 = 70^0$, $\rho_{\mathrm{hv}} = 0.9$, $Z_{DR} = 1dB$, ideal dipole element. Top row: $Z_{DR}$ biases in dB for the ATSR and STSR modes. Bottom row: $\rho_{hv}$ biases for the ATSR and STSR modes.

# Chapter 6 Conclusions and future work

Planar or Cylindrical Polarimetric Phased Arrays are studied for weather radar applications. The copolar and cross-polar radiation patterns and polarimetric parameter estimation performances of Planar and Cylindrical Polarimetric Phased Array Radar are studied and compared with those obtained using a dual polarized parabolic reflector antenna (WSR-88D). At broadside, all three antennas have cross-polar patterns of 4 peaks alternating phase symmetrically located about the copolar beam. PPPAR radiation pattern evolves into 1 cross-polar pattern mainlobe co-axial with the copolar mainlobe, which is the most effective in creating polarimetric polarimetric parameter estimate bias as the beam scans away from principle planes. It is found that the cross-pol field along boresight of CPPAR is much less than that of PPAR. The general formulas to calculate the biases of polarimetric radar parameters for any kind of antenna for both ATSR and STSR mode are given in chapter 2.

Planar Polarimetric Phased Array Radar (i.e., PPPAR) creates biases in observed polarimetric parameters when the beam is pointed off broadside. The biases of polarimetric parameters with a PPPAR are presented, and they are unacceptably large. Thus, a bias correction matrix needs to be applied for each beam direction. The biases expected in PPAR measured polarimetric parameters such as $Z_{DR}$, $\rho_{\mathrm{hv}}$ and LDR, are functions of the element's radiation pattern, beam direction, the copolar correlation coefficient, the reflectivity field, and the array factor. A bias correction matrix is developed to correct biases in polarimetric parameters for array elements consisting of either dipole, waveguide apertures or patches. If the element's far field radiation pattern

is known (either from a theoretical formula or measurement), the projection matrix can be found from which a correction matrix can be derived to mitigate biases. The theoretical projection matrices for aperture and patch elements are derived, and it is shown they are nearly complementary to the projection matrix for crossed dipoles. Correction matrices are given for both the Alternate Transmission and Simultaneous Reception mode and the Simultaneous Transmission and Simultaneous Reception mode. It is shown that by using a patch size to obtain the same patterns for horizontally and vertically polarized fields, the bias of $Z_{DR}$ is almost zero between elevation 0° to 15° for both ATSR and STSR modes. This is an important property that can be utilized in antenna design for PPAR so that polarization correction is minimal or no needed at all as with the WSR-88D. For PPPAR, we also compare the biases from the boresight contributions and those biases calculated when the entire radiation patterns are integrated and find that they are almost the same. Therefore, boresight contribution is a good approximation of the integration results.

The PPPAR, however, has significant deficiencies for polarimetric measurements, as well as other limitations, such as increases in beamwidth, decreases in sensitivity, and high geometrically projected cross-polar fields when the beam scans away from the array's broadside direction. The Cylindrical Polarimetric Phased Array Radar (i.e., CPPAR) is proposed to avoid these deficiencies. It is shown that the CPPAR has much lower geometrically induced cross-polar fields and smaller bias of polarimetric parameters than those of PPPAR. Biases in estimation of polarimetric variables including differential reflectivity, correlation coefficient, and differential

phase are derived for both STSR and ATSR modes. The biases are calculated by integration of the field in all directions assuming uniform reflectivity. Comparing CPPAR, PPPAR and WSR-88D, it is found that biases of CPPAR are much less than those of PPPAR and biases of CPPAR are approaching the biases of WSR-88D. After gain adjustment in H and V, the $Z_{DR}$ biases for PPAR reduce greatly. And $Z_{DR}$ biases for CPPAR and WSR-88D are nearly zero after simple adjustments to the voltages applied to the H and V ports to account for the gain difference. Then, the CPPAR principle and potential performance are demonstrated through theoretical analysis and simulation. The element separation and grating lobes, element lattice and error effects are studied. The horizontally staggered triangular lattice can save 8% array elements than rectangular lattice but requires many circuit board crossovers.

Multi-faced PPAR is introduced and discussed. And the polarimetric radar parameters biases are calculated by running simulations of pattern integration. It is found that the variations of $Z_{DR}$ and $\rho_{\mathrm{hv}}$ is within tolerance for weather applications if several columns are placed on one face for a 5m diameter multi-faced PPAR.

Future work should employ a more types of antenna elements such as aperture coupled patch element that have more symmetric patterns and are less affected by the higher order mode of the feed lines. In addition, because it is difficult to isolate the H and V polarized waves if they co-exist in each element aperture, the layout and shape of pairs of H and V polarized apertures in an array needs to be considered to minimize

coupling. Coupling between array elements and feed lines is another issue that needs to be examined.

## References

ANSYS. *( available online at http://www.ansys.com/Products/Simulation+Technology/Electromagnetics/Signal+Integrity/ANSYS+HFSS).*

Balanis, C. A., 1997: *Antenna theory : analysis and design.* 2nd ed. Wiley, 941 p.

Baron, 2009: 2009 WSR-88D Dual-Polarization Program, Report: Antenna Component Test. *Baron Services, Inc. 4930 Research Park Drive, Huntsville, AL, 35805*.

Bhardwaj, S., and Y. Rahmat-Samii, 2014: Revisiting the generation of cross-polarization in rectangular patch antennas: A near-field approach. *Antennas and Propagation Magazine, IEEE*, **56,** 14-38.

Brandes, E. A., G. Zhang, and J. Vivekanandan, 2002: Experiments in Rainfall Estimation with a Polarimetric Radar in a Subtropical Environment. *Journal of Applied Meteorology*, **41,** 674-685.

Bringi, V. N., and V. Chandrasekar, 2001: *Polarimetric Doppler weather radar : principles and applications.* Cambridge University Press, 636 p.

Bringi, V. N., and Coauthors, 2011: Design and Performance Characteristics of the New 8.5-m Dual-Offset Gregorian Antenna for the CSU–CHILL Radar. *Journal of Atmospheric and Oceanic Technology*, **28,** 907-920.

Crain, G. E., and D. Staiman, 2007: Polarization selection for phased array weather radar. *presented at the Proc. AMS Annu. Meeting: 23rd Conf. IIPS, San Antonio, TX, Jan. 2007***,** Paper 7.7.

Darcy, S. S., 2012: New science for the WSR-88D: status of the dual polarization updates. *92nd AMS annual meeting, IIPS, New Orleans, LA*.

Dawson II, D. T., L. J. Wicker, E. R. Mansell, and R. L. Tanamachi, 2012: Impact of the Environmental Low-Level Wind Profile on Ensemble Forecasts of the 4 May 2007 Greensburg, Kansas, Tornadic Storm and Associated Mesocyclones. *Monthly Weather Review*, **140,** 696-716.

Doviak, R., D. S. Zrnić, J. Carter, A. Ryzhkov, S. Torres, and A. Zahrai, 1998: WSR-88D Radar for Research and Enhancement of Operations: Polarimetric Upgrades to Improve Rainfall Measurements. *NOAA/NSSL report*, *http://www.nssl.noaa.gov/publications/mpar_reports/***,** 110.

Doviak, R. J., and D. a. S. Zrnić, 2006: *Doppler radar and weather observations*. 2nd ed. Academic Press, xix, 562 p. pp.

Doviak, R. J., L. Lei, Z. Guifu, J. Meier, and C. Curtis, 2011: Comparing Theory and Measurements of Cross-Polar Fields of a Phased-Array Weather Radar. *Geoscience and Remote Sensing Letters, IEEE*, **8,** 1002-1006.

FAA, 2013: NextGen Surveillance and Weather Radar Capability**,** Federal Aviation Administration, 16.

Fradin, A. Z., 1961: Microwave Antennas. *Pergamon Press***,** 668.

Fulton, C., and W. J. Chappell, 2010: Calibration of a digital phased array for polarimetric radar. *Microwave Symposium Digest (MTT), 2010 IEEE MTT-S International*, 161-164.

Galletti, M., and D. S. Zrnić, 2011: Bias in Copolar Correlation Coefficient Caused by Antenna Radiation Patterns. *Geoscience and Remote Sensing, IEEE Transactions on*, **49,** 2274-2280.

Hansen, R. C., 2009: *Phased array antennas.* 2nd ed. Wiley, 547 p.

Jones, E. M. T., 1954: Paraboloid reflector and hyperboloid lens antennas. *Antennas and Propagation, Transactions of the IRE Professional Group on*, **2,** 119-127.

Josefsson, L., and P. Persson, 2006: Conformal array antenna theory and design. *IEEE Press series on electromagnetic wave theory*, IEEE Press, Wiley-Interscience.

Kraus, J. D., J. D. Kraus, and R. J. Marhefka, 2002: *Antennas for all applications.* 3rd ed. McGraw-Hill, 938 p.

Lei, L., Z. Guifu, and R. J. Doviak, 2012: Theoretical Analysis of Polarization Characteristics for Planar and Cylindrical Phased Array Radars. *AMS annual meeting, 28th conference on Interactive Information Processing Systems (IIPS), New Orleans, LA, Jan. 22-26*.

Lei, L., Z. Guifu, and R. J. Doviak, 2013: Bias Correction for Polarimetric Phased-Array Radar With Idealized Aperture and Patch Antenna Elements. *Geoscience and Remote Sensing, IEEE Transactions on*, **51,** 473-486.

Liu, H., and V. Chandrasekar, 2000: Classification of Hydrometeors Based on Polarimetric Radar Measurements: Development of Fuzzy Logic and Neuro-Fuzzy Systems, and In Situ Verification. *Journal of Atmospheric and Oceanic Technology*, **17,** 140-164.

Ludwig, A., 1973: The definition of cross polarization. *Antennas and Propagation, IEEE Transactions on*, **21,** 116-119.

Paramax, 1992: Test Report, Antenna/Pedestal, Part 1 of 4, Linear Polarized Antenna First Article. *prepared for :U.S. Department of Commerce, Office of Procurement, Washington, DC 20230*.

Park, H. S., A. V. Ryzhkov, D. S. Zrnić, and K.-E. Kim, 2009: The Hydrometeor Classification Algorithm for the Polarimetric WSR-88D: Description and Application to an MCS. *Weather and Forecasting*, **24,** 730-748.

Perera, S., Y. Pan, Y. Zhang, X. Yu, D. Zrnić, and R. J. Doviak, 2014: A fully reconfigurable polarimetic phased array antenna testbed. *International Journal of antennas and propagation*.

Ryzhkov, A. V., S. E. Giangrande, and T. J. Schuur, 2005: Rainfall Estimation with a Polarimetric Prototype of WSR-88D. *Journal of Applied Meteorology*, **44,** 502-515.

Sherman, J. W., and M. I. Skolnik, 1970: Radar Handbook, *McGraw Hill*, Aperture-antenna analysis, Chap. 9.

Sikina, T. V., and K. D. Trott, 2010: Polarization isolation limit for dual-polarized phased array systems. *Phased Array Systems and Technology (ARRAY), 2010 IEEE International Symposium on*, 796-800.

Smith, P., and Coauthors, 2008: Evaluation of the Multifunction Phased Array Radar Planning Process. *National Research Council Report*.

Staiman, D., 2009: Calibration of polarimetric phased array radar for improved measurement accuracy,. *Proc. AMS Annu. Meeting: 25th Conf. IIPS*, Paper 9B.2.

Steiner, M., and J. A. Smith, 2002: Use of Three-Dimensional Reflectivity Structure for Automated Detection and Removal of Nonprecipitating Echoes in Radar Data. *Journal of Atmospheric and Oceanic Technology*, **19,** 673-686.

Urkowitz, H., 2006: Radar receiver correction polarization. *Proc. AMS Annu. Meeting: 22nd Conf. IIPS*, Paper 11.8.

Vivekanandan, J., S. M. Ellis, R. Oye, D. S. Zrnić, A. V. Ryzhkov, and J. Straka, 1999: Cloud Microphysics Retrieval Using S-band Dual-Polarization Radar Measurements. *Bulletin of the American Meteorological Society,* **80,** 381-388.

Weadon, M., P. Heinselman, D. Forsyth, J. Kimpel, W. E. Benner, and G. S. Torok, 2009: Multifunction Phased Array Radar. *Bulletin of the American Meteorological Society,* **90,** 385-389.

Weber, M. E., J. Y. N. Cho, J. S. Herd, J. M. Flavin, W. E. Benner, and G. S. Torok, 2007: The Next-Generation Multimission U.S. Surveillance Radar Network. *Bulletin of the American Meteorological Society*, **88,** 1739-1751.

Wurman, J., and M. Randall, 2001: An inexpensive, mobile, rapid-scan radar. *30th International Conference on Radar Meteorology*, P3.4.

Yussouf, N., E. R. Mansell, L. J. Wicker, D. M. Wheatley, and D. J. Stensrud, 2013: The Ensemble Kalman Filter Analyses and Forecasts of the 8 May 2003 Oklahoma City Tornadic Supercell Storm Using Single- and Double-Moment Microphysics Schemes. *Monthly Weather Review*, **141,** 3388-3412.

Zhang, G., J. Vivekanandan, and E. Brandes, 2001: A method for estimating rain rate and drop size distribution from polarimetric radar measurements. *Geoscience and Remote Sensing, IEEE Transactions on*, **39,** 830-841.

Zhang, G., R. J. Doviak, D. S. Zrnic, J. Crain, D. Staiman, and Y. Al-Rashid, 2009: Phased Array Radar Polarimetry for Weather Sensing: A Theoretical Formulation for Bias Corrections. *Geoscience and Remote Sensing, IEEE Transactions on*, **47,** 3679-3689.

Zhang, G., R. J. Doviak, D. S. Zrnić, R. Palmer, L. Lei, and Y. Al-Rashid, 2011: Polarimetric Phased-Array Radar for Weather Measurement: A Planar or Cylindrical Configuration? *Journal of Atmospheric and Oceanic Technology,* **28,** 63-73.

Zrnić, D. a. S., A. Ryzhkov, J. Straka, Y. Liu, and J. Vivekanandan, 2001: Testing a Procedure for Automatic Classification of Hydrometeor Types. *Journal of Atmospheric and Oceanic Technology*, **18,** 892-913.

Zrnić, D. S., Z. Guifu, and R. J. Doviak, 2011: Bias Correction and Doppler Measurement for Polarimetric Phased-Array Radar. *Geoscience and Remote Sensing, IEEE Transactions on*, **49,** 843-853.

Zrnić, D. S., R. J. Doviak, and V. M. Melnikov, 2012: Issues and Challenges for polarimetric measurement of weather with an agile beam phased array radar. *NOAA/NSSL report, http://www.nssl.noaa.gov/publications/mpar_reports/*, 117.

Zrnić, D. S., R. J. Doviak, G. Zhang, and A. Ryzhkov, 2010: Bias in Differential Reflectivity due to Cross Coupling through the Radiation Patterns of Polarimetric Weather Radars. *Journal of Atmospheric and Oceanic Technology*, **27,** 1624-1637.

Zrnić, D. S., V. M. Melnikov, R. J. Doviak, and R. Palmer, 2013: Scanning and Waveform for the Multifunction Phased Array Radar to Satisfy Aviation and Meteorological Needs. *IEEE Internatioal Symposium on Phased Array Systems & Technology, Revolutionary Developments in Phased Arrays***,** 4.

Zrnić, D. S., and Coauthors, 2007: Agile-Beam Phased Array Radar for Weather Observations. *Bulletin of the American Meteorological Society*, **88,** 1753-1766.

# APPENDIX A:
# Analytically derived radiation patterns for Aperture and Patch

### Aperture: $TE_{10}$ - Mode Distribution

Let's consider a rectangular aperture in an infinite ground plane, wherein the aperture is energized with a $TE_{10}$ wave propagating in a uniform waveguide. If the aperture has a vertical polarized wave (Balanis 1997, chapter 12: aperture antenna)

$$E_{\mathrm{a}} = \hat{a}_{\mathrm{z}} E_{\mathrm{o}} \cos(\frac{\pi}{a} y) \qquad \begin{cases} -a/2 < y < a/2 \\ -b/2 < z < b/2 \end{cases} \tag{A1}$$

By equivalence principle, the equivalent sources are

$$\begin{cases} M_{\mathrm{s}} = -2\hat{n} \times E_{\mathrm{a}} = 2\hat{a}_{\mathrm{y}} E_{\mathrm{o}} \cos(\frac{\pi}{a} y) \\ J_{\mathrm{s}} = 0 \end{cases} \tag{A2}$$

Then, $L_\theta$, $L_\phi$ are related to the electric vector potential and are defined by Balanis (1997, Eqn. (12.7)), whereas $Q_\theta$ and $Q_\phi$ are related to the magnetic vector potential and are also defined by Balanis (1997, Eqn. (12.6)); $Q$ replaces $N$ in this dissertation).

$L_\theta$, $L_\phi$, $Q_\theta$ and $Q_\phi$ can be obtained from (12.12) in Balanis (1997)

$$
\begin{aligned}
L_\theta &= \iint_s M_y \cos\theta \sin\phi e^{jkr'\cos\psi} ds' \\
&= \iint_s M_y \cos\theta \sin\phi e^{jk(y\sin\theta\sin\phi + z\cos\theta)} ds' \\
&= 2E_o \cos\theta \sin\phi \int_{-\frac{a}{2}}^{\frac{a}{2}} \cos(\frac{\pi}{a} y) e^{jky\sin\theta\sin\phi} dy \int_{-\frac{b}{2}}^{\frac{b}{2}} e^{jkz\cos\theta} dz \\
&= 2E_o \cos\theta \sin\phi \cdot \frac{0.5\pi a \cos X_1}{(0.5\pi)^2 - X_1^2} \cdot \frac{b \sin Y_1}{Y_1} \\
&= \pi abE_o \cos\theta \sin\phi \cdot \frac{\cos X_1}{(0.5\pi)^2 - X_1^2} \cdot \frac{\sin Y_1}{Y_1}
\end{aligned}
\tag{A3}
$$

where, $X_1 = \frac{k_0 a}{2} \sin\theta \sin\phi, Y_1 = \frac{k_0 b}{2} \cos\theta$

$$
\begin{aligned}
L_\phi &= \iint_s M_y \cos\phi e^{jk_0 r'\cos\psi} ds' \\
&= \iint_s M_y \cos\phi e^{jk_0(y\sin\theta\sin\phi + z\cos\theta)} ds' \\
&= 2E_o \cos\phi \int_{-\frac{a}{2}}^{\frac{a}{2}} \cos(\frac{\pi}{a} y) e^{jk_0 y\sin\theta\sin\phi} dy \int_{-\frac{b}{2}}^{\frac{b}{2}} e^{jk_0 z\cos\theta} dz \\
&= 2E_o \cos\phi \cdot \frac{0.5\pi a \cos X_1}{(0.5\pi)^2 - X_1^2} \cdot \frac{b \sin Y_1}{Y_1} \\
&= \pi abE_o \cos\phi \cdot \frac{\cos X_1}{(0.5\pi)^2 - X_1^2} \cdot \frac{\sin Y_1}{Y_1}
\end{aligned}
\tag{A4}
$$

$$
Q_\theta = 0 \tag{A5}
$$

$$
Q_\phi = 0 \tag{A6}
$$

After the $L_\theta$ , $L_\phi$ , $Q_\theta$ and $Q_\phi$ are obtained, the far fields of a vertical polarized rectangular aperture can be calculated by substituting Eqn. (A3) to Eqn.(A6) into (12.10) in Balanis (1997) to obtain the electrical fields of a vertically polarized aperture. That is

$$E_\theta \simeq -\frac{jk_0 e^{-jk_0 r}}{4\pi r}(L_\phi + \eta Q_\theta)$$
$$= -\frac{jk_0 e^{-jk_0 r}}{4r} abE_o \cos\phi \cdot \frac{\cos X_1}{(0.5\pi)^2 - X_1^2} \cdot \frac{\sin Y_1}{Y_1} \tag{A7}$$

and

$$E_\phi \simeq \frac{jk_0 e^{-jk_0 r}}{4\pi r}(L_\theta - \eta Q_\phi)$$
$$= \frac{jk_0 e^{-jk_0 r}}{4r} abE_o \cos\theta \sin\phi \cdot \frac{\cos X_1}{(0.5\pi)^2 - X_1^2} \cdot \frac{\sin Y_1}{Y_1} \tag{A8}$$

In the above equations, $E_\theta$ (i.e., V, the so-called vertically polarized field) is the copolar radiation field, and $E_\phi$ (i.e., H, is the cross-polar field).

Likewise the electric field of a horizontally polarized aperture can be calculated. At the aperture surface, we have

$$E_a = \hat{a}_y E_o \cos(\frac{\pi}{a} z) \text{ , where } \quad \begin{cases} -b/2 < y < b/2 \\ -a/2 < z < a/2 \end{cases} \tag{A9}$$

The equivalent magnetic current sources are

$$\begin{cases} M_s = -2\hat{n} \times E_a = 2\hat{a}_z E_o \cos(\frac{\pi}{a} z), \\ J_s = 0. \end{cases} \tag{A10}$$

Then, $L_\theta$, $L_\phi$, $Q_\theta$ and $Q_\phi$ can be obtained

$$
\begin{aligned}
L_\theta &= \iint_s -M_z \sin\theta e^{jk_0 r'\cos\psi} ds' \\
&= \iint_s -M_z \sin\theta e^{jk_0(y\sin\theta\sin\phi + z\cos\theta)} ds' \\
&= 2E_o \sin\theta \int_{-\frac{b}{2}}^{\frac{b}{2}} \cos(\frac{\pi}{a} z) e^{jk_0 z\cos\theta} dz \int_{-\frac{a}{2}}^{\frac{a}{2}} e^{jk_0 y\sin\theta\sin\phi} dy \\
&= 2E_o \sin\theta \cdot \frac{0.5\pi a \cos X_2}{(0.5\pi)^2 - X_2^{\,2}} \cdot \frac{b\sin Y_2}{Y_2} \\
&= \pi abE_o \sin\theta \cdot \frac{\cos X_2}{(0.5\pi)^2 - X_2^{\,2}} \cdot \frac{\sin Y_2}{Y_2}
\end{aligned}
\tag{A11}
$$

where $X_2 = \frac{k_0 a}{2}\cos\theta, Y_2 = \frac{k_0 b}{2}\sin\theta\sin\phi$, and $L_\phi = Q_\theta = Q_\phi = 0$. Therefore, the electric fields of the horizontally polarized aperture are:

$$
E_\theta \simeq -\frac{jk_0 e^{-jk_0 r}}{4\pi r}(L_\phi + \eta Q_\theta) = 0 \tag{A12}
$$

$$
\begin{aligned}
E_\phi &\simeq \frac{jk_0 e^{-jk_0 r}}{4\pi r}(L_\theta - \eta Q_\phi) \\
&= \frac{jk_0 e^{-jk_0 r}}{4r} abE_o \sin\theta \cdot \frac{\cos X_2}{(0.5\pi)^2 - X_2^{\,2}} \cdot \frac{\sin Y_2}{Y_2},
\end{aligned}
\tag{A13}
$$

where $E_\theta$ and $E_\phi$ are respectively the cross-polar and copolar fields.

**Radiating fields from the radiating slots of an ideal patch antenna**

The radiation fields of an ideal patch come from two sources: radiating and non-radiating slots which will be discussed this subsection and next subsection respectively. The following derivation is limited to patches that have electrically thin substrates. The far field of a horizontally polarized patch can be found from (14-44) in Balanis (1997):

$$E_{\phi}^{(h)} \simeq j\frac{2V_o e^{-jk_o r}}{\pi r}\left\{\sin\theta\frac{\sin(\frac{k_o W}{2}\cos\theta)}{\cos\theta}\right\}\cos(\frac{k_o L_e}{2}\sin\theta\sin\phi) \tag{A14}$$

$$E_{\theta}^{(h)} \simeq 0 \tag{A15}$$

Let's next consider the radiation field from the radiating slots of a vertically polarized patch. A patch is composed by a pair of horizontally oriented radiating slots. So, the pattern of radiation from one slot is calculated first, and then the array factor is added to obtain the final radiation pattern for the pair of slots on opposite sides of the patch. Across each slot the electric field is uniform, that is (Balanis 1997, chapter 12: aperture antenna)

$$E_a = \hat{a}_x E_o \qquad \begin{cases} -a/2 < y < a/2 \\ -b/2 < x < b/2 \end{cases} \tag{A16}$$

And the equivalent sources are

$$\begin{cases} M_s = -2\hat{n}\times E_a = 2\hat{a}_y E_o \\ J_s = 0 \end{cases} \tag{A17}$$

Then, $L_\theta$, $L_\phi$, $Q_\theta$ and $Q_\phi$ can be obtained:

$$\begin{aligned} L_\theta &= \iint_s M_y \cos\theta\sin\phi e^{jk_0 r'\cos\psi} ds' \\ &= \iint_s M_y \cos\theta\sin\phi e^{jk_0(x\sin\theta\cos\phi + y\sin\theta\sin\phi)} ds' \\ &= 2E_o\cos\theta\sin\phi\int_{-\frac{a}{2}}^{\frac{a}{2}} e^{jk_0 y\sin\theta\sin\phi} dy\int_{-\frac{b}{2}}^{\frac{b}{2}} e^{jk_0 x\sin\theta\cos\phi} dx \\ &= 2abE_o\cos\theta\sin\phi\cdot\frac{\sin X_3}{X_3}\cdot\frac{\sin Y_3}{Y_3} \end{aligned} \tag{A18}$$

where, $X_3 = \frac{k_0 b}{2}\sin\theta\cos\phi, Y_3 = \frac{k_0 a}{2}\sin\theta\sin\phi$

$$\begin{aligned} L_\phi &= \iint_s M_y \cos\phi e^{jk_0 r'\cos\psi} ds' \\ &= \iint_s M_y \cos\phi e^{jk_0(x\sin\theta\cos\phi + y\sin\theta\sin\phi)} ds' \\ &= 2abE_o \cos\phi \cdot \frac{\sin X_3}{X_3} \cdot \frac{\sin Y_3}{Y_3} \end{aligned} \tag{A19}$$

$Q_\theta = 0; \quad Q_\phi = 0$

Therefore, the electric field radiated by one slot for a vertically polarized patch (i.e. a horizontal magnetic dipole) is:

$$\begin{aligned} E_\theta &\simeq -j\frac{k_0 e^{-jk_0 r}}{4\pi r}(L_\phi + \eta Q_\theta) \\ &= -j\frac{k_0 e^{-jk_0 r}}{4\pi r} 2abE_o \cos\phi \cdot \frac{\sin X_3}{X_3} \cdot \frac{\sin Y_3}{Y_3} \\ &\simeq -j\frac{k_0 abE_o e^{-jk_0 r}}{2\pi r}\cos\phi \cdot \frac{\sin Y_3}{Y_3} \\ &= -j\frac{V_o e^{-jk_0 r}}{\pi r}\cos\phi \cdot \frac{\sin\frac{k_0 a}{2}\sin\theta\sin\phi}{\sin\theta\sin\phi} \end{aligned} \tag{A20}$$

$$\begin{aligned} E_\phi &\simeq j\frac{k_0 e^{-jk_0 r}}{4\pi r}(L_\theta - \eta Q_\phi) \\ &= j\frac{k_0 e^{-jk_0 r}}{4\pi r} 2abE_o \cos\theta\sin\phi \cdot \frac{\sin X_3}{X_3} \cdot \frac{\sin Y_3}{Y_3} \\ &\simeq j\frac{k_0 e^{-jk_0 r}}{4\pi r} 2abE_o \cos\theta\sin\phi \cdot \frac{\sin Y_3}{Y_3} \\ &= j\frac{V_o e^{-jkr}}{\pi r}\cos\theta\sin\phi \cdot \frac{\sin\frac{k_0 a}{2}\sin\theta\sin\phi}{\sin\theta\sin\phi} \end{aligned} \tag{A21}$$

The array factor for the two slot elements (separated by $L_e$ and both having the same magnitude and phase) of the patch is

$$\left(AF\right)_{\mathrm{z}} = 2\cos\left[0.5(k_0 L_{\mathrm{e}}\cos\theta)\right] \tag{A22}$$

Therefore the electric fields for the patch are

$$E_{\theta} \simeq -j\frac{2V_o e^{-jk_o r}}{\pi r}\left\{\cos\phi\frac{\sin(\frac{k_o W}{2}\sin\theta\sin\phi)}{\sin\theta\sin\phi}\right\}\cos(\frac{k_o L_{\mathrm{e}}}{2}\cos\theta) \tag{A23}$$

$$E_{\phi} \simeq j\frac{2V_o e^{-jk_o r}}{\pi r}\left\{\cos\theta\sin\phi\frac{\sin(\frac{k_o W}{2}\sin\theta\sin\phi)}{\sin\theta\sin\phi}\right\}\cos(\frac{k_o L_{\mathrm{e}}}{2}\cos\theta) \tag{A24}$$

**Radiating fields from the non-radiating slots of an ideal patch antenna**

The fields of non-radiating slots for a horizontally polarized patch are given in Balanis (1997). The radiation fields of non-radiating slots for a vertically polarized patch are derived by applying a coordinate system transformation to the already derived fields from the horizontally polarized patch.

For horizontally polarized patch (i.e. vertical magnetic dipole in the radiating slots), the fields from the non-radiating slots are given by the eqs. 14-48(a) 14-48(b) in Balanis (1997). The normalization factors $\frac{k_o h L_e E_o e^{-jk_o r}}{2\pi r}$ are taken out and the fields are

$$E_r \simeq 0 \tag{A25}$$

$$E_{\theta} \simeq -\left\{ Y\cos\phi \frac{\sin X}{X} \frac{\cos Y}{Y^2 - \left(\frac{\pi}{2}\right)^2} \right\} e^{j(X+Y)} \tag{A26}$$

$$E_{\phi} \simeq \left\{ Y\cos\theta\sin\phi \frac{\sin X}{X} \frac{\cos Y}{Y^2 - \left(\frac{\pi}{2}\right)^2} \right\} e^{j(X+Y)} \tag{A27}$$

Where

$$\begin{cases} X = \frac{k_o h}{2}\sin\theta\cos\phi \\ Y = \frac{k_o L_e}{2}\sin\theta\sin\phi \end{cases} \tag{A28}$$

Transformation from $E_r$, $E_{\theta}$, and $E_{\phi}$ to $E_x, E_y$ and $E_z$, we have

$$E_x = -\cos\theta \cdot Y \cdot \frac{\sin X}{X} \cdot \frac{\cos Y}{Y^2 - \left(\frac{\pi}{2}\right)^2} e^{j(X+Y)} \tag{A29}$$

$$E_y = 0 \tag{A30}$$

$$E_z = \cos\theta\sin\phi Y \frac{\sin X}{X} \frac{\cos Y}{Y^2 - \left(\frac{\pi}{2}\right)^2} e^{j(X+Y)} \tag{A31}$$

In order to obtain the fields from the non-radiating slots of a vertically polarized patch we need transformation from $x, y, z$ to $x', y', z'$ coordinate systems as shown below

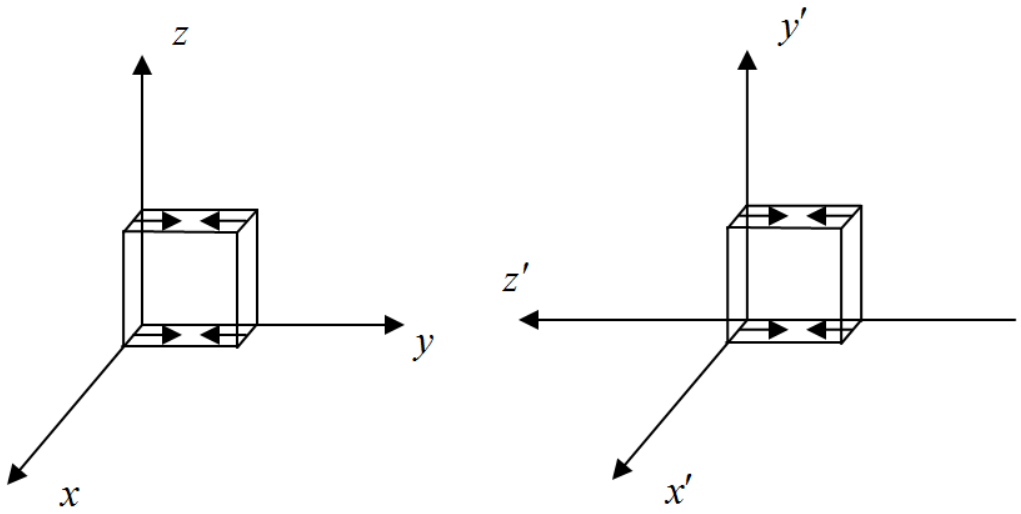


**Figure A:** xyz to $x'\ y'\ z'$ coordinates: transform horizontally polarized patch (left) to vertically polarized patch (right; only moments from non-radiating slots are shown).

From Figure A, we have

$$\begin{cases} x' = x \\ z' = -y \\ y' = z \end{cases} \tag{A32}$$

And therefore,

$$\begin{cases} \sin\theta'\cos\phi' = \sin\theta\cos\phi \\ \cos\theta' = -\sin\theta\sin\phi \\ \sin\theta'\sin\phi' = \cos\theta \end{cases} \tag{A33}$$

Eqn. (A32) yields

$$\begin{cases} E_{x'} = E_x \\ E_{z'} = -E_y \\ E_{y'} = E_z \end{cases} \tag{A34}$$

and Eqn. (A33) can be recalculated as

$$\begin{cases} \cos\theta' = -\sin\theta\sin\phi \\ \sin\theta' = \sqrt{\cos^2\theta + \sin^2\theta\cos^2\phi} \\ \cos\phi' = \dfrac{\sin\theta\cos\phi}{\sin\theta'} \\ \sin\phi' = \dfrac{\cos\theta}{\sin\theta'} \end{cases} \tag{A35}$$

Using eqs. (A29), (A30), (A31), (A34), and (A35), coordinate system transformation from $E_x$, $E_y$, and $E_z$ to $E_{r'}$, $E_{\theta'}$, and $E_{\phi'}$ are:

$$E_{r'} = 0 \tag{A36}$$

$$E_{\theta'} = 0 \tag{A37}$$

$$E_{\phi'} = \sin\theta' \cdot Y \cdot \frac{\sin X}{X} \cdot \frac{\cos Y}{Y^2 - \left(\frac{\pi}{2}\right)^2} e^{j(X+Y)} \tag{A38}$$

Where

$$\begin{cases} X = \dfrac{k_0 h}{2}\sin\theta'\cos\phi' \\ Y = -\dfrac{k_0 L_e}{2}\cos\theta' \end{cases} \tag{A39}$$

Therefore, eqs. (A36) to (A39) are the electrical fields for non-radiating slots generated from vertically polarized patch.

And the corresponding array factor for the pair of non-radiating slots generated from vertically polarized patch is

$$AF_y = 2i\sin\left(\frac{k_0 W}{2}\sin\theta'\sin\phi'\right) \tag{A40}$$

## APPENDIX B:

## Theoretical far field copolar and cross-polar radiation patterns for the WSR-88D

Analytical solutions for the copolar electric field radiated by a circularly symmetric aperture distribution can be obtained from equations given by Sherman and Skolnik (1970). Applying these equations and normalizing, we obtain the theoretical pattern of copolar power density $S(u) = F_{vv}^2(u) / g_{vv}$

$$S(u) = 20\ \mathrm{Log}_{10}\left[ 5.405 \left| 1.68 \frac{4!\, J_4(u)}{u^4} + 0.16 \frac{J_1(u)}{u} \right| \right] \qquad \text{(B1)}$$

where

$$u = \frac{2\pi\rho_{\mathbf{o}} \sin\theta'}{\lambda}, \quad 2\rho_{\mathbf{o}} = 8.534, \ \lambda(\mathrm{KOUN}) = 0.1109\,\mathrm{m}, \qquad \text{(B2)}$$

and $\theta', \phi'$ are the polar and azimuth angles in the spherical coordinate system with the polar axis along the beam—because of symmetry there is no $\phi'$ dependence for $F_{vv}$.

Unfortunately there is no analytical solution for the cross-polar $F_{hv}$ of an axially symmetric aperture distribution. Thus we use Jones's (1954) theoretical formulas of the cross-polar far field of a reflector illuminated by a Hertzian dipole field to calculate the approximate angular distribution of cross-polar lobes, but the dipole's aperture field distribution is multiplied by (B1) to account for the feed horn pattern weighting. Note the $TE_{11}$ distribution of the WSR-88D horn's radiation pattern partially cancels the cross-polar field generated by the reflector (Fradin 1961). Thus we cannot use the

magnitude of the cross-polar field as calculated by Jones (1954) to estimate the peak intensity of the cross-polar field. Cross-polar measurements are used to scale the theoretical cross-polar radiation patterns computed from Jones' formulas.

The integral for the far field cross-polar radiation field is given by Jones (1954, Eqn. (22)), and when $W(\rho)$ from (B1) is introduced this equation becomes

$$E_x = A\int_0^{\gamma} W(u)\frac{u^3 J_2(\beta u)\sin(2\phi')}{(1+u^2)^2}du \qquad \text{(B3)}$$

where $E_x$ is the cross-polar radiation in the far field, $A$ is a normalizing constant, $u = \rho / 2f$, f = 3.2 m is the focal length of KOUN's parabolic reflector, $\beta = 2kf\sin\theta'$ where $k = 2\pi/\lambda$, and $J_2$ is the Bessel function of the first kind of order 2. The azimuth angle $\phi'$ around the beam axis is referenced to the dipole's axis. This theoretical WSR-88D cross-polar pattern is plotted in Figure 2-8 and Figure 2-11 and is the one used to compute the polarimetric parameter biases for the WSR-88D. Also plotted for comparison in Figure 2-11c is the cross-polar pattern measured by Seavey Engineering on their antenna range in Massachusetts (Baron 2009).

## APPENDIX C:

## Angle transformation from spherical coodinates $(r,\theta',\phi')$ of the dish antenna to the $(r,\theta,\phi)$ coordinates of Figure 2-1.

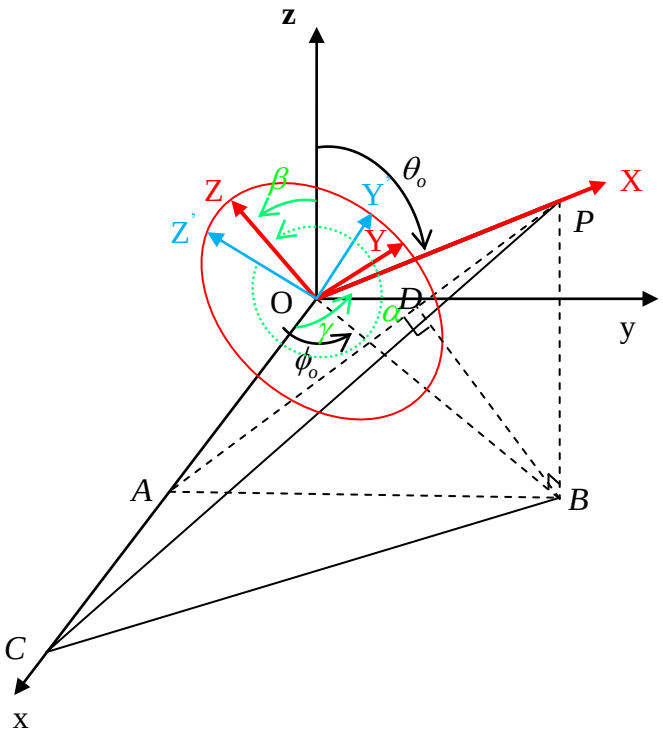


**Figure C** The spherical coordinates $(r,\theta,\phi)$ of Fig.1, and the spherical coordinates $(r,\theta',\phi')$ with polar axis along the dish antenna's beam axis $X = r$.

XYZ is the dish antenna coordinate system and the beam axis is along the X axis.

$(X,Y,Z)$ and $(r,\theta',\phi')$ are related by $\begin{bmatrix} X \\ Y \\ Z \end{bmatrix} = \begin{bmatrix} r\sin\theta'\cos\phi' \\ r\sin\theta'\sin\phi' \\ r\cos\theta' \end{bmatrix}$. xyz is the coordinate

system defined in Figure 2-1. $(x, y, z)$ and $(r, \theta, \phi)$ are related by $\begin{bmatrix} x \\ y \\ z \end{bmatrix} = \begin{bmatrix} r\sin\theta\cos\phi \\ r\sin\theta\sin\phi \\ r\cos\theta \end{bmatrix}$.

The relations of xyz and XYZ coordinates using Euler angles are derived as follows.

Let's first find the rotation angles between the xyz and the XY'Z' coordinate systems where Ox is in the XOY' plane (i.e. OY' is in the xoX plane). Initally consider the XY'Z' coordinate systems to be overlapped with xyz coordinate system. First rotate XY'Z' coordinates around X axis by ange $\beta$. Then rotate the XY'Z' coordinates around Z' axis by the angle $\gamma$. After these rotations OX is pointing to the $(\theta_o, \phi_o)$ direction and the rotation angles $\beta$ and $\gamma$ are calculated as now describe. First note that

$$\angle POA = a\cos\left(\frac{1+(\sin\theta_o\cos\phi_o)^2-\left[(\sin\theta_o\sin\phi_o)^2+\cos^2\theta_o\right]}{\left|2\sin\theta_o\cos\phi_o\right|}\right) \tag{C1}$$

and assume that OP = 1; PB is perpendicular to xOy plane; OP is perpendicular to PC;

PAB plane is perpendicular to the x axis; BD is perpendicular to PA and D is on line PA.

Then

$$AP = \sin(\angle POA) \tag{C2}$$

$$AB = \sin(\theta_o)\sin(\phi_o) \tag{C3}$$

$$PB = \cos(\theta_o) \tag{C4}$$

$$PC = \tan(\angle POA) \tag{C5}$$

It can be proved that PB is parallel to z and BD is parallel to Z, therefore $\beta$ is equal to $\angle PBD$. Because $\angle PBD$ is equal to $\angle PAB$, we finally find that $\beta$ and $\gamma$ are given by

$$\beta = \angle PAB = a\cos(\frac{AP^2 + AB^2 - PB^2}{2AP \cdot AB}) \quad \text{(C6)}$$

$$\gamma = \angle POA \quad \text{(C7)}$$

After above two rotations, OX is along the $(\theta_o,\phi_o)$ direction, but OY' does not parallel to the ground. Therefore, one more step of rotation is needed which is to rotate XY' Z' coordinates around X axis by α degree to make OY' lines with OY which is in the plane of xoy. It can be proved that OY' is parallel to PC and OY is parallel to BC.

$$\alpha = 360^o - \angle PCB = 360^o - a\tan(PB / PC) \quad \text{(C8)}$$

Therefore, for any point P, its coordinate system in xyz and XYZ are $[x_1, y_1, z_1]$ and $[X_1, Y_1, Z_1]$ respectively. And they are related by

$$\begin{bmatrix} X_1 \\ Y_1 \\ Z_1 \end{bmatrix} = \begin{bmatrix} 1 & 0 & 0 \\ 0 & \cos\alpha & \sin\alpha \\ 0 & -\sin\alpha & \cos\alpha \end{bmatrix} \begin{bmatrix} \cos\gamma & \sin\gamma & 0 \\ -\sin\gamma & \cos\gamma & 0 \\ 0 & 0 & 1 \end{bmatrix} \begin{bmatrix} 1 & 0 & 0 \\ 0 & \cos\beta & \sin\beta \\ 0 & -\sin\beta & \cos\beta \end{bmatrix} \begin{bmatrix} x_1 \\ y_1 \\ z_1 \end{bmatrix} \quad \text{(C9)}$$

Where $\begin{bmatrix} X \\ Y \\ Z \end{bmatrix} = \begin{bmatrix} r\sin\theta'\cos\phi' \\ r\sin\theta'\sin\phi' \\ r\cos\theta' \end{bmatrix}$ and $\begin{bmatrix} x_1 \\ y_1 \\ z_1 \end{bmatrix} = \begin{bmatrix} r\sin\theta\cos\phi \\ r\sin\theta\sin\phi \\ r\cos\theta \end{bmatrix}$ (C10)

## APPENDIX D:

## Comparison of the analytically and HFSS derived radiation fields of a patch

A microstrip patch antenna consists of an electrically conducting ground plane, a substrate, and an electrically conducting patch on top forming an open-ended cavity. In this appendix, the size of dual polarized square patch is the same size as the substrate and the ground plane is set to infinitely large. Horizontally polarized and vertically polarized patch formulas have been derived in Balanis (1997) and in Appendix A of this dissertation. For the theoretical patterns, both radiating slots and non-radiating slots are considered in this appendix. And those theoretical derived formulas are plotted in Figure D1 and to compare with HFSS simulated patch patterns (Figure D2).

The parameters uses in both Figure D1 and Figure D2 are:

| | |
|---|---|
| frequency | 2.7051 GHz |
| dielectric constant of substrate | 2.2 |
| substrate height | 0.0142 λ |
| Patch length and width | 0.33114λ (this value is calculated from eqs. (14-1) to (14-3) in Balanis (Balanis 1997) to let Length L and width W the same) |

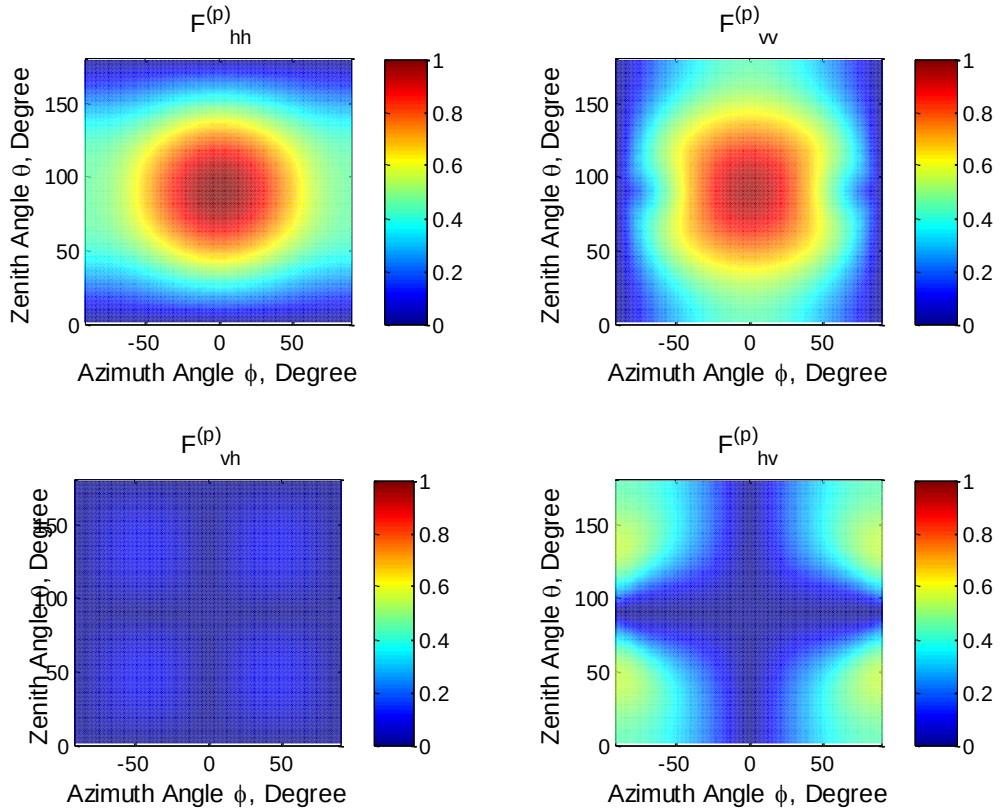


Figure D1. Patch patterns calculated by theory (Balanis 1997). Both radiating slots and non-radiating slots are considered.

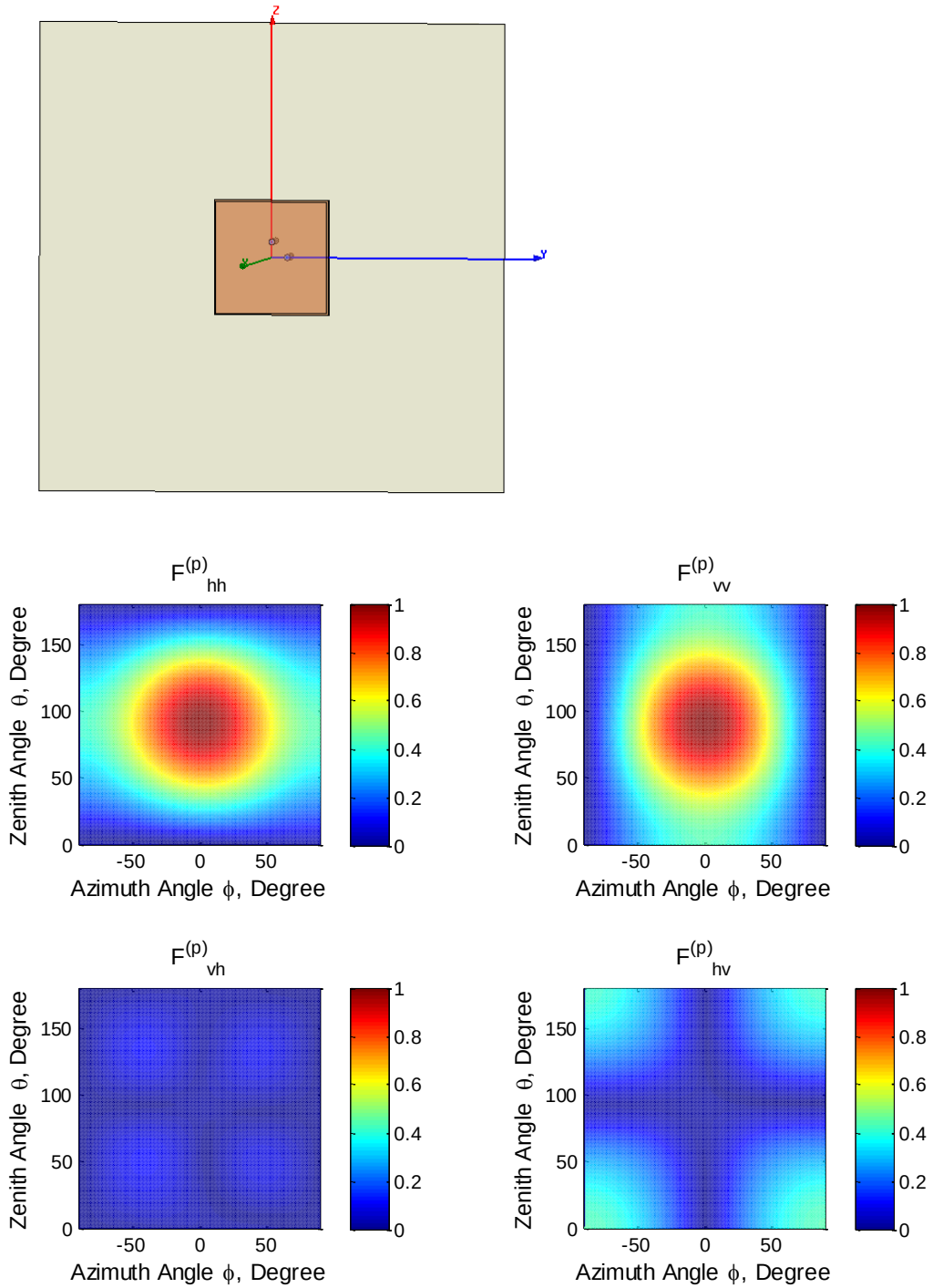


Figure D2. Patch patterns simulated by HFSS. The ground plane is infinitely large and the size of patch is same size as the substrate.

In Figures D1 and D2, $F_{\mathbf{vv}}^{(p)}$ is the copolar pattern of the V field $E_\theta$ if the V antenna port is energized and vice versa for $F_{\mathbf{hh}}^{(p)}$. $F_{\mathbf{hv}}^{(p)}$ is proportional to the H radiated electric field ($E_\phi$) if the V port is energized and vice versa for $F_{\mathbf{vh}}^{(p)}$. Both copolar and cross-pol patterns are normalized by the copolar peak. Comparing Figure D1 and Figure D2, we see that the ideal patch model approximates the HFSS simulated fields of the patch, For the HFSS simulated patch, but the cross-polar pattern nulls (Figure D2) are not exactly at $\theta = 90^0$ as shown by the theoretical pattern (Figure D1). This change in null line location is due to the higher order modes caused by the unsymmetrical location of the feed lines.